TIME-DEPENDENT DAMAGE OF SOFT MATERIALS WITH BOND BREAKING AND HEALING KINETICS

A Dissertation

Presented to the Faculty of the Graduate School

of Cornell University

in Partial Fulfillment of the Requirements for the Degree of

Doctor of Philosophy

by

Jikun Wang

May 2023

TIME-DEPENDENT DAMAGE OF SOFT MATERIALS WITH BOND BREAKING AND HEALING KINETICS

Jikun Wang, Ph.D.

Cornell University 2023

This study aims to understand the effect of polymer chain breaking and healing on the strain field ahead of the crack tip. Polyampholyte (PA) hydrogels are used as the system to learn about chain breaking and healing for transient bonds. Polydimethylsiloxane (PDMS) is used as the system to learn about the time-dependent damage of permanent bonds.

Firstly, for rate-dependent material, the constitutive model plays an important role in the analysis of mechanical properties, and model parameter fitting is the key to good development of the constitutive model. To get optimal model parameters fast and automatically, we propose an efficient method to determine the model parameters using machine learning (ML) algorithms together with singular value decomposition (SVD). SVD compresses training data and provides outputs for the ML algorithm. The trained ML algorithm rapidly computes the material responses for a large set of material parameters. We test our method by performing model fitting for PVA model (4 parameters), PA model with chemical crosslinks (9 parameters) and PA model without chemical crosslinks (13 parameters). While directly evaluating the constitutive model millions of times takes hundreds of hours, the ML prediction takes less than one hour for the same fitting effect.

Secondly, we study the strain-dependent chain breaking and healing for transient bonds in PA gels. PA gels are nonlinear viscoelastic, with time-

dependent behavior controlled by the breaking and reforming of ionic bonds in the dynamic network. Relaxation experiments are performed on single edge notch tension (SENT) and T shape specimens consisting of different variations of polyampholyte (PA) hydrogels. In contrast to the linear viscoelastic theory, faster relaxation speed in the higher strain region is observed in both SENT and T-shape samples, which demonstrates the strain-dependent chain dynamics in PA gels. We further find the load transfer between permanent and dynamic networks of different strengths. This load transfer mechanism is connected to viscoelastic behavior. All these experimental results are explained by a nonlinear viscoelastic model.

Thirdly, we study the time-dependent chain breaking of permanent networks by studying the delayed fracture of PDMS. Here we study the interaction between polymer chain damage and the elastic field experimentally using different specimens and crack geometries with blunt and sharp cracks. We find that stable slow crack growth can occur in sharp crack samples within a wide range of applied load, while catastrophic fracture can happen in blunt crack samples after hours of holding. Our experiments demonstrate a universal relation between crack growth rate and applied energy release rate in sharp crack samples. A model coupling nonlinear elastic fracture mechanics and rate-dependent bond scission is proposed to explain and describe this relationship.

BIOGRAPHICAL SKETCH

Jikun Wang was born in Xiangyang, an inland city in the middle of China. After graduating from No.4 High School of Xiangyang, he was admitted to Xi'an Jiaotong University to pursue his bachelor's degree in Engineering Mechanics. In 2016, he started doing research in Mechanics at Xi'an Jiaotong University, as a Master's student. In 2019, he began his Ph.D. study in Sibley School of Mechanical and Aerospace Engineering at Cornell University. His major concentration is Solid Mechanics and Materials.

To my families

ACKNOWLEDGEMENTS

Throughout my 4-year Ph.D. journey at Cornell, I encountered many obstacles that made me feel like my life was unreal. However, with the help of so many people, I'm grateful that I didn't have to face these challenges alone.

I would like to express my deepest gratitude to my advisor, Prof. Alan T. Zehnder, for not only imparting valuable knowledge and skills but also for showing me the importance of kindness and empathy towards others. Prof. Alan T. Zehnder is always patient and ready to provide guidance and support whenever I need. His unwavering dedication and support inspire me to achieve personal and professional growth.

I am incredibly grateful to Prof. Chung-Yuen Hui. I have been really fortunate to work with him. Without his expertise and enthusiasm, I would not have been able to complete this work to such a high standard. I am genuinely grateful for his continuous efforts to develop my research attitude and habits. I would also like to thank Prof. David Bindel for serving in my committee. He is always kind and has provided helpful guidance for my machine learning research and my minor in computer science. Then I would like to thank Prof. Jian-Ping Gong and Prof. Jingjie Yeo for their help with my research.

I am also grateful to my research participants Tianjiao Li, Bangguo Zhu and Kunpeng Cui for their collaboration, friendship and support. Their dedication, passion and expertise have enriched my learning experience and made my research more productive.

Finally, I'd like to express my heartfelt gratitude to my parents for their unwavering support, love and understanding throughout my academic journey. Despite not being able to see them in person for the past four years, they have always been my support and motivation to pass through the tough times.

TABLE OF CONTENTS

LIST OF TABLES

LIST OF FIGURES

CHAPTER 1

INTRODUCTION

Soft polymeric materials such as elastomers and gels are essentially networks of polymer chains, with or without solvent trapped within the networks [1, 2]. Due to the innate flexibility of long polymer chains, soft materials usually exhibit high compliance, low friction and good compatibility with biological tissues. With these desirable properties, soft materials have been extensively studied in soft robotics [3], wearable and stretchable electronics [4, 5], bio-transducers and separation membranes [6], tissue engineering [7], drug delivery [8], etc. Some of the widely studied soft materials include hydrogels [9], room-temperature-vulcanizing silicone (RTV silicone) [10], soft composite materials or structures [11], and other applications.

For most of those applications, good mechanical properties such as high stretchability and high toughness, are required, which are not satisfied by traditional soft materials [9]. Many toughening mechanisms have been proposed to make tougher and stronger soft materials[9, 12], such as interpenetrating polymer networks [13, 14], coupled covalent and ionic bonds [15], combining permanent and transient networks [16, 17], and soft composite materials [11]. Among all these mechanisms, one of the most widely used is combining permanent and transient bonds to make double network materials [18]. The permanent bonds can keep the solid state of the materials, whereas the transient bonds can break and reform; thus, a great deal of energy can be dissipated to prevent the materials from fracturing. For example, Sun et al. [15] synthesized tough hydrogels by mixing ionically crosslinked alginate as transient network and covalently crosslinked polyacrylamide as permanent network. With the internal hysteresis

introduced by the ionic bonds, this gel can be stretched 20 times its initial length and has a toughness of 9000 J/m^2, despite its high water content of 90%. And its mechanical properties can recover 80% after 24 hours at a temperature of $80°C$. Mayumi et al. [16] developed a specific type of poly(vinyl alcohol) (PVA) dual-crosslink hydrogel. This gel contains one network with covalent (permanent) and physical (transient) bonds. During loading, the covalent bonds remain attached while the physical bonds can break and reattach, so it has strong rate-dependent behavior and can recover to its full mechanical properties after several hours at room temperature. Sun et al. [17] reported the synthesis of a tough polyampholyte (PA) hydrogel with ionic bonds and chemical bonds (optional). The strong bonds or chemical bonds serve as permanent crosslinks, whereas the weak bonds can break and reform to dissipate energy. This PA gel has a toughness of 4000 J/m^2, and can fully recover just by soaking the gel in deionized water. This gel also has excellent fatigue resistance [17] and is stable in deionized water for an extended period.

With these highly extensible and tough soft materials, many studies have been done to understand the mechanical properties of such materials. For example, Lu et al. [19] developed a coupled viscoelasticity and Mullins effect model to describe the stress-strain relation of Alginate-Polyacrylamide hydrogel. Guo et al. [20] built a constitutive model that captures the kinetics of transient bonds in PVA hydrogel. Venkata et al. [21, 22] reported models to characterize the strain-dependent chain kinetics in PA hydrogels with and without chemical bonds. Despite the accuracy of these models, how chain healing and breaking affect the failure of soft materials, especially at large deformation, remains unclear. When a crack is present in the material, the strain/stress field and the strain/stress gradient near the crack tip can be very high. Suppose the dynam-

ics of bond breaking and healing are sensitive to stress/strain, especially when deformation is large. In that case, it is reasonable to expect that the material behavior near the crack tip cannot be adequately described by linear viscoelasticity [23]. Under these circumstances, nonlinear viscoelasticity will dominate near the crack tip, which implies that load transfer can happen between permanent and transient bonds near the crack tips. Also, since the bond breaking and healing are time-dependent, such materials can have time-dependent strength, which means that traditional ways of measuring toughness may be inaccurate.

This study aims to understand the time-dependent, large deformation mechanical responses of soft polymeric materials with bond breaking and healing through experimental and theoretical analysis. This study focuses on the effect of polymer chain breaking and healing, with three types of materials as examples, PDMS, PVA hydrogel and PA hydrogel. PDMS is a commonly used RTV silicone rubber with only covalent bonds, so it is an ideal material for us to study the dynamics of permanent networks. PVA hydrogel is a kind of linear viscoelastic material [20], whose chain breaking and healing rate is independent of strain level. PA gel is considered a highly nonlinear viscoelastic material [17, 21]. However, strain-dependent chain kinematics have not been observed directly. In this study, we will use the proposed constitutive models and specially designed experiments to further the study of these materials.

This thesis is organized as follows. In Chapter 2, the details of the experimental setups are provided, including materials preparation, sample measurement, tensile tester build up and digital image correlation (DIC) implementation. In Chapter 3, some constitutive models for these materials are introduced. Those models are proposed by previous Ph.D. students at Cornell. We will show

all the equations in detail, but omit some physical or mathematical assumptions. More details can be found in the original papers [20, 21, 22].

To get good parameters for these constitutive models, a machine learning framework for constitutive model fitting is studied in Chapter 4. Parameter fitting for complex time-dependent constitutive models is important but often tedious work. In this part, we propose a machine learning framework, which can perform model fitting automatically. This method is applied to PVA and PA constitutive models. It is shown that this method can accelerate the fitting process by 100 times faster than random search or grid search. The work in this chapter is published in Journal of the Mechanics and Physics of Solids [24].

In Chapter 5, the nonlinear viscoelasticity of PA hydrogels due to strain-dependent polymer chain breaking and healing is explored. We utilize the digital image correlation (DIC) method to reveal the nonlinear viscoelastic effects near the crack tip experimentally, and use PA constitutive models to show the physical mechanisms for these phenomena. Nonlinear viscoelasticity leads to the strain increase near the crack tip during the relaxation test, while the load transfer between physical (or transient) and chemical (or permanent) networks can decrease the strain during relaxation. These effects play critical roles in the fracture of such kinds of materials. This work is published in Extreme Mechanics Letters [25].

The time-dependent damage of PDMS is studied in Chapter 6. Although there have been many studies on the fracture and delayed fracture of soft materials [26, 27, 28], there has not been even a clear definition of delayed fracture for these materials. The main reason is that delayed fracture behavior in soft materials is sensitive to many factors, so it is hard to draw a clear conclusion

without comprehensive studies. In this work, PDMS is used as an example for a comprehensive study of delayed fracture. Different types of delayed fracture behaviors are clearly defined. Experiments for sharp crack delayed and blunt crack delayed fracture. With these results, the delayed fracture of PDMS can be explained by the time-dependent damage of permanent chains. All the results are considered together to build a time-dependent damage model for PDMS. This model can predict the relationship between crack propagation rate and energy release rate quantitatively, and the crack evolution for short initial crack quantitatively. This work is planned to be submitted recently.

CHAPTER 2

EXPERIMENTAL SETUPS

2.1 Introduction

In this study, experimental methods were used to study the mechanical properties of soft materials with nonlinear effects. The basic experimental setups are introduced in this chapter, including materials preparation, custom-built tensile tester design, and digital image correlation (DIC) measurement system implementation.

2.2 Materials preparation

In this study, all material precursors are made in liquid state and then cured into thin sheets. The mold we used to accommodate the precursors is shown in Fig. 2.1.

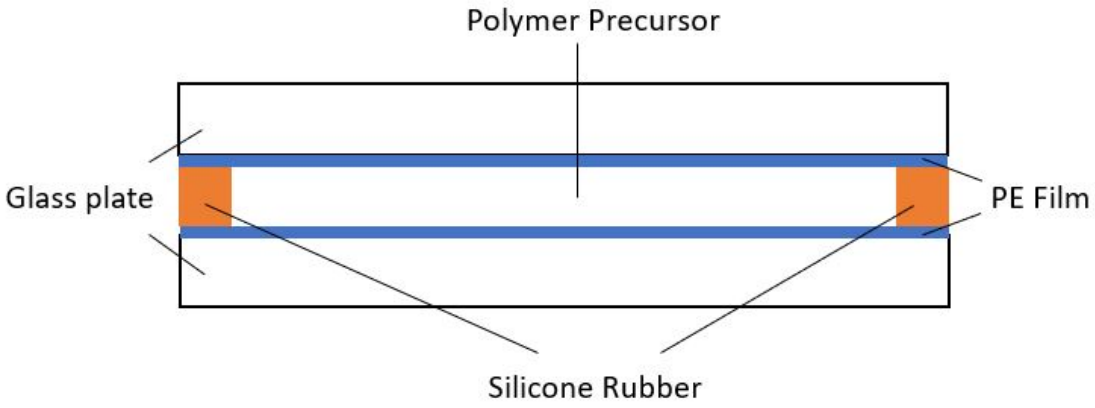

Figure 2.1: Mold used for making thin sheets of materials

2.2.1 PVA gel preparation

To make PVA hydrogels, we first added 30g PVA 16 wt% solution to the beaker under active stirring. Then 0.82g GA 2.5 wt% solution was added. The GA 2.5 wt% solution was always freshly diluted from GA 25wt% solution (Sigma-Aldrich, Grade II, G6257-10ml) with deionized water. After stirring for about 10 minutes, 0.8ml hydrochloric acid (HCL, 1 mol/L) was added to the solution and stirred for another 10 minutes. After the solution was mixed evenly, the solution was injected into a mold using a syringe.

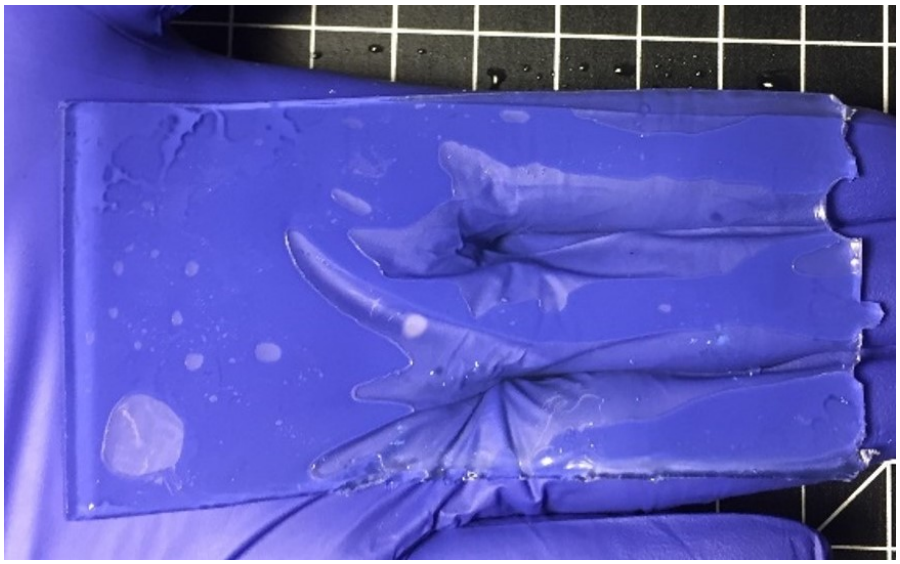

Figure 2.2: Sample of PVA hydrogel

The mold was made of acrylic plates spaced by silicone rubber (2mm in thickness) with acetate sheets attached to the acrylic. The solution polymerizes in 36 hours. Then we removed the gel from the mold and soaked the gel with distilled water to neutral pH. The water was changed several times. After 24 hours of washing, the chemically crosslinked gel was swollen and very brittle.

After washing the chemically crosslinked gel, we soaked the gel in a fresh Borax/NaCl solution to form the physical bonds. The Borax and NaCl were

from Sigma-Aldrich (Borax: Sodium tetraborate decahydrate, ACS reagent, ≥ 99.5%, S9640-500 g; NaCl: Sodium chloride, puriss. pa., ≥ 99.5%, 71380-1 kg). The concentration of borax and NaCl in the solution was 1 mM/L and 90 mM/L, respectively. For the chemical gel of weight m, we soaked it in the Borax/NaCl solution of weight 20m. The gel was soaked in the solution for at least 3 days to reach equilibrium.

2.2.2 PA gel preparation

$c - PA_{weak}$ and $p - PA_{weak}$ gels are made from p-styrenesulphonate (NaSS) and N-dimethylaminoethylacrylate (DMAEA-Q), with and without MBAA (Wako Pure Chemical Industries Ltd., Japan) as crosslinker. $c - PA_{strong}$ and $p - PA_{strong}$ are made from NaSS and 3-(methacryloylamino) propyl-trimethylammonium chloride (MPTC) with and without MBAA.

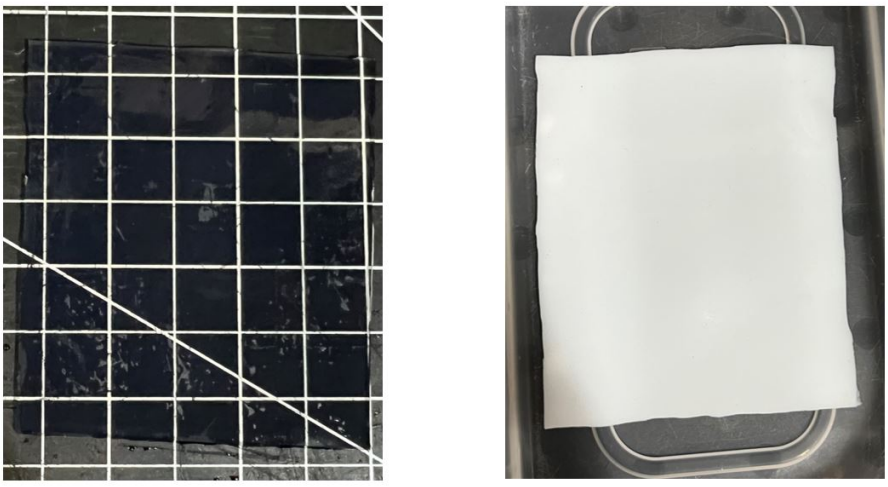

(a) (b)

Figure 2.3: Sample of PA hydrogels. (a) c-PA gel. (b) p-PA gel

For the gels with weak stickers, P(Nass-co-DMAEA-Q) gels, the concentra-

tion of monomers (NaSS and DMAEA-Q) is 2.5 M, and the molar ratio is NaSS: DMAEA-Q = 0.516 : 0.484. The concentration of initiator α-keto is 0.1 mol% with respect to monomer concentration. The concentrations of MBAA are 0, 0.3 and 0.5 mol%, respectively. For the gels with strong stickers, the concentration of monomers (NaSS and MPTC) is 2.1 M and the molar ratio is NaSS : MPTC = 0.517 : 0.483. The concentration of α-keto is 0.25 mol%. The concentrations of MBAA are 0 and 0.3 mol%, respectively. In both gels, the precursor solution was deoxidized in an Argon glove box and then injected and sealed into a mold made by glass plates and silicone rubber spacer (120 mm $\times$ 12 mm $\times$ 2.2 mm. The solution was polymerized under UV irradiation for 11 hours. After polymerization, the as-prepared gel was soaked in deionized water for one week to remove counter-ions and reach equilibrium. The deionized water was changed every day.

2.2.3 PDMS preparation

PDMS precursor was bought from Dow Inc. and used without preprocessing. The PDMS elastomers were prepared by mixing PDMS Sylgard 184 prepolymer and cross-linking agent at a 10:1 ratio. After stirring evenly for 10 minutes, air bubbles inside the mixture were removed in a vacuum chamber. Then the PDMS was poured into a mold made of glass plates and silicone rubber spacer (120 mm $\times$ 120 mm $\times$ 0.5mm). The thickness here is smaller than the thickness of PVA and PA gels because the modulus and strain hardening of PDMS is much higher, which makes it much harder to grip thick PDMS samples. The mold was put into an oven and heated for 4 hours at 65 $^{\circ}C$.

2.2.4 Thickness measurement

Since the silicone rubber spacer was hyperelastic and the materials we synthesized in this study were all soft materials, the thickness of the specimen was not exactly the same as the spacer and was hard to measure with calipers. So we used a Newport translation stage and a GAERTNER modular microscope to measure the thickness. The setup is shown in Fig. 2.4. We first aligned the center of the microscope cross-hair with one edge of the specimen. Then we moved the microscope with the translational stage until the crosshair center was aligned with the other edge of the specimen. The displacement was the thickness of the specimen.

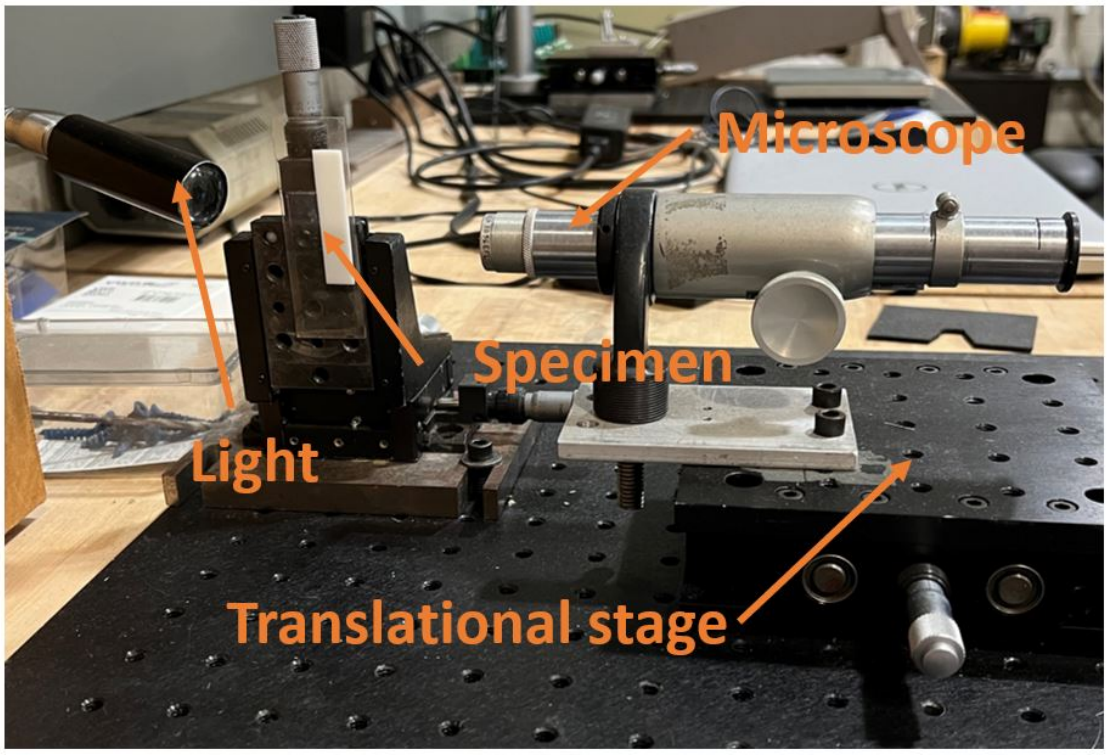

Figure 2.4: Thickness measurement tool for soft materials

2.3 Tensile tester setup

In this study, the modulus of materials ranges from 1kPa to 10MPa, and the deformation ranges from 1% to 1000%. To satisfy these requirements, the maximum force of the tester should be 100N with a precision of $0.01N$, and the maximum displacement of the tester should be 300mm with a precision of $10\mu m$. Based on these criteria, we built a custom-built tensile tester for all the uniaxial tensile tests in this study. Fig. 2.5 shows the custom-built tensile tester used in this study. It was designed and built in Zehnder's laboratory by Jikun. It is combined by three main modules: displacement controlling, sensing, gripping, and data collection.

2.3.1 Displacement sensing and control

For uniaxial tensile tests, the displacement is applied to materials along one direction, which is achieved using a straight guide rail driven by a NEMA 23 motor. The motor is connected to a motor driver DM542T, which can be controlled precisely through electric pulses from a single chip like Arduino or Raspberry Pi. As for displacement data, this tester has two outputs. One is the input displacement data given to the guide rail; another is the output of the displacement sensor (CALT 500mm Draw Wire Encoder, CWP-S500 0-5Kohm). The displacement data from these two methods are quite consistent, so we mainly use the input data as the displacement data for its low noise.

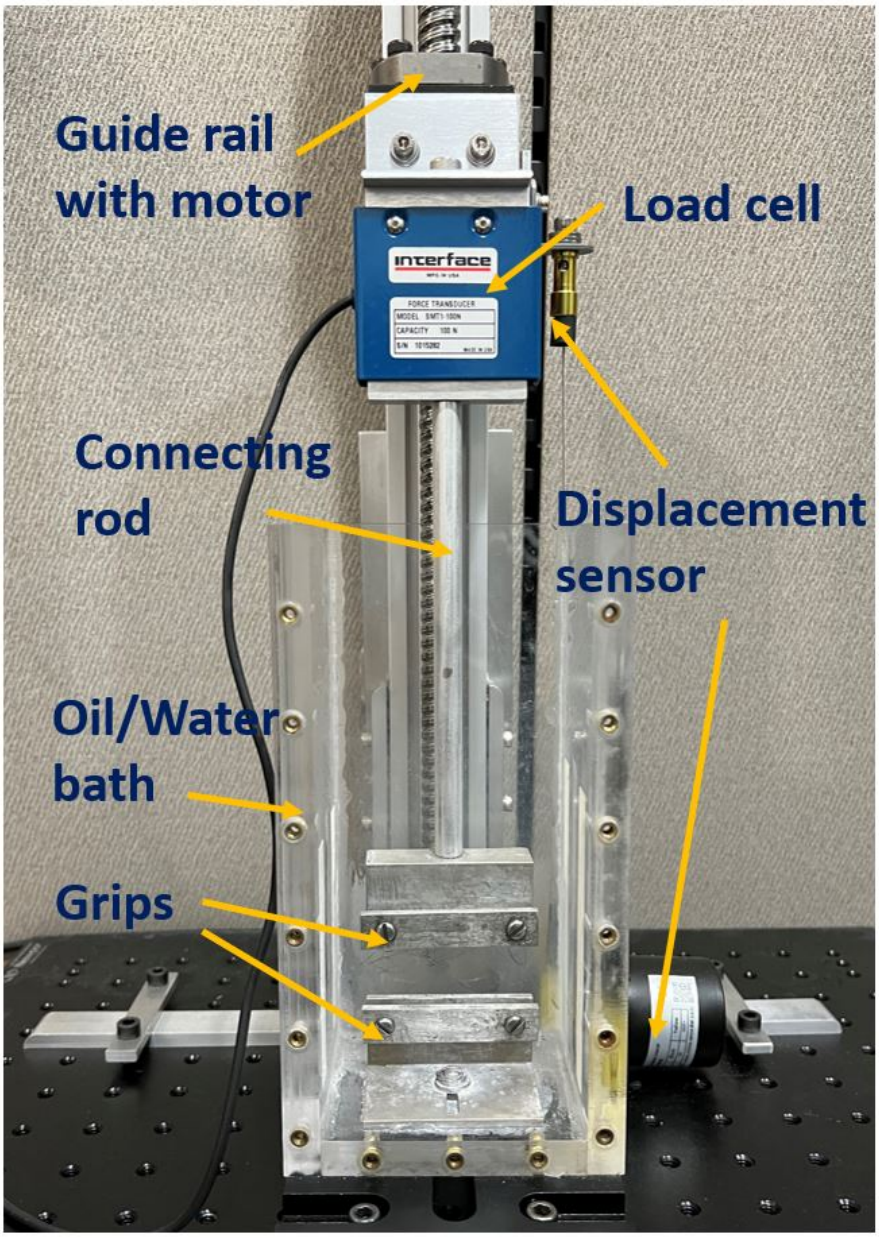

Figure 2.5: Custom-built tensile tester for soft materials. Controlling, signal conditioning and data collection modules are not included in this figure.

2.3.2 Force sensing

We use a $100N$ load cell from Interface Inc. to measure the force applied to the samples. The main part of the load cell is a strain gauge. The force applied to the two ends of the load cell will change its deformation and finally leads to a

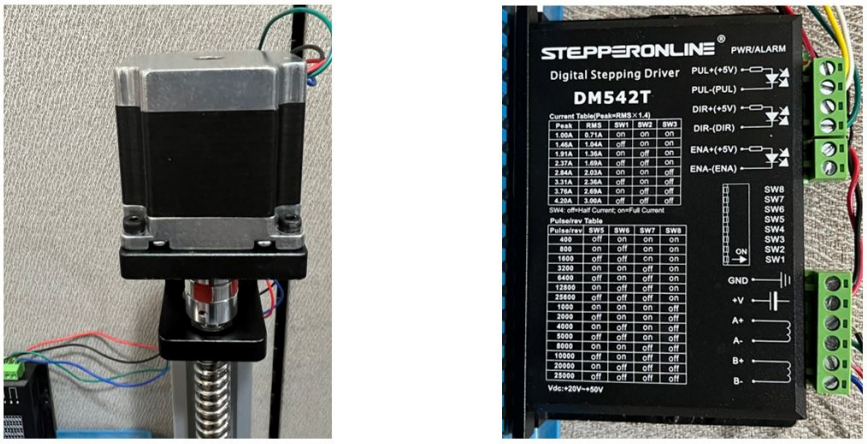

(a) (b)

Figure 2.6: Displacement controlling module. (a) Nema 23 step motor. (b) DM542T digital stepping driver.

change in the resistance of the strain gauge. So, to get the force value during tensile tests, one end of the load cell is fixed to the guide rail slider, and the other is connected to the gripper through a long connecting rod. The resistance change is minimal, so a bridge circuit is used inside this load cell to measure such change. However, even with the bridge circuit, the output voltage is still too small to be measured with an Analog-to-Digital Converter (ADC, ADS 1115) directly. We further use a voltage amplifier CALEX 163MK signal conditioner to amplify and filter the voltage signal from the load cell.

One important thing for the load cell is calibration to ensure the force captured by the controlling system is correct. The measuring range of this load cell is $-100N$ to $+100N$, and the measuring range of the ADC is $-5V$ to $5V$. So we want to change the voltage output of the load cell so that $1V$ difference in voltage means $20N$ difference in force. This calibration is done through the amplifier CALEX 163MK. We first tune the output offset of the amplifier so the voltage is $0V$ when there is no force applied to the load cell. Then we add the gripper to the load cell. After that, we tune the gain of the amplifier until the voltage

(a) (b)

Figure 2.7: Force sensing module. (a) 100 N load cell. (b) Signal conditioner.

difference is $0.245V$ with and without a $500g$, $(4.9N)$ weight attached to the gripper. After this calibration, the voltage read by ADC is correlated with the force correctly.

2.3.3 Gripper and water/oil box

Hydrogels can contain more than 90 wt% of water, and their mechanical properties can vary a lot even with a small change of water content. To prevent the gels from drying or swelling during tests, we made an acrylic box where the samples can be immersed in mineral oil or water. As shown in the figure, we use an aluminum rod to connect the upper gripper and the load cell, and the lower gripper is fixed to the bottom of the box. The side view of this box is shown in

Fig. 2.8. The front surface of this box is detachable. Once the sample is gripped, the front surface is tightened to the box with screws, and oil/water proof foam is placed between the box and the front surface to prevent the oil/water from leaking.

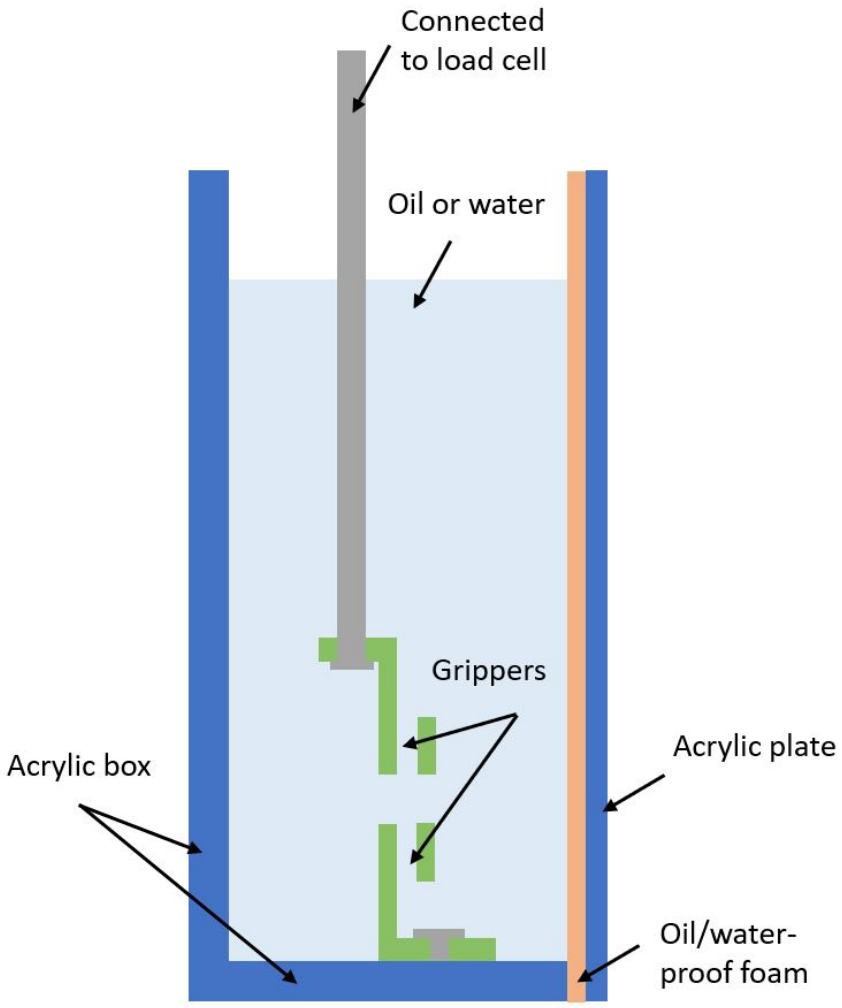

Figure 2.8: Side wide of the water/oil tank

2.3.4 Control system and data collection

The central part of the control system is a Raspberry Pi 4B, and the controlling program is written in Python. Using specific Python codes, Raspberry Pi 4B can output electric pulses to control the guide rail movement, and at the same time, it can read the voltage from the force sensor and the displacement sensor through an analog-to-digital converter (ADC) with given frequencies. The voltage data is then transferred to force (N) and displacement (mm) data using calibrated parameters.

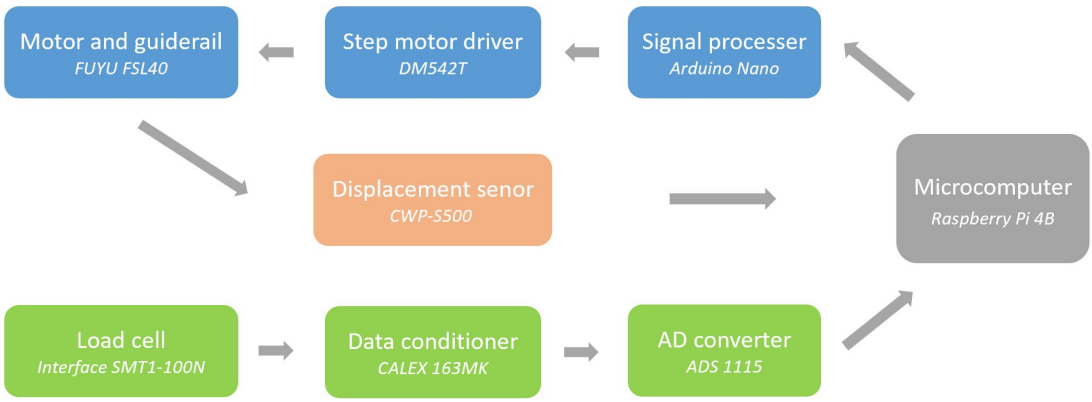

Figure 2.9: Data flow in the tensile tester control system

2.4 Digital image correlation measurement

While the tensile tester can measure the force/displacement responses of samples, it cannot probe the spatial strain field of samples undergoing non-uniform deformation, especially when strain concentration is high at some points. As a non-contact, full-field deformation measurement method, digital image correlation (DIC) is an ideal candidate for measuring non-uniform deformation. There are different types of DIC for different measuring purposes. In this study, most

of the tests are done under plane stress condition, so we only care about the strain in x-y plane. Based on this requirement, we chose 2D DIC to measure the planar motion of material points during our tests and only one camera is needed. The details of 2D DIC theories, equipments, algorithms, applications, etc, can be found in the comprehensive review papers published by Pan et al. [29].

2.4.1 Speckle pattern generation for DIC tests

Generating a high-quality speckle pattern is one of the most important parts of DIC measurement, especially for hydrogels, due to their very high water content. Considering the difficulties of different methods and the precision needed for this study, we chose to generate speckle patterns by spraying black ink using an airbrush.

Ink used

As we mentioned in section 2.3, most tests need to be done in water or mineral oil, so the ink we use for our samples should be waterproof and oilproof (at least for mineral oil). Under this constraint, the ideal ink should dry fast and attach to the surface of the sample tightly. After trying several different types of ink, we finally chose Mark II 1250 brand ink.

Pattern generation using airbrush

The speckle pattern on the surface of the sample should have moderate size and density. Large speckles will lead to poor DIC precision, and very small speckles cannot be captured by the camera we use. To obtain a good pattern, air

pressure of 80 psi and a low flow of ink are used. Samples of speckle patterns with different qualities are shown in Fig. 2.10.

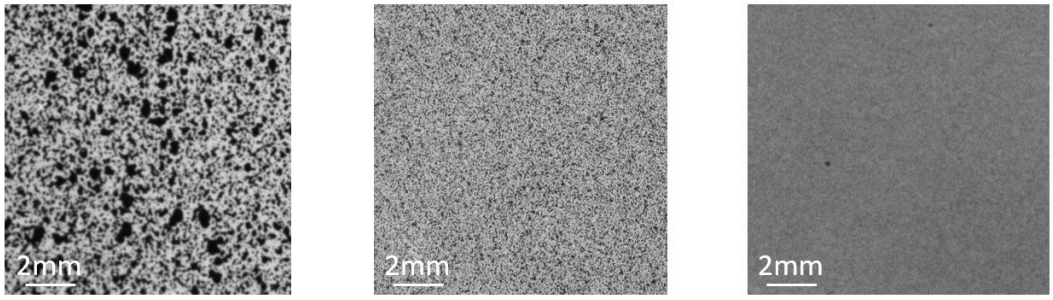

Figure 2.10: Samples of speckle patterns with different qualities. (a) Speckles are too large. (b) Speckles are good. (c) Speckles are too small.

2.5 FLIR camera system

In this study, we use a FLIR camera with telecentric lenses to capture the picture of speckles during tensile tests. For 2D DIC, there is no specific limitation for the choice of photo capturing system, so long as the photos are not distorted, and all the speckles are clear.

The images of speckles for DIC measurements were captured using a CCD camera (FLIR Grasshopper3 4.1 MP Mono) with two telecentric lenses (Edmund Optics, SilverTL 0.16×, 0.5×). The first lens has larger field of scope but smaller precision, whereas the second one has smaller field of scope but higher precision. The first one is mainly used for measuring the strain field for the whole sample and the second one is mainly used for monitoring what happens near the crack tip.

To make the speckles clearer and decrease the image noises, two LED

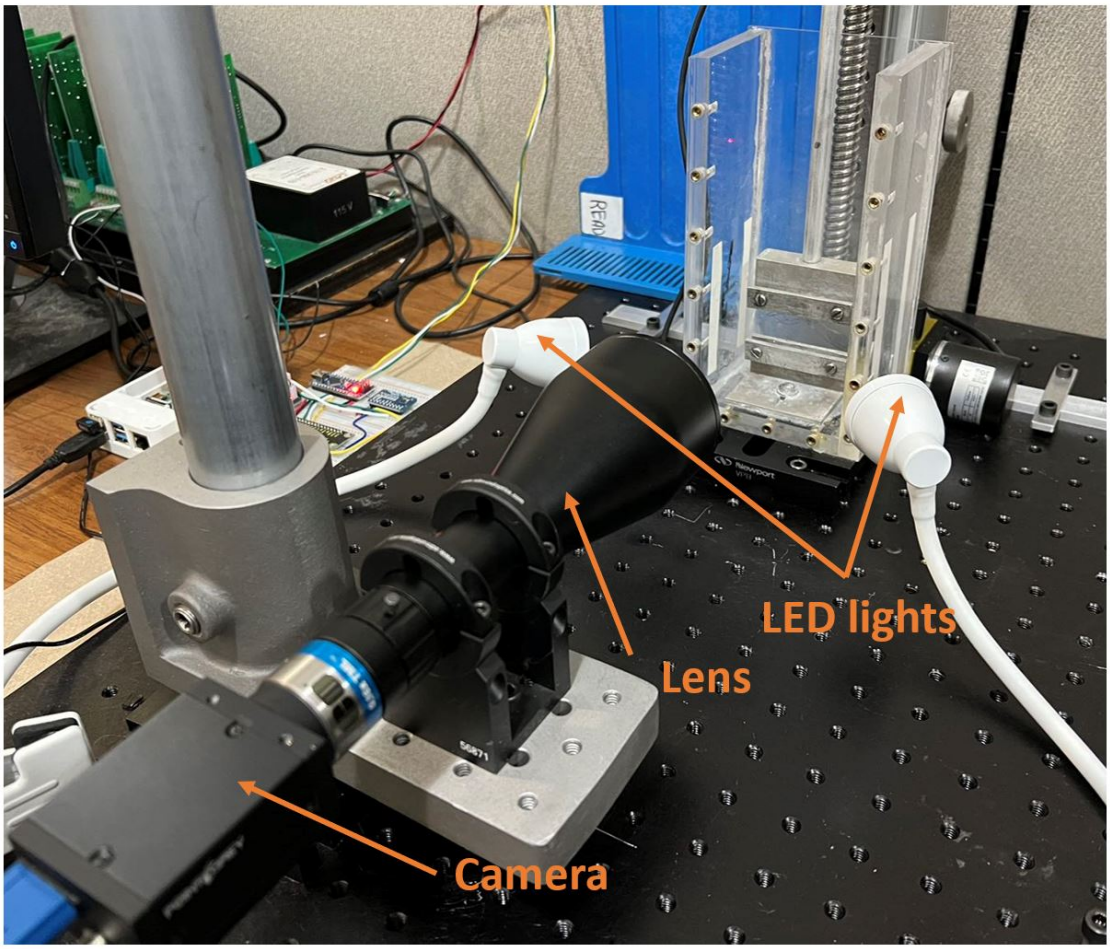

Figure 2.11: FLIR camera system for DIC measurement

lights were used to provide additional illumination. The whole system is fixed on an optical breadboard, and the camera is connected to the computer using a USB cable. The camera is activated through the signals from the cable. In this study, we use Python codes to control its working states. More details about this camera can be found on its official website "https://www.flir.com/products/grasshopper3-usb3".

2.5.1 DIC calculation using Ncorr

Ncorr is a free 2D DIC measurement package in MATLAB, which utilizes the reliability-guided DIC algorithm developed by Pan et al [29]. The most important feature for us is that Ncorr can capture large deformation very well, using the algorithm developed by Pan et al. [29]. The parameters used for our tests will be provided. More details about Ncorr can be found on its official website.

Code calibration

Here we validate the precision of Ncorr using virtual speckle patterns. We first generate random speckles and then deform the whole image with the given strain fields. Fig. 2.12 shows the calibration results for normal strains, and Figure Fig. 2.13 shows the calibration results for shear strain. The strain shown in Figure 2.13 is Green-Lagrangian strain in $x - y$ direction, so the given value is exactly $0.4/2 = 0.2$. Both tests show that the calculation from Ncorr is quite accurate even for large deformation.

Parameter choice and data processing

Large strain analysis is activated in Ncorr to update the reference image. The important input parameters are the subset radius, the radius of a circular subset used to correlate sub-images, is set to 10-20 pixels; the subset spacing, the spacing between neighboring subsets, is set to 0-2 pixels; and the strain radius, the size of the region over which displacement data are fit to a plane to calculate the displacement gradient, is set to 3-5. The choice of these parameters is determined by the quality of speckle patterns and the strain distribution and may vary from test to test. Generally speaking, smaller values of those parameters can give us higher DIC precision. However, due to various limitations such as

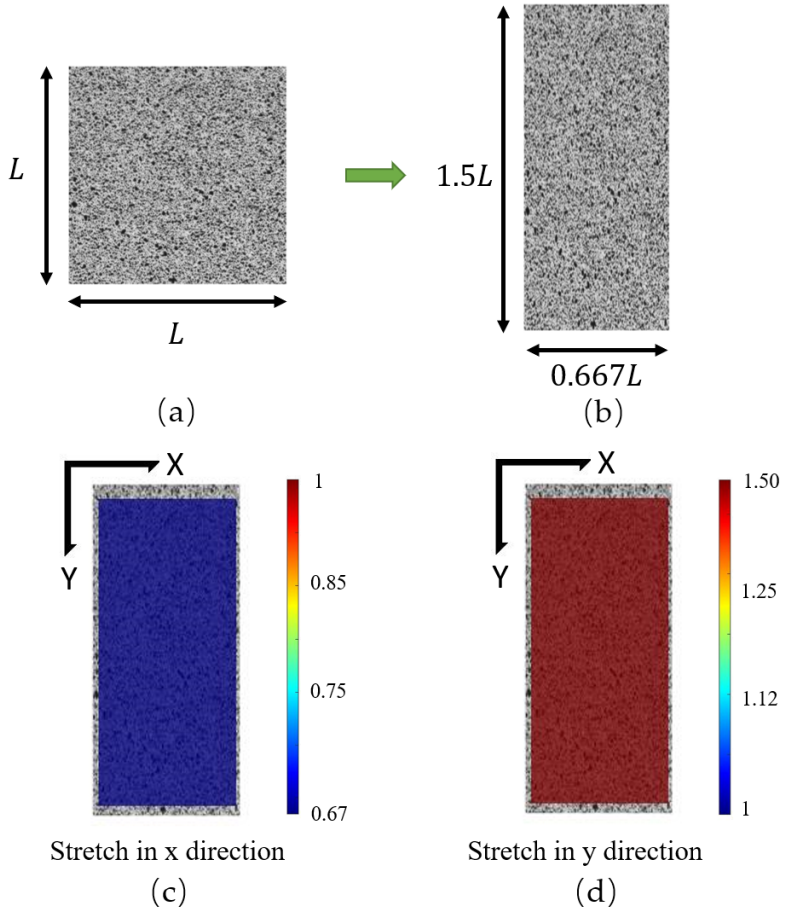

Figure 2.12: Normal strain calibration for Ncorr. This figure shows a virtual speckle pattern (a) before deformation and (b) after deformation, and the stretch calculated by Ncorr in (c) x direction and y direction.

speckle pattern quality, camera precision, photo quality, etc, sometimes we may lose track of the movement of speckles with very small value or get results with large noise. In this study, we usually start from a small value of subset radius, 10 pixels, and increase this value if Ncorr fails to finish the correlation calculation.

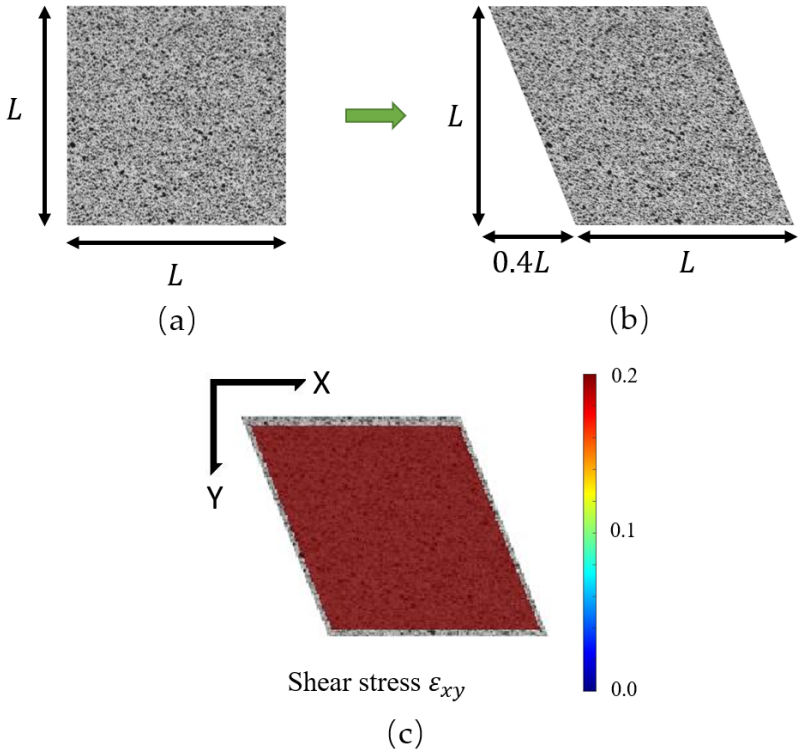

Figure 2.13: Shear strain calibration for Ncorr. This figure shows a virtual speckle pattern (a) before deformation and (b) after deformation, and the shear strain calculated by Ncorr in (c) $x - y$ direction.

CHAPTER 3

CONSTITUTIVE MODELS INTRODUCTION

A fundamental problem in the mechanics of solids is to develop constitutive models which accurately predict the mechanical response of materials subjected to applied loads. The simplest constitutive model is an ideal elastic solid, which is a reasonable approximation for traditional engineering materials. The elastic solid represents an extreme case of material behavior where there is a unique relation between stress and strain. Many materials, for example, soft solids such as rubber and gels, are viscoelastic or viscoplastic. These materials, besides being rate-sensitive, may sustain very large deformation before failure. The mechanical behavior of rate dependent solids remains a major challenge to material physicists and mechanicians. Experiments on material behavior are time-consuming and are often limited by the amount of material available. Further, it is impossible to cover the entire spectrum of loading configurations and histories by experiments. Thus, the development of constitutive models must be complemented by theoretical modeling. Fortunately, in this work, we already have very good constitutive models for the materials we analyzed. Those models were established by professors and students in our research group. Here I introduce these models briefly and explain the meaning of some important equations and parameters. More details about how these models are built can be found in our previous papers [20, 21, 22].

3.1 PA gels

In the following, we summarize the constitutive model governing a uniaxial tension test where the stretch ratio $\lambda(t)$ in the loading direction is prescribed for two kinds of PA gels used in this work. The multi-axial versions of these constitutive models were developed and fully explained in our previous works [21, 22]. Photographs of the c-PA and p-PA gels are shown in Fig. 2.3. It is obvious that the c-PA gel is transparent and the p-PA gel is opaque. The appearance of these two types of gels means there is phase separation within the p-PA gel, whereas there isn't in the c-PA gel [30]. Our constitutive models for c-PA and p-PA gels are based on this physical fact.

We start with the c-PA gel (intermediate complexity with $q = 9$, where q means the number of independent parameters in the model), followed by the p-PA gel ($q = 13$). In the following, stretching commences at $t = 0$. Before this time the sample is in its pristine unstressed state.

The nominal stress for the c-PA gel is [22]

$$\sigma(t) = \left(\omega_{chem} + 2\rho\phi_B(\tau = 0, t, H^{0\to t})\right) \times 2 \left.\frac{dW_0}{dI_1}\right|_{I_1(t)} \left(\lambda(t) - \lambda(t)^{-2}\right) \tag{3.1}$$

$$+ \int_0^t \left[\chi(\tau)\phi_B(\tau, t, H^{\tau\to t}) 2 \left.\frac{dW_0}{dI_1}\right|_{I_1(t)=H^{\tau\to t}} \left[\frac{\lambda(t)}{\lambda^2(\tau)} - \frac{\lambda(\tau)}{\lambda^2(t)}\right]\right] d\tau$$

where ω_{chem} is the molar fraction of chemical bonds, W_0 is the strain energy density function for the network, I_1 is the trace of the deformation gradient tensor evaluated at t, ρ is the molar fraction of connected physical cross-links at $t = 0$ and

$$\phi_B(\tau, t, H^{\tau\to t}) = \left[1 + \frac{\alpha_B - 1}{t_B} \int_\tau^t f(H^{\tau\to s}) ds\right]^{\frac{1}{1-\alpha_B}} \tag{3.2}$$

is the survivability function, it is the fraction of physical crosslinks that survive

from the time of their formation τ to the current time t. In Eq. (3.2), t_B is the characteristic breaking time of physical crosslinks, α_B is a material parameter that controls the rate of decay of the survivability function and $f$is a function which measures the dependence of breaking rate on the stretch experienced by a physical bond from its formation at time τ to the current time $t > \tau$. $H^{\tau\to t}$ is the trace of the deformation tensor at t using the configuration at τ as the reference state. In uniaxial tension, it is

$$H^{\tau\to t} = \frac{\lambda^2(t)}{\lambda^2(\tau)} + \frac{2\lambda(\tau)}{\lambda(t)} \tag{3.3}$$

Finally, $\chi(\tau)$ in Eq. (3.1) is the fraction of broken physical bonds divided by the characteristic healing time t_H. This healing rate $\chi(\tau)$ is history-dependent and is given by the solution of the nonlinear Volterra integral equation

$$1 - \omega_{chem} = \chi(t)t_H + \int_{-\infty}^{t} \phi_B(\tau, t, H^{\tau\to t})\chi(\tau)d\tau \tag{3.4}$$

Here we note that ρ is related to the other parameters by $\rho = \frac{(1-\omega_{chem})_{t_B}}{(2-\alpha_B)t_H+t_B}$. W_0 is the free energy function for polymer chains, and it is given by a 3-term Yeoh's model, i.e.,

$$W_0(I_1) = \sum_{i=1}^{3} c_i(I_1 - 3)^i \tag{3.5}$$

where c_i are material constants and the breaking function f is

$$f(I_1) = \left(1 + \frac{I_1 - 3}{I_c - 3}\right)^m \tag{3.6}$$

where $I_c > 3$ and $m > 0$ are material constants. I_c represents an effective stretch ratio where breaking accelerates, and m measures the severity of accelerated bond breaking. Eq. (3.1) to Eq. (3.6) implies that this model has 9 unknown material parameters.

$$\{c_1.c_2, c_3, \omega_{chem}, I_c, \alpha_B, t_B, m, t_H\}.$$

The physical meaning of Eq. (3.1) is as follows: the first term is the stress carried by the chemically crosslinked network, the second term is the stress carried by the physical crosslinks that remain connected from $t = 0$ to the current time t, the third integral is the stress carried by the healed chains in the physical network which survives to the current time.

The constitutive model for the p-PA gel is similar, except it has no chemical network. However, due to phase separation, there are two physical networks, each with their survivability and breaking functions. The material parameters associated with these networks have the same physical meaning as the physical network in c-PA gel and are labeled by the subscript i ($i = 1, 2$). For example, characteristic breaking times and healing times are denoted by t_{Bi}, t_{Hi} respectively. The nominal stress $\sigma(t)$ is related to the stretch history $\lambda(t)$ by [21]:

$$\sigma(t) = \left[\sum_{i=1}^{2} \rho_i \left[1 + \frac{\alpha_{Bi} - 1}{t_{Bi}} f_i(I_1(t))t\right]^{\frac{2-\alpha_{Bi}}{1-\alpha_{Bi}}}\right] \times 2 \left.\frac{dW_0}{dI_1}\right|_{I_1(t)} \left(\lambda(t) - \lambda^{-2}(t)\right) \tag{3.7}$$

$$+ \sum_{i=1}^{2} \int_0^t \chi_i(\tau)\phi_{Bi}(\tau, t, H(\tau, t))2 \left.\frac{dW_0}{dI_1}\right|_{H(\tau,t)} \left[\frac{\lambda(t)}{\lambda^2(\tau)} - \frac{\lambda(\tau)}{\lambda^2(t)}\right] d\tau$$

where $\rho = \frac{\omega_i t_{Bi}}{(2-\alpha_{Bi})t_{Hi} + t_{Bi}}$. Similar to Eq. (3.4), the healing rate $\chi_i(t)$ for each network is obtained by solving the integral equation

$$\omega_i - \rho_i \left[\phi_{B_i}(0, t)\right]^{2-\alpha_{Bi}} = \chi_i(t)t_{Hi} + \int_0^t \phi_{Bi}(\tau, t)\chi_i(\tau)d\tau \tag{3.8}$$

The survivablity functions have the same form as Eq. (3.2) except that the breaking function Eq. (3.6) is replaced by

$$f_i(I_1) = \exp\left\{\left(1 + \frac{I_1 - 3}{I_c - 3}\right)^{m_i} - 1\right\} \tag{3.9}$$

There are a total of 13 independent material parameters in this model, i.e., a

parameter vector $\vec{x}$ with components:

$$\{c_1, c_2, c_3, I_c, \omega_1, \alpha_{B1}, t_{B1}, m_1, t_{H1}, \omega_2, \alpha_{B2}, t_{B2}, m_2, t_{H2}\},$$

where $\omega_1 + \omega_2 = 1$.

3.2 PVA gel

Here, we summarize the model for the PVA hydrogel. We discuss this model later because it is a simplified version of c-PA gel where the chain breaking kinetics is independent of stretching [20], that is, linear viscoelasticity. This gel contains chemical network, and there is no phase separation within it.

With linear viscoelasticity, we set $f = 1$ and then Eq. (3.2) reduces to

$$\phi_B\left(\frac{t}{t_B}\right) = \left(1 + (\alpha_B - 1)\frac{t}{t_B}\right)^{\frac{1}{1-\alpha_B}} \tag{3.10}$$

Since the chain breaking kinetics is independent of stretch, the chains within this gel are constantly breaking and healing until reaching an equilibrium state, that is,the chain breaking rate equals chain healing rate. At this point, there is a steady state solution

$$\chi(t) = \chi_{ss} = \frac{\rho(2 - \alpha_B)}{t_B} \tag{3.11}$$

Now the integral equation is no longer needed, and $\chi(t)$ in Eq. (3.4) is replaced by χ_{ss}. Finally, the free energy function W_0 used in this model, strain hardening can be ignored because the fracture stretch for this gel fractures before the hardening happens, which leads to $c_2 = c_3 = 0$ in Eq. (3.5). In previous work, we use $c_1 = \mu/2$ where μ is the small strain shear modulus of the network. Thus, Eq. (3.1) reduces to

$$\sigma(t) = \mu\left[\omega_{chem} + \rho\phi_B(t)\right]\left(\lambda(t) - \lambda^{-2}(t)\right) \tag{3.12}$$

$$+\mu\chi_{ss}\int_0^t\left[\phi_B(t-\tau)\left[\frac{\lambda(t)}{\lambda^2(\tau)}-\frac{\lambda(\tau)}{\lambda^2(t}\right]\right]d\tau$$

Since $\chi_{ss}=(2-\alpha_B)\rho t_B^{-1}$, in our previous paper, the model is expressed as:

$$\sigma(\vec{x},t)=\left[\mu\rho+\mu\overline{\gamma}_\infty\frac{t_B}{2-\alpha_B}\left(1+(\alpha_B-1)\frac{t}{t_B}\right)^{\frac{2-\alpha_B}{1-\alpha_B}}\right]\left[\lambda(t)-\frac{1}{\lambda^2(t)}\right] \tag{3.13}$$

$$+\mu_j\overline{\gamma}_\infty\int_0^t\phi_B\left(\frac{t-\tau}{t_B}\right)\left[\frac{\lambda(t)}{\lambda^2(\tau)}-\frac{\lambda(\tau)}{\lambda^2(t)}\right]d\tau$$

These two equations are identical to each other and in this study, we will use Eq. (3.13) for PVA gel. In Eq. (3.13), the gel constitutive model is completely determined by 4 material parameters $\mu\rho,\ \alpha_B,\ t_B,$ and $\mu\overline{\gamma}_\infty$.

3.3 Notations for stress histories

Since we have multiple parameters in these constitutive models, for simplicity, we express a set of parameters as a vector. For example, for PVA model, there are 4 material parameters $\mu\rho,\ \alpha_B,\ t_B,$ and $\mu\overline{\gamma}_\infty$. Hence a parameter set is specified by a 4 dimensional vector $\vec{x}=(\mu\rho,\ \alpha_B,\ t_B,\ \mu\overline{\gamma}_\infty)^\top\in\Omega\subset\mathbb{R}^4$. Here Ω means the parameter space for the constitutive model.

According to our theory [20], in an uniaxial tension test where the stretch ratio $\lambda(t)$ is prescribed, the nominal stress $\sigma_j(t)$ corresponding to the material parameter set $\vec{x}_j=(\mu_j\rho_j,\ \alpha_{Bj},\ t_{Bj},\ \mu_j\overline{\gamma}_{\infty j})^\top$ is

$$\sigma_j(t)\equiv\sigma(\vec{x}_j,t) \tag{3.14}$$

And the stress history from 0 to $m\Delta t$ as

$$\vec{\sigma}(\vec{x}_j)\equiv(\sigma(\vec{x}_j,\Delta t),\sigma(\vec{x}_j,2\Delta t),\cdots,\sigma(\vec{x}_j,m\Delta t))^\top \tag{3.15}$$

CHAPTER 4

MACHINE LEARNING BASED PARAMETER FITTING FOR CONSTITUTIVE MODELS

4.1 Introduction

Theory plays an important role in the development of constitutive models. In the past two decades, many rate-dependent constitutive models have been developed to study the time-dependent behavior of soft materials made of dynamic networks as well as the flow of solvent in polymer gels [21, 31]. The complex micromechanics governing mechanical behavior requires many material parameters to construct a constitutive model with good predictive capability. For example, Mao et al. [32]. has developed a constitutive model for a hydrothermally activated malleable covalent network polymer. This model has 24 material parameters. Lu et al. [19] developed a 12 parameter constitutive model which incorporates viscoelasticity and Mullins effect to study the time dependent mechanical responses of four soft materials. Mao et al. [33] developed a large deformation viscoelasticity model to study the behavior of a double network hydrogel consisting of a covalently crosslinked polyacrylamide and an ionically crosslinked alginate network. This model has 18 material parameters. Chester [31] has developed a 10 parameters constitutive model to study the coupling of poroelasticity and viscoelasticity in polymer gels. Tang et al. [34] have developed a micro-stress based viscoelastic model to describe the viscoelasticity of polymers. This model has 9 material parameters.

In physically based constitutive models, some material parameters can be determined based on their physical significance, while others are typically cal-

ibrated manually or through an optimization process. For example, Crespo-Cuevas et al. [35] use transient network theory to develop a physical based model to quantify the poro-viscoelasto-plasticity of an Agarose gel. To estimate the material parameters in their model, they compare experimental creep and stress relaxation data with finite element simulations. They start the finite element simulation with some initial guesses of the material parameters and then update the input values iteratively using a minimization algorithm in MATLAB.

For complex constitutive models with a large number of parameters, fitting can be extremely challenging since computation can be time consuming even with an efficient optimization scheme. In this work, we highlight an alternative method that combines singular value decomposition (SVD) and neural networks (NN) to address this challenge. In the past few years, there has been intense interest in using machine learning techniques to solve solid mechanics problems [36, 37]. One approach is to train regression trees or neural networks to quickly solve a specific type of boundary value problem in solid mechanics. For example, Liu et al. [38] have shown that machine learning can rapidly determine the fracture toughness of a pre-notched pentagonal cross-section microcantilever loaded at its end. The machine learning solutions for different cantilever geometries agreed well with finite element results.

A different approach is to use machine learning to construct constitutive models, that is, to provide mechanical responses without using analytic constitutive equations. For example, Wang et al. [39] used a temporal convolutional network to simulate the ultra-long-history-dependent stress-strain relationship of reinforced concrete. Saharuddin et al. [40] used artificial neural network and extreme learning machine to simulate the mechanical behavior of a magnetorhe-

ological elastomer. Masi et al. [41] proposed a thermodynamics-based artificial neural network and applied their model to study the behavior of elasto-plastic solids.

Although there are a few papers that discuss parameter determination using machine learning [42, 43, 44], we have not found any published work using machine learning to determine material parameters in complex constitutive models. As we will demonstrate later, machine learning provides an efficient means to determine these material parameters. Our method has certain advantages over traditional nonlinear fitting methods such as the Levenberg-Marquardt algorithm [45, 46, 47]. This method also preserves the physical meaning of analytic constitutive models.

The basic idea is to train a ML method to determine the optimal material parameters given the constitutive model and experimental data from several different types of tests. For each type of experiment, e.g., a relaxation test, our training set consists of many stress histories associated with the experiment. Each stress history corresponds to a parameter set. These stress histories are stored as rows in a stress history matrix. We apply SVD to this stress matrix and use the dominant principal components as outputs of the neural network (input to ML method is the material parameters). Here we note that SVD has been employed for many years to analyze and reduce the size of training or experimental data [48]. It has been successfully utilized by researchers in many fields, such as the analysis of spectroscopic data [49], of dynamics simulations [50], and the genome-wide expression data processing [51]. SVD can also serve as a noise filter and a small subset of singular values and vectors can effectively represent the experimental data [52]. We then use the trained network to gener-

ate a very large number of stress histories. We determine the optimal parameter set by finding the stress history that best fits the experimental data.

We test our ML framework on three different soft hydrogels with very different time dependent behavior. Specifically, the constitutive model of these gels has 4, 9 and 13 material parameters respectively. For each gel, we perform four types of uniaxial tension experiments. These experiments provide data to train the ML method.

4.2 Singular value decomposition for constitutive models

For a $n \times m$ matrix A with rank r, it can be factorized into

$$A = U\Sigma V^\top \tag{4.1}$$

where

$$U = [\vec{u}_1, \vec{u}_2, \cdots, \vec{u}_r],\ V = [\vec{v}_1, \vec{v}_2, \cdots, \vec{v}_r] \textit{ and } U^\top U = V^\top V = I_{r\times r} \tag{4.2}$$

$$\Sigma = diag(s_1^2, s_2^2, \cdots, s_r^2) \textit{ for singular values } s_1^2 \geq s_2^2 \geq, \cdots, \geq s_r^2 > 0.$$

The columns of V, a $m \times r$ matrix, denoted by $\vec{v}_k \in \mathbb{R}^m,\ 1 \leq k \leq r$, form an *orthonormal basis* of the row space of A. The matrix U, a $n \times r$ matrix, also has rank r; the non-zero columns of U, denoted by $\vec{u}_k,\ 1 \leq k \leq r$ are orthonormal vectors in $\mathbb{R}^n$ and form a basis for the column space of A.

For many matrices of real-world data, the diagonal entries in Σ decay rapidly [53]. That is, there exists a positive integer r^* such that

$$\sum_{k=1}^{r^*} s_k^2 \gg \sum_{k=r^*+1}^{r} s_k^2, \quad r^* \ll r \tag{4.3}$$

Thus, the matrix A can be approximated by a smaller rank-r^* matrix, A_{r^*}, i.e.,

$$A \approx A_{r^*} = U_{r^*}\Sigma_{r^*}V_{r^*}^\top = s_1^2\vec{u}_1\vec{v}_1^\top + s_2^2\vec{u}_2\vec{v}_2^\top + \cdots + s_{r^*}^2\vec{u}_{r^*}\vec{v}_{r^*}^\top \tag{4.4}$$

4.2.1 Stored histories stored in computer

As part of the effort to construct the training data set, we construct the stress matrix first. We sample $|\Omega_T|$ different parameter vectors $\vec{x}_1, \vec{x}_2, \cdots, \vec{x}_{|\Omega_T|}$ from the parameter space Ω, where $|\Omega_T|$ depends on the number of parameters in the constitutive model. Larger values of $|\Omega_T|$ may be chosen for constitutive models with larger number of parameters. The value of $|\Omega_T|$ of different models in this paper will be specified later. By putting all those parameter vectors together, we can get a $|\Omega_T| \times p$ parameter matrix, i.e.,

$$X = [\vec{x}_1, \vec{x}_2, \cdots, \vec{x}_{|\Omega_T|}]^\top, \tag{4.5}$$

which is also called the matrix of the training input. The superscript $\top$ denotes matrix transpose.

For each $\vec{x}_j,\ 1 \le j \le |\Omega_T|$, we compute the stress history $\vec{\sigma}^\top(\vec{x}_j)$ as a function of time t for *the same stretch history* using the constitutive model. This stress history is stored as the j^{th} row vector

$$\vec{\sigma}^\top(\vec{x}_j) = \Big(\sigma(\vec{x}_j, \Delta t), \sigma(\vec{x}_j, 2\Delta t), \cdots, \sigma(\vec{x}_j, \zeta\Delta t)\Big) \tag{4.6}$$

The schematic for generating the stress matrix A is illustrated in Fig. 4.1. The numerical calculations begin at $t = \Delta t$, where Δt is a small time increment.

In general, A is a fairly large matrix, e.g. $|\Omega_T| \sim 10^3$, and $\zeta\Delta t \sim 10^1$ to 10^3 with $\Delta t = 0.1s$, then $\zeta \sim 10^2$ to 10^4 and the matrix has up to 10 million elements.

	Δt	$2\Delta t$	$\cdots$	$\zeta\Delta t$
$\vec{x}_1$	$\sigma(\vec{x}_1, \Delta t)$	$\sigma(\vec{x}_1, 2\Delta t)$		$\sigma(\vec{x}_1, \zeta\Delta t)$
$\vdots$				
$\vec{x}_j$	$\sigma(\vec{x}_j, \Delta t)$	$\sigma(\vec{x}_j, 2\Delta t)$		$\sigma(\vec{x}_j, \zeta\Delta t)$
$\vdots$				
$\vec{x}_{\lvert\Omega_T\rvert}$	$\sigma(\vec{x}_{\lvert\Omega_T\rvert}, \Delta t)$	$\sigma(\vec{x}_{\lvert\Omega_T\rvert}, 2\Delta t)$		$\sigma(\vec{x}_{\lvert\Omega_T\rvert}, \zeta\Delta t)$

Figure 4.1: Stress matrix for $|\Omega_T|$ sets of parameters. The loading history is the same for all different parameters in this matrix.

The information stored in the stress matrix A reflects how material parameters control stress histories. However, since the stress histories in this matrix are constructed according to the constitutive model, they should be correlated. Hence one anticipates that the data in this matrix can be compressed and the information in this matrix can be extracted using SVD, which is described below.

4.2.2 SVD for stress matrix

Suppose the rank of the stress matrix A is r. The compact SVD of the rank-r $|\Omega_T| \times \zeta$ matrix A can be factorized into

$$A = U\Sigma V^T \tag{4.7}$$

From section 4.2.1, we known that this matrix A can be approximated by a matrix A_{r^*}

$$A \approx A_{r^*} = U_{r^*}\Sigma_{r^*}V_{r^*}^\top = s_1^2\vec{u}_1\vec{v}_1^\top + s_2^2\vec{u}_2\vec{v}_2^\top + \cdots + s_{r^*}^2\vec{u}_{r^*}\vec{v}_{r^*}^\top \tag{4.8}$$

With this definition, we can get that the j^{th} row of A can be approximated as

$$\vec{\sigma}^{\top}(\vec{x}_j) \approx s_1^2 u_{1j} \vec{v}_1^{\top} + s_2^2 u_{2j} \vec{v}_2^{\top} + \cdots + s_{r^*}^2 u_{r^* j} \vec{v}_{r^*}^{\top} = \vec{\psi}^{\top}(\vec{x}_j) V_{r^*}^{\top}, \quad 1 \leq j \leq |\Omega_T| \tag{4.9}$$

where u_{kj} denotes the j^{th} component of the vector $\vec{u}_k$ and $\vec{\psi}(\vec{x}_j)$ is a row vector of length r^* defined by

$$\vec{p}(\vec{x}_j) = \left(s_1^2 u_{1j}, s_2^2 u_{2j}, \cdots, s_{r^*}^2 u_{r^* j}\right)^{\top} \tag{4.10}$$

Since the rows of $V_{r^*}^{\top}$ or $B = \left\{\vec{v}_k^{\top},\ 1 \leq k \leq r^*\right\}$ is an approximate orthonormal basis for the row space of A, the entries of $\vec{\psi}(\vec{x}_j)$ represent the coordinates of stress history $\vec{\sigma}^{\top}(\vec{x}_j)$ with respect to B. Here we state a key assumption:

Assumption 1: *If one keeps sampling from a fixed probability distribution on* Ω*, and calculate and store the stress histories as rows in A (i.e. the number of rows of A,* $|\Omega_T|$*, increases accordingly),* $V_{r^*}^{\top}$ *or* $B = \left\{\vec{v}_k^{\top},\ 1 \leq k \leq r^*\right\}$ *will converge.*

Assumption 1 states that, for a *given loading history*, all stress histories generated by the constitutive model are linear combinations of the *same* basis. This is a reasonable assumption because there must exist some relation between stress histories since they are generated by the same constitutive model. We can therefore use the same orthonormal basis B in the row space to compute $\vec{\sigma}^{\top}(\vec{x}_j)$ where $\vec{x}_j$ *can be any parameters in* Ω. This means we can find a good approximation of $\vec{\sigma}^{\top}(\vec{x}_j)$ in Ω *without using the constitutive model if we can find* $\vec{\psi}(\vec{x}_j)$, the projection of $\vec{\sigma}^{\top}(\vec{x}_j)$ on B. This allows us to dramatically increase the data set without doing additional computations.

Now the problem is how to determine $\vec{\psi}(\vec{x}_j^*)$ if the parameters vector $\vec{x}_j^*$ is not in the training set. In other words, $\vec{x}_j^* \in \Omega_P,\ \Omega_P \cap \Omega_T = \emptyset$.

4.3 Machine learning framework for model fitting

In this part, we introduce the use of machine learning methods to predict the value of $\vec{\psi}(\vec{x}_j^*)$ for $\vec{x}_j^* \in \Omega_P,\ \Omega_P \cap \Omega_T = \emptyset$.

It is well known that there are many types of machine learning methods and they usually have their unique features for specific problems [54, 55]. To make our methods more general, in this section, we will first introduce a machine learning framework for constitutive model fitting without considering specific machine learning methods. In the next two sections, we will implement this framework with two different machine learning methods and discuss their effectiveness in the model fitting problem.

4.3.1 Preprocessing

Preprocessing means preparing the training set for machine learning methods. What is the input and the output, and how can we generate some input and output data for following training process? This workflow is shown in Fig. 4.2. The first thing we need to do is to choose $|\Omega_T|$ sets of parameters and calculate their stress histories, using the constitutive model. Then, as we mentioned before, we can put all those stress histories together to be a stress matrix, as shown in Fig. 4.2 (a) and (b). After that, singular value decomposition is applied to the stress matrix and we can get its U, Σ and $V^\top$. From Σ, we can plot the curve of singular values versus the number of terms to determine the value of r^*, as shown in Fig. 4.2 (c). With the value of r^*, we can then determine the basis B from $V^\top$, as shown in Fig. 4.2 (d).

Now it is clear that for this machine learning framework, the input is the model parameters and the output is the principal components. Note again that our purpose for this machine learning framework is to find the relationship between model parameters and principal components of stress histories, for a given loading history, so this framework knows nothing about the basis.

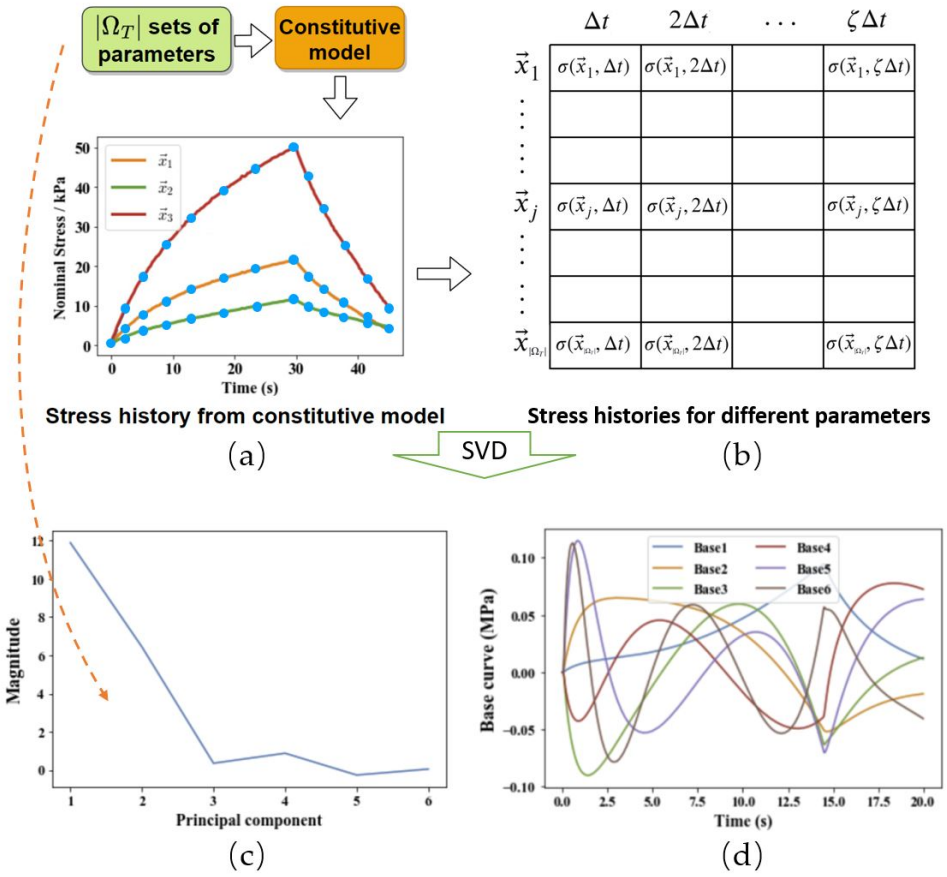

Figure 4.2: Preprocessing of the machine learning framework.

4.3.2 Training and validation

With the training set, the next step is to implement the training and validation of this machine learning framework, which is the most important process in

determining the final prediction quality. The workflow is shown in Fig. 4.3. First, the training set with $|\Omega_T|$ sets of parameters and principal values are fed to the specific ML method for training, as shown in Fig. 4.3 (a). After training, we randomly choose $|\Omega_V|$ sets of parameters from the parameter space Ω such that $\Omega_T \cap \Omega_V = \emptyset$. Then we use the trained ML method to get the predicted principal components $\vec{\psi}_{ML}(\vec{x}_j),\ \vec{x}_j \in \Omega_V$, while we also calculate the real principal components $\vec{\psi}(\vec{x}_j),\ \vec{x}_j \in \Omega_V$ using the constitutive model and basis in Fig. 4.2 (d). $\vec{\psi}_{ML}(\vec{x}_j)$ will be compared with $\vec{\psi}\vec{x}_j)$ for all $\vec{x}_j \in \Omega_V$, as shown in Fig. 4.3 (b). If the error between them is small, we adopt the training results and go to the next step, otherwise we will retrain the machine learning method, or set $\Omega_T = \Omega_T \cup \Omega_V$ and then retrain the machine learning method.

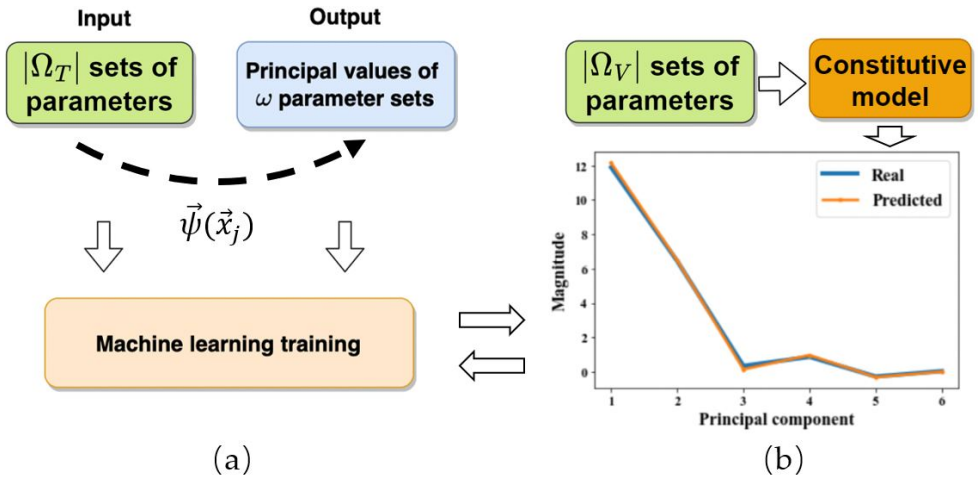

Figure 4.3: Training and validation of ML method

4.3.3 Prediction and fitting

After training and validation, the ML method should be able to predict the principal components of any parameters in the parameter space Ω fast and precisely; we can use this fast prediction for fast parameter fitting.

Let us suppose we carried out a uniaxial experiment with some loading history. We first take the stress history from this experiment to form a vector and then calculate its projection on the basis of B to determine its principal values. Then, we uniformly randomly select a large number of new parameter vectors in a subset Ω_P of the parameter space Ω and predict their principal vectors using the trained neural network. If Ω_P is large enough, there should exist some parameter vectors which fit the experimental data well. To ensure good fitting, we choose $|\Omega_P| == 1000|\Omega_T|$, so the size of prediction set is larger than 1 million. It is very time-consuming to calculate the constitutive model 1 million times (time is roughly 1s per calculation). However, as we shall see below, it is very fast for the ML method to predict principal components for 1 million parameter vectors. The optimal set of parameters should have principal components closest to the experimental principal components, as defined by Eq. (4.11) below.

$$\vec{x}_{opt} = argmin_{\vec{x}_j \in \Omega_P} \frac{||\vec{\psi}_{ML}(\vec{x}_j) - \vec{\psi}_{exp}||}{||\vec{\psi}_{exp}||} \tag{4.11}$$

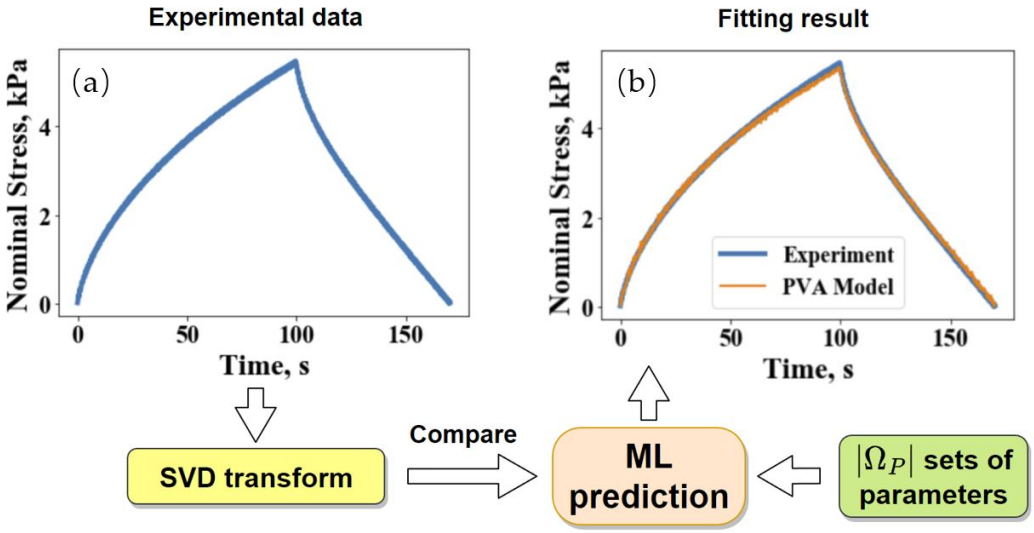

Figure 4.4: Prediction and fitting

Often, one can obtain a set of parameters that fits one experiment extremely well. A more stringent test of a constitutive model is to find a set of parameters

which works for a wide variety of loading histories. This situation is more complicated since the basis B and principal components are different for different loading histories. Here we adopt one of the most straightforward methods, that is, we train different neural networks independently for different loading histories, and then make predictions for different loading histories, using the same prediction set. The optimal parameter vector $\vec{x}_{opt}$ is the one with the smallest average error among all experiments, i.e.,

$$\vec{x}_{opt} = argmin_{\vec{x}_j \in \Omega_P} \frac{1}{N} \sum_{i=1}^{N} \frac{\|\vec{\psi}_{ML}^{(i)}(\vec{x}_j) - \vec{\psi}_{exp}^{(i)}\|}{\|\vec{\psi}_{exp}^{(i)}\|} \tag{4.12}$$

where N means there are N experiments in total, and i means the i^{th} loading history.

4.4 Gaussian process method

4.4.1 Gaussian Process regression introduction

From Eq. (4.5) we already know X is the matrix of parameters in the training set, now let's define another parameter matrix as

$$X^* = [\vec{x}_1^*, \vec{x}_2^*, \cdots, \vec{x}_{|\Omega_P|}^*]^\top, \quad \vec{x}_j^* \in \Omega_P, \quad 1 \leq j \leq |\Omega_P| \tag{4.13}$$

which is called the matrix of the prediction inputs. The theory of Gaussian process states that if the function $y(\vec{x}_j)$ conforms to a Gaussian Process on Ω, the distribution over any set of inputs belonging to Ω must have a joint multivariate Gaussian distribution, i.e.,

$$\begin{bmatrix} \vec{y} \\ \vec{y}^* \end{bmatrix} \sim \mathcal{N}\left(0, \begin{bmatrix} [K_{XX}] + \delta^2[I] & [K_{XX^*}] \\ [K_{X^*X}] & [K_{X^*X^*}] \end{bmatrix}\right) \tag{4.14}$$

In Eqn. 4.14, δ^2 represents the noise level and can be treated mathematically as a regularizer (e.g. from experiments or numerical calculation), and $[I]$ is the identity matrix. Here $[K_{XX}]$, $[K_{XX^*}]$, $[K_{X^*X}]$ and $[K_{X^*X^*}]$ are $|\Omega_T| \times |\Omega_T|$, $|\Omega_T| \times |\Omega_P|$, $|\Omega_P| \times |\Omega_T|$ and $|\Omega_P| \times |\Omega_P|$ matrices, respectively, and they are called covariance matrix [56]. How to get those matrices according to the training data will be introduced later. Now, if we already know the value of all those matrices, given $\vec{y}$, the Gaussian process regression predicts that

$$\overline{\vec{y}^*} = [K_{X^*X}]\left[[K_{XX}] + \delta^2[I]\right]^{-1}\vec{y} \tag{4.15}$$

where $\overline{\vec{y}^*}$ is the mean value of the random variable, $\vec{y}^*$; it represents the best estimation of the output value for inputs $\vec{x}_j^* \in \Omega$, $1 \le j \le |\Omega_P|$ when we already know the values of the training set $\left\{ y(\vec{x}_j) \mid \vec{x}_j \in \Omega,\ 1 \le j \le |\Omega_T| \right\}$. The variance of $\vec{y}^*$ is given by:

$$var(\vec{y}^*) = diag\left([K_{X^*X^*}] - [K_{X^*X}]\left[[K_{XX}] + \delta^2[I]\right]^{-1}[K_{XX^*}]\right) \tag{4.16}$$

Eq. (4.16) measures the variablity of $\vec{y}^*$ and provides useful information on the reliability of the estimate given by Eq. (4.15). The next step is to identify the random variables $y(\vec{x}_j)$ and $y(\vec{x}_j^*)$ in the Gaussian process, $\mathcal{GP}$, with physical quantities in our problem.

4.4.2 Gaussian process metamodeling for constitutive models

Since we already know the definition of X and X^*, now the most important thing would be, what should $\vec{y}$ and $\vec{y}^*$ be, in order to predict the principal values of parameter vectors that are not in the training inputs without using this constitutive model?

Assumption 2: *Each component in $\vec{\psi}(\vec{x}_j)$ and $\vec{\psi}(\vec{x}^*_j)$ conforms to an independent Gaussian process on Ω.*

Recall that after SVD compression, $\vec{\psi}(\vec{x}_j)$ and $\vec{\psi}(\vec{x}^*_j)$ both contain r^* components, where r^* is the number of dominant singular values of A. Each component of these coordinate vectors $\vec{\psi}(\vec{x}_j)$ and $\vec{\psi}(\vec{x}^*_j)$ will now be identified as the random variable $y(\vec{x}_j)$ or $y(\vec{x}^*_j)$ in a $\mathcal{GP}$. We further assume these $\mathcal{GP}$s are independent. We have r^* independent $\mathcal{GP}$s. Specifically, we define

$$\psi_k(\vec{x}_j) = k^{th} \textit{ component of } \vec{\psi}(\vec{x}_j), \quad \vec{x}_j \in \Omega \tag{4.17}$$

For the rest of this paper, $\psi_k(\vec{x}_j)$ or $\psi_k(\vec{x}^*_j)$ denote the k^{th} component of $\vec{\psi}(\vec{x}_j)$ or $\vec{\psi}(\vec{x}^*_j)$. The vectors $\vec{y}_k$, $k = 1, 2, \cdots, r^*$, which are the vectors of the training outputs in the k^{th} Gaussian process model $\mathcal{GP}_k$, correspond to $\vec{y}$ in Eq. (4.14):

$$\vec{y}_k \equiv \begin{pmatrix} \psi_k(\vec{x}_1) \\ \vdots \\ \psi_k(\vec{x}_{|\Omega_T|}) \end{pmatrix}, \quad k = 1, 2, \cdots, r^* \tag{4.18}$$

To predict $\vec{y}^*_k(\vec{x}^*_j)$, we train a total of ξ independent $\mathcal{GP}$s, namely $\mathcal{GP}_k$, $k = 1, 2 \cdots, \xi$, using the training set that comprises the matrix of the training inputs X and the vector of the training outputs $\vec{y}_k$ for $k = 1, 2 \cdots, \xi$. The training process will be discussed later. Using Eq. (4.15) we obtain

$$\overline{\vec{y}^*_k} = \begin{pmatrix} \overline{\psi_k}(\vec{x}^*_1) \\ \vdots \\ \overline{\psi_k}(\vec{x}^*_{|\Omega_P|}) \end{pmatrix} = [K_{X^*X}]_k \left[[K_{XX}]_k + \delta^2 [I] \right]^{-1} \vec{y}_k, \quad k = 1, 2, \cdots, r^* \tag{4.19}$$

where $\overline{\psi_k}(\vec{x}^*_j)$ is the *predicted mean value of k^{th} component of $\vec{\psi}(\vec{x}^*_j)$*. The subscript k in $[K_{XX}]_k$ and $[K_{X^*X}]_k$ indicates that the elements of these matrices are dependent on

$\vec{y}_k$. From Eq. (4.17) and Eq. (4.19) we obtain $\vec{\psi}_{GP}(\vec{x}_j^*)$ which is an approximation of $\vec{\psi}(\vec{x}_j^*)$, i.e.,

$$\vec{\psi}_{GP}(\vec{x}_j^*) = \left(\overline{\psi_1}(\vec{x}_j^*), \overline{\psi_2}(\vec{x}_j^*), \cdots, \overline{\psi_{r^*}}(\vec{x}_j^*)\right)^\top \approx \vec{\psi}(\vec{x}_j^*) \tag{4.20}$$

With the estimated value of $\psi(\vec{x}_j^*)$, the stress history corresponding to $\vec{x}_j^*$ is

$$\vec{\sigma}^\top(\vec{x}_j^*) \approx \vec{\psi}^\top(\vec{x}_j^*) V_{r^*}^\top \approx \vec{\psi}_{GP}^\top(\vec{x}_j^*) V_{r^*}^\top \tag{4.21}$$

Now, the stress history can be predicted from matrix-vector multiplications without solving for the stress using the constitutive model, as shown in Fig. 4.5.

We now have a better understanding of why SVD is first applied to the stress matrix. After SVD, each stress history can be represented by r^* quantities. To build metamodels for all those quantities, a total of r^* independent $\mathcal{GP}$ should be trained, namely $\mathcal{GP}_k$, $k = 1, 2 \cdots, r^*$. Note, in the original stress history matrix, each stress history is defined by ζ quantities, i.e., the number of columns of matrix A. As a result, to build metamodels for the constitutive model, a total of ζ independent $\mathcal{GP}$ are needed. Unfortunately, ζ is usually 10 to 1000 times larger than r^*, so applying Gaussian process directly to the matrix is extremely uneconomical.

4.4.3 Anisotropic RBF kernel and training

To determine $\psi_{GP}(\vec{x}_j^*)$, we need to specify and evaluate the covariance matrices in Eq. (4.15) and Eq. (4.19). There are many forms of covariance functions [56]. In this work we use the anisotropic RBF kernel which defines the elements of the covariance matrix $[K_{XX}]$ in Eq. (4.15) as

$$k_{x_j x_{j'}} \equiv k(\vec{x}_j, \vec{x}_{j'}) = \sigma_f^2 \exp\left(-\frac{1}{2}\sum_{d=1}^{q}(x_{jd} - x_{j'd})^2/\ell_d^2\right), \quad 1 \le d \le q \tag{4.22}$$

where the subscript d in x_{jd} denotes the d^{th} component of the parameter vector $\vec{x}_j \in \mathbb{R}^q$. ℓ_d is the *characteristic length* specific to x_{jd} while σ_f is the *signal variance*. This class of covariance functions naturally takes care of the coordinate-dependent scaling of the parameter vector by specifying a unique ℓ_d for the d^{th} coordinate of the parameter vector for $1 \leq d \leq q$. This property is especially suitable in our case where the parameters in a constitutive model usually have different units and scales. In the literature, the anisotropic RBF kernel has been successfully applied to material modeling [57, 58].

Let the set $\vec{\theta} = \{\ell_1^2, \ell_2^2, \cdots, \ell_q^2, \sigma_f^2\}$ denote the parameters in the covariance function. These components are called the hyperparameters of the machine learning model $\mathcal{GP}$. The characteristic lengths ℓ_d measure the distances in the parameter space when $y(\vec{x}_j)$ become uncorrelated [56]. ℓ_d characterizes the dependence of $y(\vec{x}_j)$ on the d^{th} component of $\vec{x}_j$, i.e., x_{jd}. A larger ℓ_d means that $y(\vec{x}_j)$ is smoother in x_{jd}. If ℓ_d is very large compared with the scale of x_{jd}, then $y(\vec{x}_j)$ is approximately linear in x_{jd}. If ℓ_d is very small compared to the scale of x_{jd}, then a small change of x_{jd} can lead to a dramatic change of $y(\vec{x}_j)$. The signal variance controls the range of the functions drawn from a $\mathcal{GP}$. Roughly, σ_f represents the absolute scale of the training outputs.

To find the optimal hyperparameters, we use Assumption 2 which states that $\left\{y_k(\vec{x}_j), \cdots, y_k(\vec{x}_\omega)\right\}$ have a joint multivariate Gaussian distribution whose covariance matrix $[K_{XX}]$ depends on the training inputs collected in X and $\vec{\theta}$, as indicated by Eq. (4.22). Thus, the probability density function of $\vec{y}_k$ given X and $\vec{\theta}$ is [56]

$$p(\vec{y}_k \mid X, \vec{\theta}) = \frac{\exp\left(-\frac{1}{2}\vec{y}_k^{\top}\left[[K_{XX}] + \delta^2[I]\right]^{-1}\vec{y}_k\right)}{\sqrt{(2\pi)^{|\Omega_T|}|[K_{XX}] + \delta^2[I]|}} \tag{4.23}$$

We remark that during training, the hyperparameters in $\vec{\theta}$ are variables and each element in $[K_{XX}]$ is a function of $\vec{\theta}$ (dark green box in Fig. 4.5) (b). In a nutshell, the training process is as follows: $k = 1, \cdots, r^*$, choose $\vec{\theta} = \vec{\theta}_k$ which made the observation of $\vec{y}_k$ most probable (dark boxes in Figure Fig. 4.5 (b)), i.e.,

$$\vec{\theta}_k = argmax_{\vec{\theta}} p(\vec{y}_k \mid X, \vec{\theta}) = argmax_{\vec{\theta}} \log p(\vec{y}_k \mid X, \vec{\theta}) \equiv argmax_{\vec{\theta}} \mathcal{L}_k(\vec{\theta}), \quad k = 1, 2, \cdots r^* \tag{4.24}$$

where $argmax_{\vec{\theta}} p(\vec{y}_k \mid X, \vec{\theta})$ denotes the $\vec{\theta}$ that maximizes $p(\vec{y}_k \mid X, \vec{\theta})$. The second equality in Eq. (4.24) is because the logarithmic function monotonically increases. $\mathcal{L}_k(\vec{\theta})$ denotes the log marginal likelihood of the observation of $\vec{y}_k$, which is

$$\mathcal{L}_k(\vec{\theta}) \equiv \log p(\vec{y}_k \mid X, \vec{\theta}) = -\frac{1}{2}\vec{y}_k^{\top}\left[[K_{XX}] + \delta^2[I]\right]^{-1}\vec{y}_k - \frac{1}{2}\log|[K_{XX}] + \delta^2[I]| - \frac{|\Omega_T|}{2}\log 2\pi \tag{4.25}$$

Numerical methods such as gradient based techniques are used to solve Eq. (4.24) for the optimal hyperparameters. In this work the `sklearn.gaussian_process.GaussianProcessRegressor` module implemented in Python is used to determine $\overline{\vec{y}^*}$ while the `L-BFGS-B` algorithm is used to maximize the log marginal likelihood function.

We use the set $\vec{\theta}_k = \{\ell_{k1}^2, \ell_{k2}^2, \cdots, \ell_{k\beta}^2, \sigma_{fk}^2\}$ to specify the optimized hyperparameters in the covariance function of the k^{th} Gaussian process machine learning model $\mathcal{GP}_k$ (light green boxes in Fig. 4.5 (b)). They uniquely define $\mathcal{GP}_k$ by Eq. (4.22). Thus, the covariance matrices $[K_{XX}]_k$ and $[K_{X^*X}]_k$ in Eq. (4.19) are $[K_{XX}]$ and $[K_{X^*X}]$ evaluated at $\vec{\theta}_k$. That is,

$$[K_{XX}]_k = [K_{XX}]|_{\vec{\theta}_k} \qquad [K_{X^*X}]_k = [K_{X^*X}]|_{\vec{\theta}_k} \tag{4.26}$$

All the processes above are summarized in Figure 4.5.

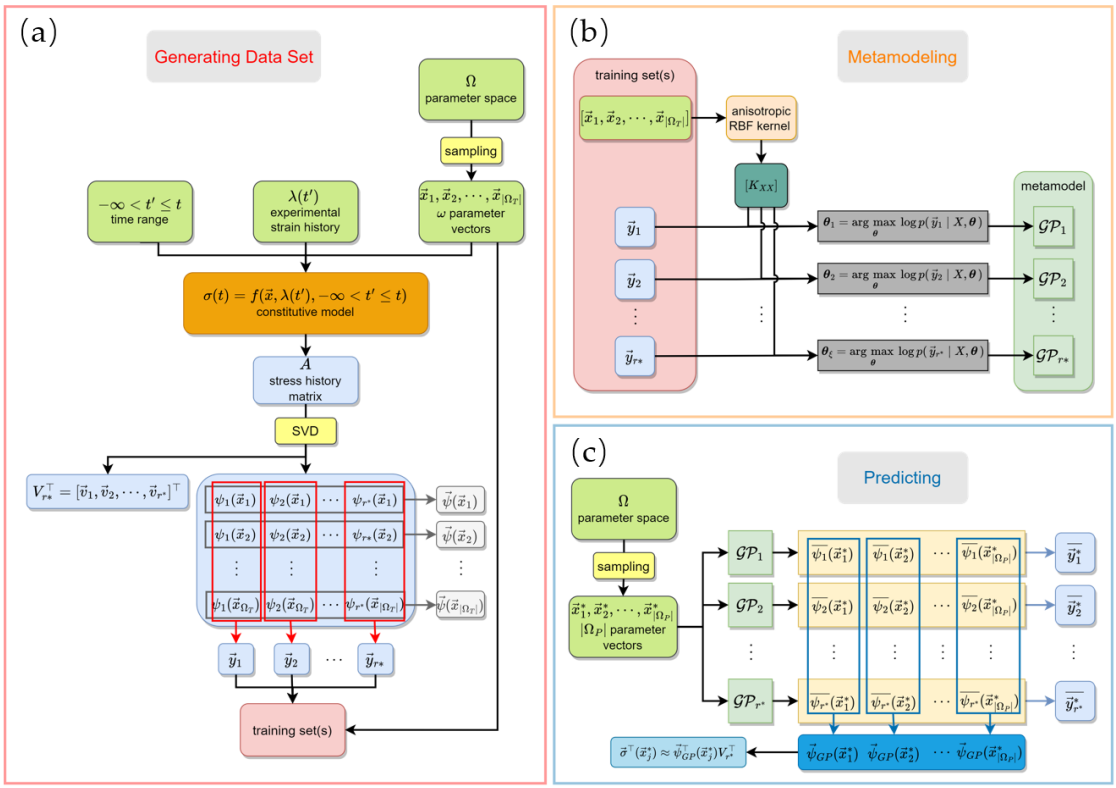

Figure 4.5: The overall flowchart for (a) generating the data set, (b) metamodeling of the constitutive behavior, and (c) predicting the stress history $\vec{\sigma}^\top(\vec{x}_j^*)$. The structure of the stress matrix A in (a) is shown in Fig. 4.1. Matrix $V_{r^*}^\top$ in (a) and (c) is the transpose of the V matrix in SVD but only with the first ξ columns. Each of the dark boxes in (b) represents an individual training process that is based on hyperparameter optimization by maximizing the log marginal likelihood.

4.4.4 Implementation of Gaussian process method on PVA gel

(This part is done with the help of Tianjiao Li at Cornell University, and more details can be found in A.1)

In this section, we are going to try fitting PVA constitutive model using Gaussian Process method. Here we first start $|\Omega_T| = 1000$.

We first conduct SVD on the stress matrix $A^{(i)}$, $1 \leq i \leq 4$, where each matrix has $|\Omega_T|$ rows generated by solving our constitutive model. Fig. 4.6 shows the SVD of $A^{(i)}$. Note that the singular values of $A^{(i)}$ decay rapidly to zero for $k > 3$ in all four strain histories. This shows that $r^* = 3$ is sufficient for accurately estimating the stresses for all four strain histories.

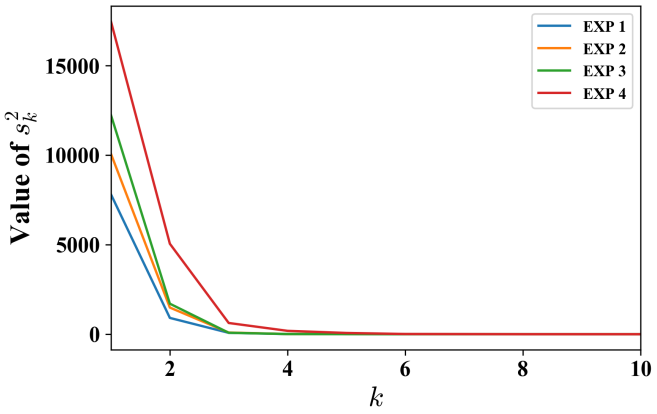

Figure 4.6: Singular values of four strain histories. The singular values for each strain history are presented by different color lines. s_k^2 values for $k > 10$ are not shown because they are too small compared with the first 4 singular values

As described earlier, the hyperparameters can provide useful information about our constitutive model. The optimized hyperparameters are listed in Table 4.1. Table 4.1 shows that the stress history is most sensitive to α_B, less sensitive to t_B and least sensitive to $\mu\rho$ and $\mu\bar{\gamma}_\infty$. Specifically, in all experiments, the characteristic length ℓ_1 is very large compared to the scale of $\mu\rho$ ($0 \leq \mu\rho \leq 15$),

this is consistent with Eq. (3.13) which indicates that the stress history depends almost linearly on $\mu\rho$. On the other hand, ℓ_2 is very small compared to the scale of α_B ($1.3 \leq \alpha_B \leq 1.9$), consistent with the fact that the stress history is very sensitive to α_B. Finally, ℓ_3 is very close to the scale of t_B ($0 \leq t_B \leq 1.5$) and ℓ_4 is 2 to 6 times larger than the scale of $\mu\overline{\gamma}_\infty$ ($0 \leq \mu\overline{\gamma}_\infty \leq 100$). This is again consistent with Eq. (3.13) which shows that stress changes smoothly (but not linearly) with t_B and $\mu\overline{\gamma}_\infty$.

As we discussed in section 4.3.2, we randomly choose 1000 random parameter vectors from all of $\vec{x}_j^*$ for validation. We then compute the $\vec{\psi}(\vec{x}_j^*)$ using Eq. (3.13) for both the cyclic and relaxation tests and compare them to the predicted $\vec{\psi}_{GP}(\vec{x}_j^*)$ using the Gaussian process models. For each test and each component of $\vec{\psi}(\vec{x}_j^*)$, the prediction of our constitutive model vs the prediction of the Guassian process models is shown in Figure 4.7. In all cases, the predicted value is practically the same as the computed value. This means the predicted $\vec{\psi}_{GP}(\vec{x}_j^*)$ by the models is highly accurate and we can determine stress histories outside the training set without integrating the constitutive model.

We then assess whether the material parameters determined by our method can accurately fit experimental data. Fig. 4.8 compares the experimental stress-strain curves predicted with the curves calculated with the rank 1^{st} set of parameters given by Eq. (4.12) for the 4 different experiments. The agreement between experiments and theory is excellent.

Here we can see that we are very lucky to get low validation error and good fitting results with one time training for each experiment. This is because PVA model only contains 4 parameters so training size of 1000 is big enough to represent the relationship between parameters and principal components of this

Table 4.1: Summary of optimized hyperparameters. Since $r^* = 3$ and $N = 4$, we have a total 12 different sets of optimized hyperparameters. To simplify notation, we omit the subscript k for each component. ℓ_1, ℓ_2, ℓ_3 and ℓ_4 are the characteristic lengths of $\mu\rho$, α_B, t_B and $\mu\bar{\gamma}_\infty$ respectively, as defined in Eq. (4.22)

	Train	σ_f	ℓ_1 †	ℓ_2	ℓ_3	ℓ_4
EXP 1	$\vec{y}_1^{(1)}$	196	1.00×10^4	0.185	2.94	393
	$\vec{y}_2^{(1)}$	197	1.00×10^4	0.178	2.75	416
	$\vec{y}_3^{(1)}$	188	9.92×10^3	0.170	2.66	477
EXP 2	$\vec{y}_1^{(2)}$	164	1.00×10^4	0.199	2.66	381
	$\vec{y}_2^{(2)}$	148	1.00×10^4	0.189	2.54	408
	$\vec{y}_3^{(2)}$	144	9.98×10^3	0.194	1.85	491
EXP 3	$\vec{y}_1^{(3)}$	133	1.00×10^4	0.213	2.39	367
	$\vec{y}_2^{(3)}$	123	1.00×10^4	0.199	2.23	428
	$\vec{y}_3^{(3)}$	74	7.52×10^3	0.224	1.07	461
EXP 4	$\vec{y}_1^{(4)}$	145	1.00×10^4	0.213	2.36	377
	$\vec{y}_2^{(4)}$	266	1.00×10^4	0.174	2.91	437
	$\vec{y}_3^{(4)}$	238	9.66×10^3	0.170	2.21	468

† the upper limit of ℓ_1 in the optimization is set to be 1.00×10^4.

model. Another thing one may discover is that the variance is not used in this fitting process, which should be useful because it provides information on the reliability of the Gaussian process estimation. So we did an active learning study for Gaussian Process in Appendix 2, which demonstrates how the variance could help us update the training set efficiently.

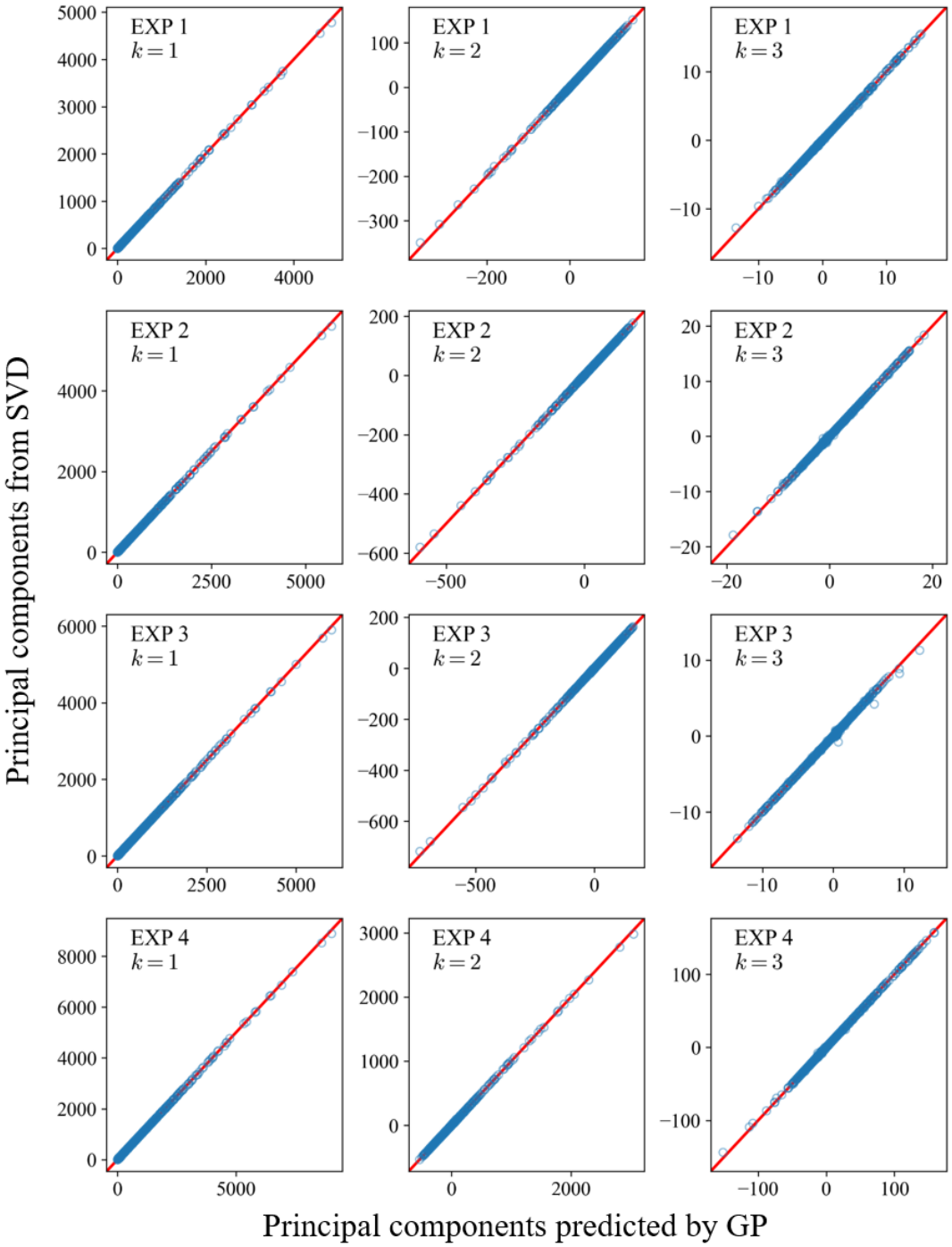

Figure 4.7: Predicted projection $\overline{\psi_k}(\vec{x}_j^*)$ using GP versus projections $\psi_k(\vec{x}_j^*)$ obtained using constitutive model for four different types of experiments.

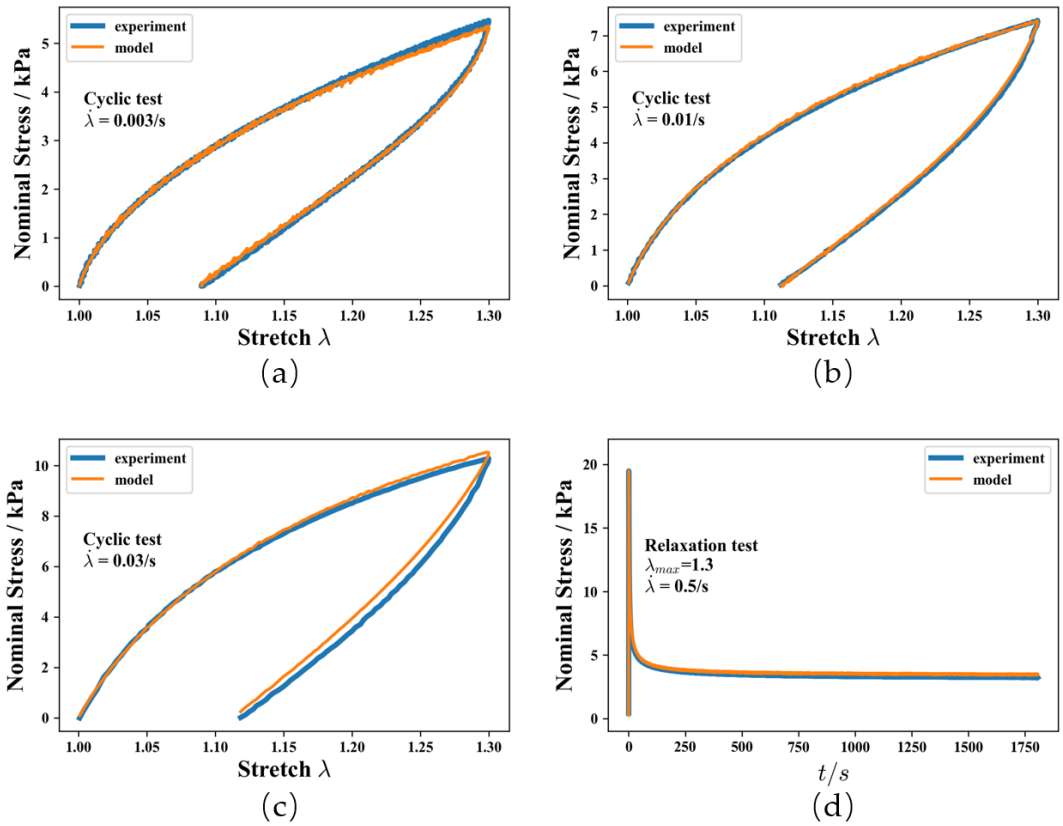

Figure 4.8: Comparison of model prediction with experiments. the model parameters are $(\mu\rho,\ \alpha_B,\ t_B,\ \mu\bar{\gamma}_\infty) = (4.744kPa, 1.579, 0.841s, 13.48kPa)$

4.4.5 Gaussian process for more complex models

One limitation of our method is that the basic computational complexity of Gaussian process is the size of the training set ω to the third power, i.e., $O(\omega^3)$. When the size of the parameter space becomes larger, larger training set is required to effectively represent the parameter space, which will potentially lead to low computational efficiency.

As we mentioned before, the Gaussian process is implemented using the `GaussianProcessRegressor` module in `sklearn` package, which is running on CPU. When we apply the same code to c-PA and p-PA models, the fitting results for 1000 training size are very bad so we iterate to increase the training size. However, when the training size increases to 3000 for c-PA model (with 9 parameters), it takes us more than 5 hours to train even one Gaussian process, which is comparable to the direct calculation of the constitutive models.

One possible way to solve this problem is to train the Gaussian process on GPU, which can accelerate the training process hundreds of times faster with the help of parallel computation. One good package for Gaussian Process on GPU is `GPytorch` [59]. However, in this study, the implementation of Gaussian Process through `GPytorch` encounters some numerical issues (may relate to the noise term and its optimization in `GPytorch`), and we are not able to solve them at the time of this study. But there should be no theoretical obstacle for solving this problem and we will be happy if one could implement our methods using parallel computation.

4.5 Adaptive neural network method

4.5.1 NN for consitutive models

There are various types of NN [54, 55]. Here we choose the deep neural network (DNN) for its simplicity. A DNN always contains three types of layers: input layer, hidden layer, and output layer. For our parameter fitting problem, the input layer is the parameters of the constitutive model so the number of input nodes equals q; the output layer is the first r^* principal components, so the number of output nodes is r^*.

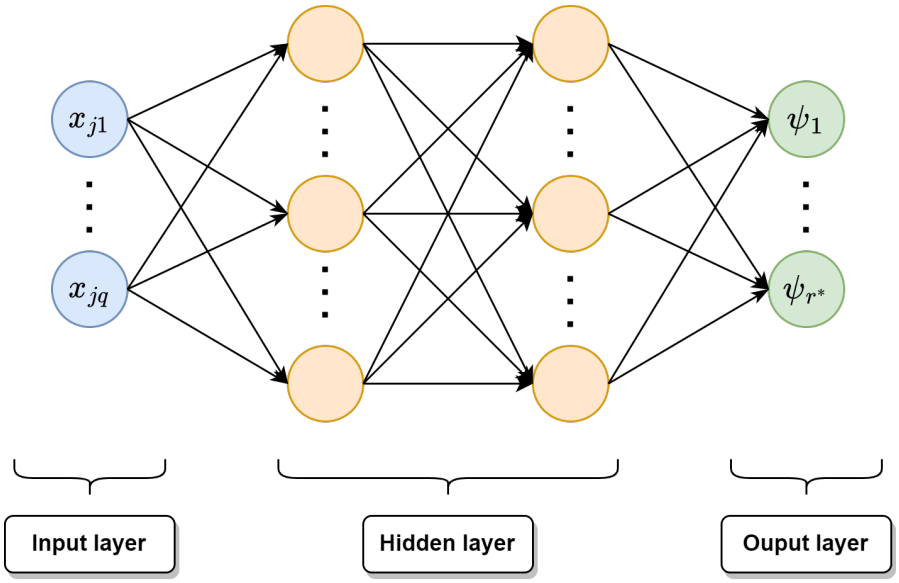

Figure 4.9: Schematics of DNN. The number of nodes in the input layer equals the number of modal parameters, q, and the number of nodes in the output layer is the number of singular values needed to approximate the stress history, r^*. The outputs are the principal components associated with a particular stress history. Only two hidden layers are shown but more can be used.

There can be many hidden layers. More layers or more nodes in each hidden layer means greater ability to simulate complex models but usually requires larger training sets to reach the best prediction result. In Fig. 4.9, we show an

example of two hidden layers. Each node in the first hidden layer (say node k) takes as input the q input values of a parameter vector $\vec{x}_j$ and computes its output $o_{1k}(\vec{x}_j)$ as:

$$o_{1k}(\vec{x}_j) = ln\left(1 + exp(\vec{w}_{1k} \cdot \vec{x}_j + b_{1k})\right) \tag{4.27}$$

where $ln(1 + exp())$ is the Softplus activation function. Here the components of $\vec{w}_{1k}$ are the weights of the k^{th} node in the first hidden layer, $\cdot$ is the dot product of two vectors and b_{1k} is the bias.

Similarly, the nodes of the 2^{nd} hidden layer will take as input the outputs of the first hidden layer $\vec{o}_1 = (o_{11}, o_{12}, \cdots, o_{1h_1})^\top$ (h_1 denotes the total number of nodes in the first hidden layer), and so on (using different weights and biases). For example, for the second hidden layer,

$$o_{2k}(\vec{o}_1) = ln(1 + exp(\vec{w}_{2k} \cdot \vec{o}_1 + b_{2k})) \tag{4.28}$$

Finally, the output is given by

$$\psi_k(\vec{x}_j) = \vec{w}_{3k} \cdot \vec{o}_2 + b_{3k}, \qquad k = 1, 2, \cdots, r^* \tag{4.29}$$

where $\vec{w}_{3k}$ and b_{3k} are the weights (in our case the principal components) and bias of the last hidden layer. Here $\vec{o}_2$ is the output vector of hidden layer 2.

We define the training error by

$$err_{train} = \frac{1}{|\Omega_T|} \sum_{\vec{x}_j \in \Omega_T} \frac{||\vec{\psi}_{NN}(\vec{x}_j) - \vec{\psi}(\vec{x}_j)||}{||\vec{\psi}_{NN}(\vec{x}_j)||} \tag{4.30}$$

where $\vec{\psi}_{NN}(\vec{x}_j)$ is the output principal vector of the NN associated with $\vec{x}_j$ in the training set and $\vec{\psi}(\vec{x}_j)$ is the computed principal vector obtain using SVD. Ω_T is the training set, so $|\Omega_T|$ is the number of elements in the training set. Training means we tune all the weights and biases in the neural network so err_{train} is less than an assigned small number. The tuning process is done using the gradient descent method. Details are given in A.3.

4.5.2 Verification and adaptive neural network

In the discussion above, we show an example of two hidden layers. However, different constitutive models require different numbers of hidden layers and training set sizes to achieve the best prediction. For example, a constitutive model with fewer material parameters usually requires fewer hidden layers and a smaller training set, whereas a model with more parameters requires more hidden layers and a larger training set. Our goal is to design an accurate and efficient algorithm to determine material parameters for any constitutive model. In the following, we design an adaptive network to update the neural network and training set automatically. The flow chart of our algorithm is given in Fig. 4.10.

In our NN, the input and output layers are fixed. For the hidden layers, we always start with two hidden layers with 32 nodes, denoted by $\{32, 32\}$ (It means there are two hidden layers, with 32 nodes in the first hidden layer and 32 nodes in the second hidden layer. If we have $\{32, 64\}$, it means there are two hidden layers, with 32 nodes in the first hidden layer and 64 nodes in the second hidden layer), and 1000 sets of parameters in the training set. We then train this neural network until the training error err_{train} approaches an approximate constant minimum value. Our strategy is as follows: if err_{train} is smaller than the designated value (e. g., 3%), the program goes to the validation part; if err_{train} is larger than the designated value, the number of hidden layers will be increased by one and the new NN is re-trained with the same training set. The number of nodes in the new hidden layer is 64. We continue this process of adding new hidden layers if the training error is larger than the designated value. The

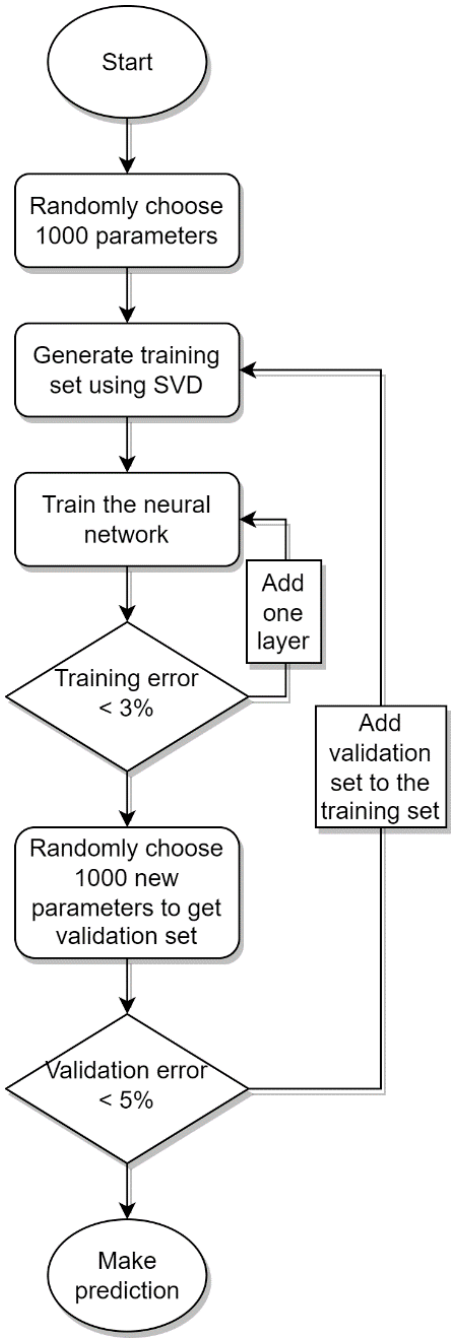

Figure 4.10: Workflow of adaptive neural network. This framework automatically increases the number of layers and training size according to training error and validation error.

number of nodes in these hidden layers are given in equation Eq. (4.31) below:

$$\underset{two\ layers}{\{32,32\}} \rightarrow \underset{three\ layers}{\{32,64,32\}} \rightarrow \underset{four\ layers}{\{32,64,64,32\}} \rightarrow \underset{five\ layers}{\{32,64,128,64,32\}} \rightarrow \dots \dots \tag{4.31}$$

We continue this procedure until the validation error is less than the designated value. The strategy is summarized by the flow chart in Fig. 4.10.

A small training error means the neural network can predict parameter vectors it has already seen before, not necessarily new vectors. So, the next step is to validate that the trained neural network can still give a small error for parameters that lie outside the training set. This step is called validation. For this part, we uniformly randomly choose 1000 sets of new parameters, Ω_V, from the parameter space Ω and determine their principal vectors using our constitutive model and SVD ($\vec{\psi}(\vec{x}_j)$) and neural networks ($\vec{\psi}_{NN}(\vec{x}_j)$) respectively. The validation error is defined in the same way as the training error, i.e.,

$$err_{validation} = \frac{1}{|\Omega_V|} \sum_{\vec{x}_j \in \Omega_V} \frac{||\vec{\psi}_{NN}(\vec{x}_j) - \vec{\psi}(\vec{x}_j)||}{||\vec{\psi}_{NN}(\vec{x}_j)||} \tag{4.32}$$

If the validation error is smaller than a pre-assigned value, we stop training and validation and go to the prediction phase; if the validation error is large, which means the NN makes bad predictions, we will add these new parameter vectors and their principal components (computed using constitutive model) to our training set and return to training.

When training and validation finally ends, the trained NN makes very good prediction of principal components for any parameter vector in the parameter space. An example is shown in Fig. 4.11 for a c-PA gel subjected to cyclic loading (strain rate is $0.01/s$ for loading and unloading, and maximum stretch is 2). After training, we randomly select 1000 parameters from Ω and then determine their principal components by calculating the c-PA model. We compare these principal components with the predicted principal components using the trained NN. From Fig. 4.11, the predicted components are practically identical to the components obtained by integrating the constitutive model.

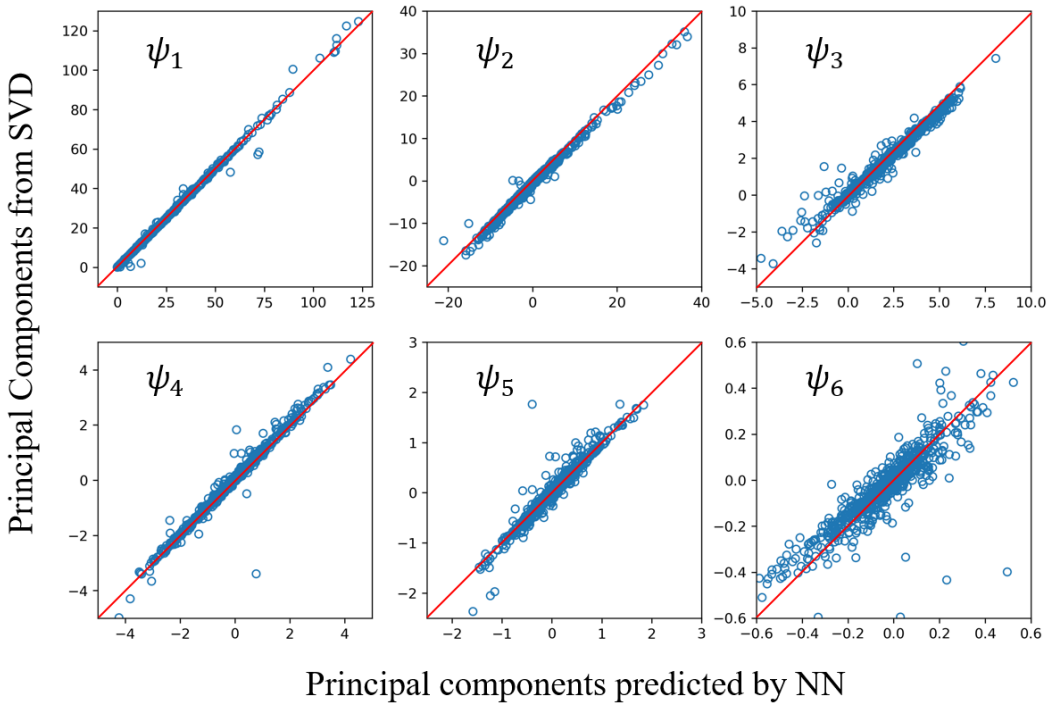

Figure 4.11: Calculated principal components using constitutive model for c-PA gel versus predicted principal components using NN for cyclic loading. The straight line with slope 1 is used to guide the eye.

Here we briefly explain the mathematical strategy of our update logic. When the training error is large, it means the neural network underfits the data due to simplicity, so we need to increase the complexity of the neural network. When the validation error is large, the neural network does not sample enough points in the parameter space to make a good prediction, so it is necessary to increase the size of the training set.

4.5.3 Results for NN fitting

For each material, we first choose 1000 sets of parameters from their parameter space, calculate the stress matrix and then get the singular values to determine

how many singular values we need to approximate an experimental curve. All the results are summarized in Fig. 4.12. For all the models and loading histories, the singular value becomes negligible after the 4^{th} term, which means $r^* = 4$ is enough in this work.

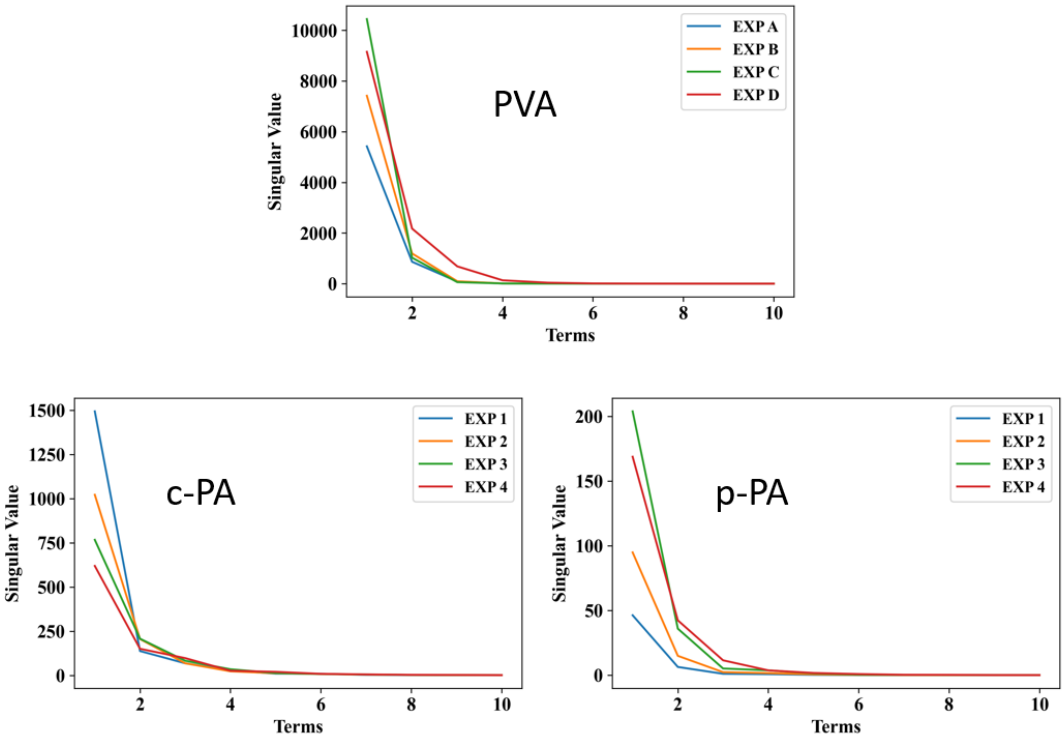

Figure 4.12: Singular values for different models and loading histories. These results show that 4 singular values are sufficient to approximate all our experiments well.

PVA model fitting

For PVA gel, the training results are shown in Table 4.2. The PVA constitutive model has 4 parameters, so it is relatively simple to fit. A neural network with two hidden layers and 1000 training size is good enough to predict the principal values extremely well. In our algorithm, $|\omega_P| = 1000|\Omega_T| = 1 \times 10^6$. This is a large number of parameters, and the last row in Table 1 shows that a brute force calculation will cost 23.4 hours in total to calculate the PVA constitutive model 2

million times for all four experiments. However, the neural network needs less than 2 seconds to predict the principal values for all parameters in Ω_P. Even if we include the training time, less than 5 minutes is needed to perfectly fit all the experimental curves. The best parameters are

$$(\mu\rho, \alpha_B, t_B.\mu\bar{\gamma}_\infty) = (4.319kPa,\ 1.648,\ 0.2206s,\ 63.85kPa) \tag{4.33}$$

The comparison between the prediction of PVA model using the parameters obtained by NN and experiments is shown in Fig. 4.13.

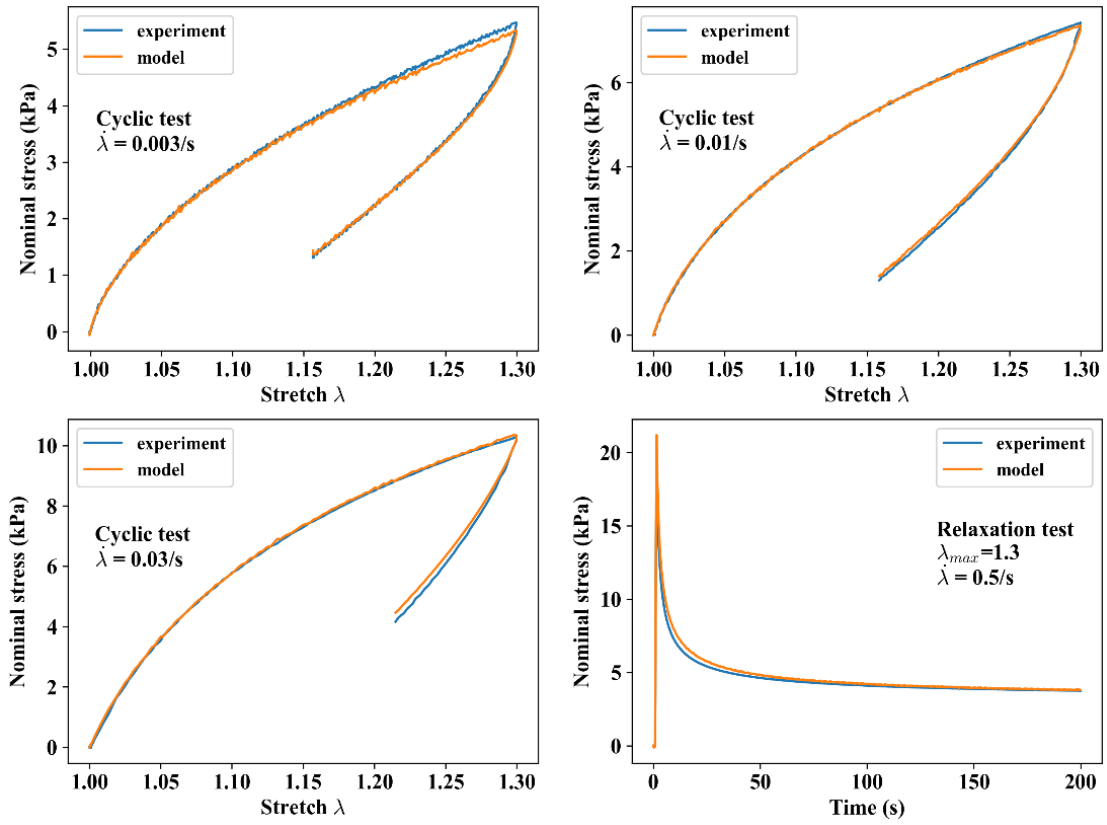

Figure 4.13: Comparison of prediction using best fitted parameters (Eq. (4.33)) from NN (orange) and experiment data (blue) for a PVA gel sample subjected to four loading histories.

Note here the parameters are different from the parameters obtained from Gaussian Process. This is because there are many sets of parameters which can fit all four experimental curves very well. This is one advantage of our machine

Table 4.2: Training results for PVA constitutive model

	EXP A	EXP B	EXP C	EXP D
Hidden layers	{32, 32}	{32, 32}	{32, 32}	{32, 32}
Training size	1000	1000	1000	1000
Training error	0.3%	0.4%	0.2%	0.3%
Validation error	3.4%	4.5%	2.8%	2.8%
Training Time	72s	72s	45s	110s
Prediction time	0.34s	0.34s	0.32s	0.34s
Compared to model	4.6h	4.6h	4.6h	9.6h

learning framework. Almost all good parameters for experimental curves can be found instead of single one. We will discuss this in detail in Section 4.6.

c-PA model fitting

For c-PA gel, the training results are shown in Table 4.3. The c-PA model is more complex than the PVA model since it has 9 parameters. The adaptive neural network captures this complexity, and a good prediction can be achieved with three hidden layers and about 3000 training size. The c-PA model is much more complex as it involves solving an integral equation for each parameter vector input. For $|\Omega_P| = 1000|\Omega_T| = 3 \times 10^6$, roughly 210 hours in total would be needed to determine the principal values for all the four loading histories without the use of neural network (last row of Table 4.3). It took less than 1 hour of training and 4 seconds of prediction time using our adaptive neural network approach.

The best parameters for c-PA model are

$$c_1 = 2.298MPa \quad c_2/c_1 = 0.2827 \quad c_3/c_1 = 0.0011 \quad \lambda_c = 1.2302$$
$$\omega_{chem} = 0.0023 \quad \alpha_B = 1.7030 \quad t_B = 0.0984s \quad m = 1.2823 \quad t_H = 0.5638s \tag{4.34}$$

The comparison between the prediction of c-PA model using the parameters obtained by NN and experiments is shown in Fig. 4.14

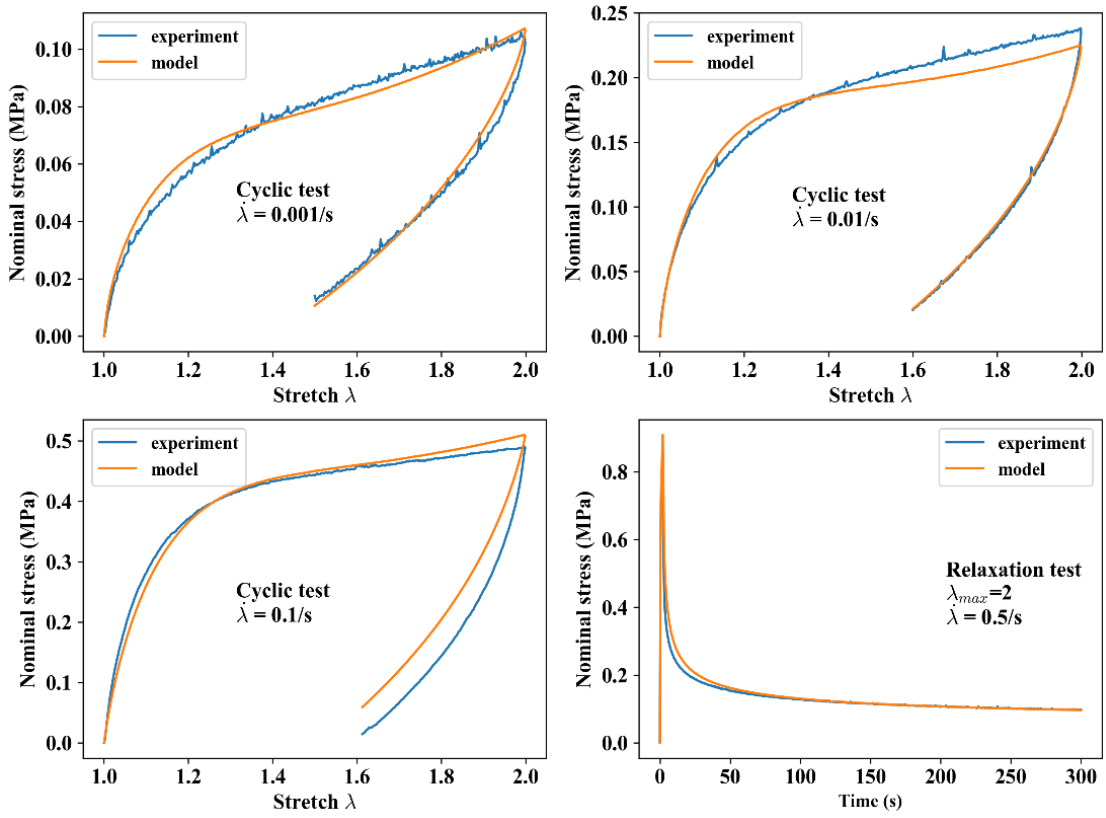

Figure 4.14: Comparison of prediction using best fitted parameters from NN (orange) and experiment data (blue) for a c-PA gel sample subjected to four loading histories.

Table 4.3: Training results for c-PA constitutive model

	EXP 1	EXP 2	EXP 3	EXP 4
Hidden layers	{32, 64, 32}	{32, 64, 32}	{32, 64, 32}	{32, 64, 32}
Training size	3000	3000	3000	3000
Training error	1.3%	1.5%	1.3%	1.2%
Validation error	4.2%	4.4%	3.2%	4.1%
Training Time	477s	487s	452s	592s
Prediction time	1.03s	0.98s	1.02s	0.99s
Compared to model	42h	42h	42h	84h

p-PA model fitting

For p-PA gel, the training results are shown in Table 4.4. The p-PA model has 13 parameters, so it is very complicated and difficult to fit. To get good prediction results, the adaptive neural network chooses five hidden layers and a training set size of 6000. The p-PA model requires solving two integral equations so it takes even more time to integrate the model than the c-PA model. For $|\Omega_P| = 1000|\Omega_T| = 6 \times 10^6$, about 600 hours in total would be needed without the help of neural network (last row of table 3), but only less than 2 hours of training and 20 seconds of prediction are needed using our adaptive neural network approach.

The best parameters for p-PA model are

$$\begin{array}{lllll} c_1 = 3.459MPa & c_2/c_1 = 0.4223 & c_3/c_1 = 0.0506 & \lambda_c = 1.1166 & \\ \omega_1 = 0.5611 & \alpha_{B1} = 1.7868 & t_{B1} = 0.0032s & m_1 = 0.3940 & t_{H1} = 0.3850s \\ \omega_2 = 0.4389 & \alpha_{B2} = 1.7268 & t_{B2} = 0.0566s & m_2 = 0.4722 & t_{H2} = 0.3542s \end{array} \tag{4.35}$$

The comparison between the prediction of p-PA model using the parameters (Eq. (4.35)) obtained by NN and experiments is shown in Fig. 4.15.

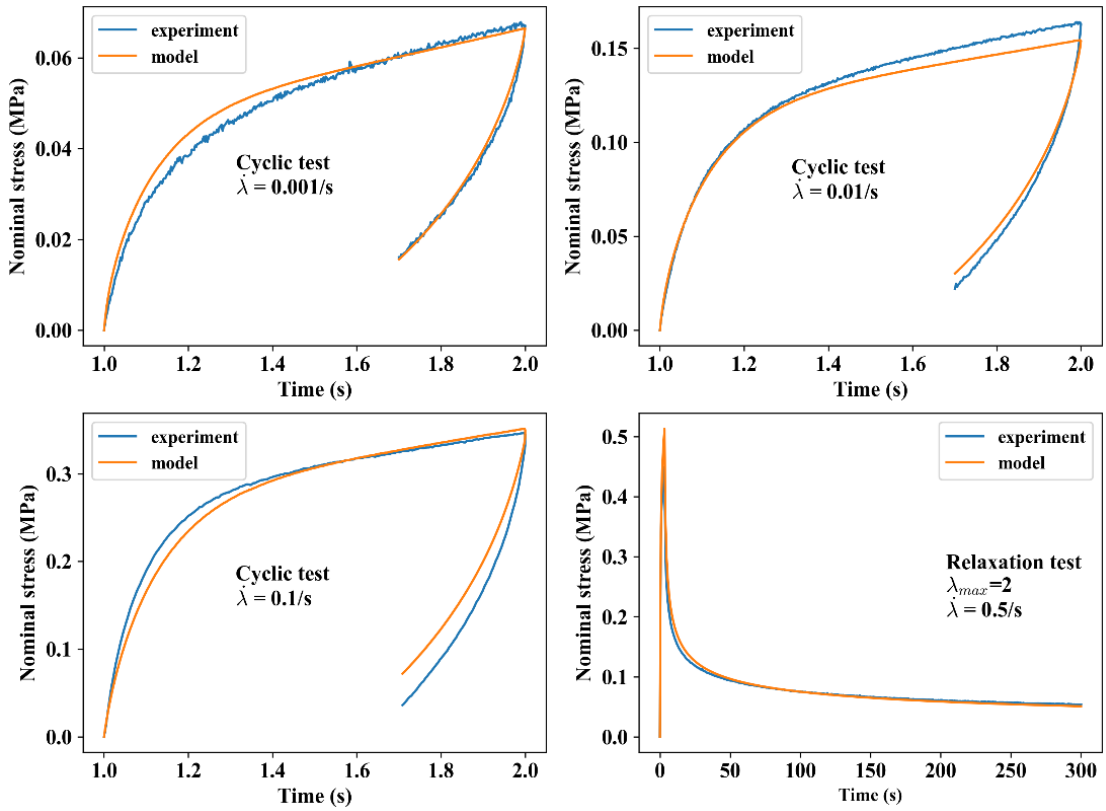

Figure 4.15: Comparison of prediction using best fitted parameters from NN (orange) and experiment data (blue) for a p-PA gel sample subjected to four loading histories.

4.6 Model analysis with machine learning method

When using this machine learning framework for model fitting, we find that there are always many sets of parameters which may fit the experimental data very well, despite considerable variations among them. For example, for PVA gel, we find that the top-ranked 500 parameters (ranked using Eq. (4.36)) vectors can fit all four experiments very well. This suggests there must be some relation between parameters. Here we make 2D projections of $\vec{x}_j^*$ onto two-dimensional subspaces of Ω and plot them in Fig. 4.16.

$$err(\vec{x}_j^*) = \frac{1}{N}\sum_{i=1}^{N}\frac{\left\|\vec{\psi}_{GP}^{(i)}(\vec{x}_j^*) - \vec{\psi}_{exp}^{(i)}\right\|}{\left\|\vec{\psi}_{exp}^{(i)}\right\|}, \quad 1 \le j \le \eta \tag{4.36}$$

Table 4.4: Training results for p-PA constitutive model

	EXP 1	EXP 2	EXP 3	EXP 4
Hidden layers	{32, 64, 128, 64, 32}	{32, 64, 128, 64, 32}	{32, 64, 64, 32}	{32, 64, 64, 32}
Training size	7000	7000	6000	5000
Training error	2.8%	2.3%	2.7%	2.4%
Validation error	3.9%	3.3%	3.8%	4.9%
Training Time	1851s	1551s	1226s	1208s
Prediction time	5.62s	3.96s	3.03s	4.12s
Compared to model	128h	128h	110h	240h

Fig. 4.16 shows that these 500 parameter vectors vary a great deal despite the fact that $err(\vec{x}_j^*)$ are less than 0.065, with most below 0.05. We let $\mathcal{X}$ denote the set of these 500 parameter vectors. The inescapable conclusion is that there are many sets of material parameters that fit these experiments. More importantly, these plots show that there are strong relationships between $\mu\rho$ and α_B, as well as t_B and $\mu\overline{\gamma}_\infty$.

To understand this dependence, we use a result from our previous work [20] which shows that when strains are small, that is, when $\lambda(t) = 1 + \epsilon(t) \sim 1$, our nonlinear viscoelastic model becomes linear, resulting in

$$\sigma(\vec{x}, t) = \int_{-\infty}^{t} Y\left(\frac{t-\tau}{t_B}\right)\frac{d\epsilon(\tau)}{d\tau}d\tau \tag{4.37}$$

where Y is the relaxation function in tension and is given by

$$Y(t) \equiv \frac{3\mu\overline{\gamma}_\infty t_B}{2-\alpha_B}\left(1 + (\alpha_B - 1)\frac{t}{t_B}\right)^{\frac{2-\alpha_B}{1-\alpha_B}} + 3\mu\rho \tag{4.38}$$

Eqs. (4.37) and (4.38) states that $\sigma(\vec{x}, t)$ depends linearly on $\mu\overline{\gamma}_\infty t_B$. If the constitutive law is correct, then $\mu\overline{\gamma}_\infty t_B$ must be a material constant C for a specific

experiment, therefore $\mu\bar{\gamma}_\infty = C/t_B$. Also, Eqs. (4.37) and (4.38) shows that $\sigma(t)$ increases with $\mu\rho$ and α_B. Therefore, to produce the same stress history, a smaller α_B must be chosen if a larger value of $\mu\rho$ is chosen. Fig. 4.16 shows that these relationships are consistent with machine learning prediction.

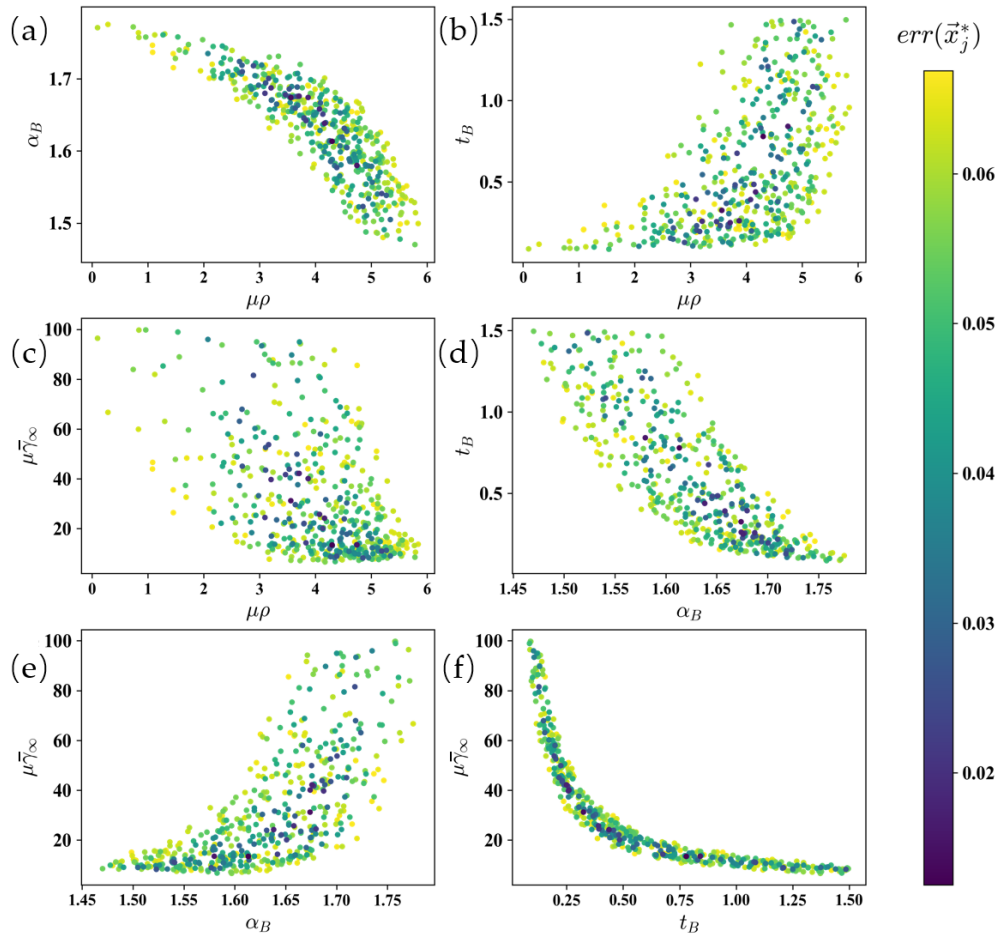

Figure 4.16: Distribution of the top 500 parameter vectors in parameter space. (a) shows that $\mu\rho$ and α_B are strongly correlated. (f) shows that t_B and $\mu\gamma_\infty$ are strongly correlated. The points are colored according to their corresponding errors defined in Eq. (4.36).

For c-PA and p-PA models, we also find that there are many good parameters that can fit all the experiments very well. Considering these two models contain more parameters (9 and 13, respectively), there is great possibility that there are some relationships between all these parameters. This part is not the focus of

this study so we haven't got the chance to dive deeper into it. However, from the analyzing results of PVA model, we have already shown that our proposed machine learning framework not only has the ability to fit model parameters, but also has great potential in model analysis and optimization.

4.7 Discussion

A machine learning framework based on singular value decomposition and machine learning training is used to build metamodels for constitutive models. Principal components of stress histories in the training set are extracted using SVD. Two different machine learning methods are trained to simulate the relationship between model parameters and principal components of stress histories. After training, the machine learning framework can predict the stress histories not in the training set very well. This allows us to generate a large number of stress histories based on different parameter sets to fit experiments precisely and quickly.

For Gaussian Process method, it makes predictions based on the kernel function with model parameters as variables, so it has a complete mathematical theory to guarantee its prediction effect. It can not only give us the prediction or fitting results, but also give us the variance of the prediction, which is very helpful information for active learning and training set update. Although we haven't implemented it efficiently on very complex models like c-PA and p-PA models, there is no theoretical obstacle to its implementation with good parallel computation setups.

For the neural network method, it is able to adapt to a wide variety of constitutive models. Our adaptive neural network method updates the size of the neural network and training size automatically. Three different time dependent constitutive models, from simple to complex, are used as examples to validate this adaptive neural network framework. Both the training results and the fitting results show that our method can automatically capture the complexity of the constitutive model and find a precise and efficient neural network. No extra operation is needed for neural network building, training, validation, and prediction to accommodate this method for different constitutive models.

With the number of parameters in the examples ranging from 4 to 13, our approach in this work shows universality and scalability, and thus can be applied to almost any parametric model. In other words, it is not necessary to restrict it to rate dependent material models. The one limitation of our method is that we need different neural networks for different loading histories since the basis is not included in the neural network. Future work may consider possible solutions like including loading conditions in the training set or using recurrent neural networks to study the time series.

Besides model parameter fitting, our approach allows exploration of the correlations between different material parameters in the constitutive model. Such information can provide useful guidance to the underlying micro-mechanics that govern the mechanical behavior of materials. This is also important for generative design of materials when the constitutive model accurately captures the physics.

CHAPTER 5

NONLINEAR VISCOELASTICITY AND LOAD TRANSFER OF PA HYDROGELS

5.1 Introduction

The area of hydrogels has undergone great advances since the development of double network (DN) gels [13, 15], which provides a path to toughen an otherwise brittle solid. However, because the networks in DN gels are chemically crosslinked, the damage to the sacrificial network due to overload cannot be recovered. This shortcoming motivated material chemists to fabricate gels with networks crosslinked by dynamic bonds [60, 61, 62]. These include dynamic covalent bond, hydrogen bond, ionic bond, metal-ligand coordination, host-guest interactions, hydrophobic interactions, and $\pi - \pi$ stacking [17, 63, 64, 65, 66, 67]. Often, dynamic bonds serve as sacrificial bonds to dissipate energy, which is a key toughening mechanism. However, unlike DN gels, physical bonds in the dynamic networks can reform, which leads to useful mechanical behavior such as self-healing and improved fatigue resistance [68, 69, 70, 71].

Tough and self-healing hydrogels usually have two distinct dynamic modes of polymer networks, one is crosslinked by the dynamic bonds, and another is crosslinked by the covalent bonds and/or entanglements. Load transfer between two networks is important to predict the failure near stress concentrators, such as the tip of a preexisting crack. For example, in a gel consisting of both permanent and dynamic networks, crack growth cannot occur until both networks fail. This failure depends on the load transfer mechanics between the permanent and the dynamic networks. In many systems, the dynamic network

consists of sacrificial bonds which break to dissipate energy and protect chains in the permanent network [72, 73]. This load transfer problem is of great importance to the development of tough gels, yet it is poorly understood. Depending on the time observation window, soft materials with dynamic networks can exhibit strong or weak viscoelastic behavior. At present, our understanding of viscoelasticity is still rather incomplete. Many analyses and physical interpretations rely on linear viscoelastic theory, which is well developed but limited to small strains. For example, the storage and loss moduli of soft materials are typically determined by rheology testing at strains on the order of 1%. In applications, strains in soft materials can easily exceed several hundred percent. More importantly, linear viscoelasticity assumes that relaxation times) are material properties, independent of stress and strain history. However, as noted by [23, 63, 74, 75], the bond breaking and healing kinetics in most dynamic networks are sensitive to the force or stretch acting on the chains. This means that relaxation times are not material properties but depend on the history of stress or strain. This nonlinear effect is expected to play a key role in the load transfer between the two networks in tough, soft materials.

In recent years, there has been a surge of interest using discrete and quasi-continuum approaches to learn the effect of bond breakage and formation on the mechanical response and viscoelastic behavior of polymer networks [76, 77, 78, 79]. In this work, we shed light on this load transfer problem and how it depends on dynamic bond (sticker) strength using polyampholyte (PA) gels with two types of stickers developed by Sun et al. [17]. We study four PA gels. Specifically, for each type of sticker, we prepare gels with or without a chemical cross-linker *N*, *N*′-methylenebisacrylamide (MBAA). We call these c-PA and p-PA gels, respectively. The dynamic bond of the 1st type

is formed by p-styrenesulphonate (NaSS) and N-dimethylaminoethylacrylate (DMAEA-Q). The softening temperature of this gel is 17.3 °C which is below room temperature. The 2nd type of dynamic bond is formed by NaSS and 3-(methacryloylamino) propyl-trimethylammonium chloride (MPTC), with softening temperature at 48.2 °C. In our experimental observation window, the storage modulus and loss modulus of the 2nd is much greater than the first, so we call the first dynamic bonds weak stickers and the second are called strong stickers. In the following, gels with strong/weak stickers will be labeled by $c - PA_{strong/weak}$ and $p - PA_{strong/weak}$, respectively.

5.2 Experimental design

As we mentioned in section 4.1, the main difference between linear and nonlinear viscoelasticity is whether the relaxation time depends on strain histories or not. Theoretically, we can perform uniaxial tension tests with different strain histories and compare their relaxation times or relaxation functions. However, nonlinear viscoelasticity is usually small in uniaxial tension tests, and it is easy to be affected by random factors, like variance between samples, testing noise, temperature, etc. To get rid of all the interference, one approach is to generate high strain gradient within a single sample. Here we propose two tests to monitor the nonlinear viscoelastic effect.

5.2.1 Single edge notched tension (SENT) test

In a linear viscoelastic solid, the relaxation function is independent of the stress/strain history, hence the speed of stress relaxation in a relaxation test is spatially uniform in the cracked specimen, despite the high stress/strain concentration near the crack tip [80]. However, for nonlinear viscoelastic solids, the relaxation function depends on the strain or stress level. If the strain field is non-uniform, the speed of stress relaxation can vary greatly in different parts of the specimen. This phenomenon is expected to be most significant near the crack tip, where the strain gradient is very large. To observe this behavior, we perform a relaxation test using the SENT specimen (Fig. 5.1). Thicknesses of specimens range from 1.9 mm to 2.1 mm. In-plane dimension is 20 mm $\times$ 10 mm with a 2 mm crack at the middle of one edge. We stretch the specimen (with initial length L_0) to a nominal stretch ratio of $\lambda = L/L_0 = 1.5$ with a fast stretch rate of 0.1/s and then hold it at the deformed length $L = 1.5L_0$ for half an hour. The strain distribution is measured using Digital Image Correlation (DIC).

5.2.2 T-shape test

The SENT test can make it much easier for us to observe nonlinear viscoelastic behaviors due to the high strain gradient near the crack tip. However, the crack geometry makes this problem very difficult to analyze. Fortunately, the key features of this phenomenon can be explained by the hypothesis that the breaking kinetics of dynamic bonds are strain dependent: the relaxation time is not a material property but is sensitive to the strain history acting on the network. If this

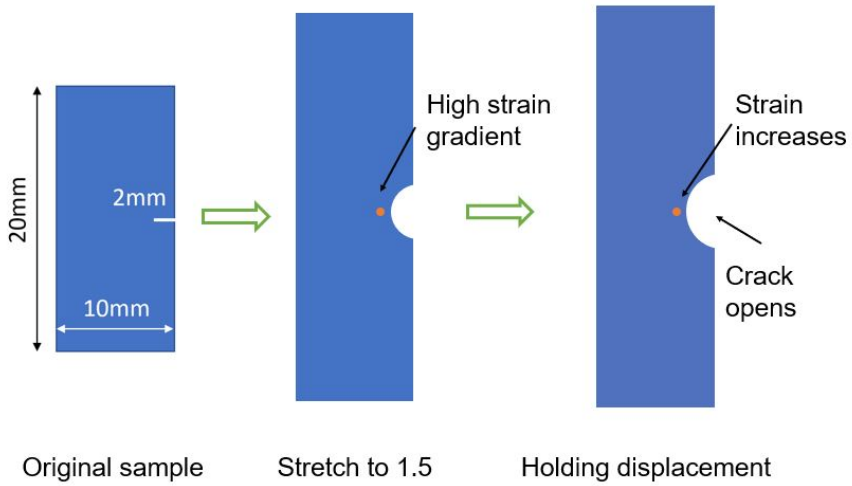

Figure 5.1: Sample of SENT test. According to our hypothesis, the crack opening displacement and strain near crack tip should increase during relaxation for nonlinear viscoelastic materials

hypothesis is correct, then we should be able to see the same phenomenon in the T-shape specimen in Fig. 5.2. The T-shape specimen has the same thickness and length as the SENT specimen, the width of the wide section (WS) is 10 mm, two times wider than the narrow section (NS). The edge of the intersection between the sections is slightly rounded to reduce stress concentration. In this specimen, each section of the specimen has approximately uniform but different strains, with the NS bearing higher strain. This means that the NS should relax faster and hence be more compliant. Since the same tension force is acting on both sections, the strain in the NS must increase. This increase in strain in the NS must be compensated by an equal decrease in strain in the WS since the total displacement is fixed during relaxation.

The common feature between the T test and the crack test is the presence of stress/strain gradient. In SENT specimen, the strain near the crack tip is higher than the strain away from the crack tip; in the T test, the strain in the NS is higher than the strain in the WS.

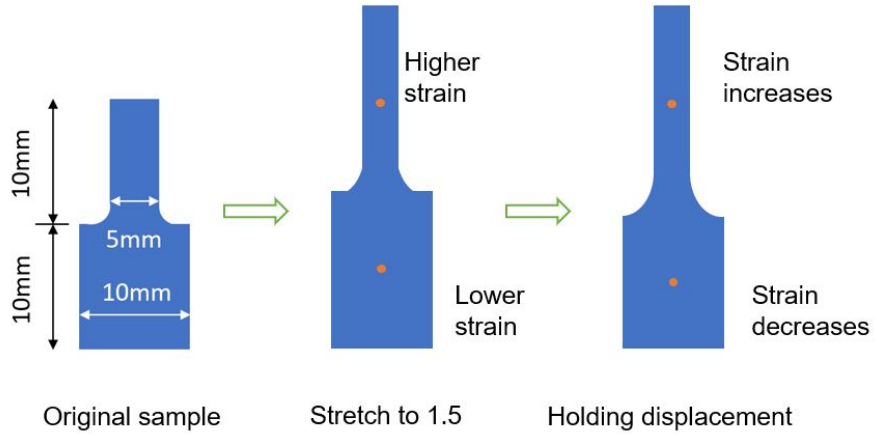

Figure 5.2: Sample of T-shape test. According to our hypothesis, the strain in the narrow region should increase during relaxation for nonlinear viscoelastic materials. The strain in the wide region should decrease because the whole displacement is fixed.

Based on this similarity, we use the T-shape test to help us understand what happens to the strain and stress fields near the crack tip during relaxation. Note that it is much easier to perform theoretical and numerical analysis for the T tests. By analyzing the stress field of T-shape specimen during relaxation, we gain insight into how the stress/strain field changes near the crack tip during relaxation and how this nonlinear viscoelastic effect would affect fracture.

With this motivation, we perform relaxation tests on the T-shaped specimen. Specifically, the specimen is stretched to a nominal stretch $\lambda_N = 1.5$ at a constant stretch rate of $0.1/s$; then held for a half hour. During this half hour, the strain history is measured using DIC. Near the boundary of the two sections, the strains are non-uniform. Our DIC measurements indicate that this non-uniformity decays rather rapidly so that the strain in each section, away from the boundary, is approximately uniform.

5.3 Experimental results for different PA gels

Here we show the experimental results of SENT and T-shape tests for all four types of PA gels. We also provide qualitative analysis of those experimental results in this section to depict the physical mechanisms of some nonlinear effects. Quantitative analysis will be given in the next section.

5.3.1 Results for p-PA gel

$p-PA_{weak}$ gel

The experimental results for the p-PA gel are shown in Fig. 5.3. In Fig. 5.3 (b), the crack opening displacement (COD) during relaxation increases with time despite the displacement being fixed at the grips. Specifically, the crack opens rapidly in the first 10 seconds and then opens slowly in the following half an hour. To quantify the change of the strain field near the crack tip, we output the evolution of stretch at point A in Fig. 5.3 (a), which is 1mm directly ahead of the crack tip. Specifically, let τ denote the time where the holding or relaxation starts. Let $\lambda_y(t)$ and $\lambda_0 \equiv \lambda_y(t = t_0)$ denote the stretch ratio in the y direction at point A for t and for $t = t_0$ respectively. Fig. 5.3 (b) also plots $\lambda_y(t)/\lambda_0$ versus time. Consistent with the crack opening profile, $\lambda_y(t)$ increases rapidly in the first 10 seconds, and then keeps increasing slowly in the span of half an hour.

As a supplement to the SENT test, we also performed the T-shape test, as shown in Fig. 5.3 (c) and (d). Similarly, the strain in the NS in the T test continued to increase with time, eventually reaching a plateau when the stress relaxes to zero, whereas the WS behaves oppositely.

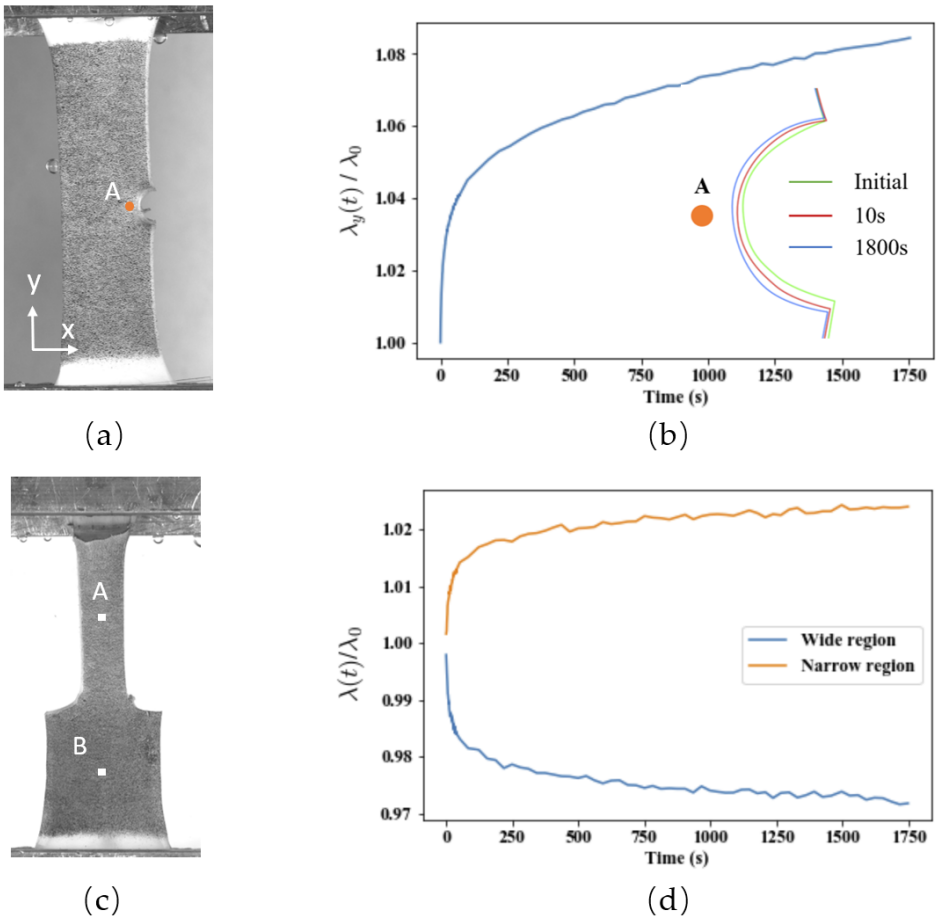

Figure 5.3: Nonlinear effect of $p - PA_{weak}$ gel. (a) SENT sample. (b) Time evolution of stretch at point A and COD (insert) in SENT specimen. λ_y is the local stretch in y direction. (c) T-shape sample. (d) Time evolution during relaxation in T-shape specimen. λ is the local stretch in y direction. λ_0 is the local stretch in y direction at measured points at $t = t_0$.

Such behavior is at odds with linear viscoelasticity, which predicts that the displacement field during relaxation should not change with time. However, this is exactly what we expect for nonlinear viscoelasticity. The common feature between the T test and the crack test is the presence of stress/strain gradient. In the SENT specimen, the strain near the crack tip is higher than the strain away from the crack tip; in the T test, the strain in the NS is higher than the strain in the WS. According to our hypothesis for nonlinear viscoelasticity, the material with higher strain should relax faster, so the stress at point A always

drops faster than the stress drop at point B. In order to keep the force balance within the sample, the strain at point A increases whereas the strain at point B decreases.

$p - PA_{strong}$ gel

We next explore the role of sticker strength by performing the same relaxation test on the gels with strong stickers.

We performed the same measurements on the SENT and T-shape specimens of $p - PA_{strong}$gel having an entangled network and a dynamic network. Strikingly, this gel shows a different behavior than single nonlinear viscoelasticity. That is, during relaxation, the COD first opens rapidly for one minute, and after that, the crack closes slowly in the following half hour. Similarly, in the T specimens, the strain in the NS first increases rapidly, reaches a maximum, then decreases slowly while the WS behaves oppositely.

Now the question is why does the $p - PA_{strong}$ gel behave in the same way as the $p - PA_{weak}$ gel in the first 10s but then behave oppositely? One possible explanation is that $p - PA_{strong}$ gel has a very long relaxation time of topological entanglements between the chains. This relaxation time, called the sticky-reptation time, is controlled by the sticker lifetime and sticker density [81]. The strong sticker results in a very long sticky-reptation time so the topological entanglements of $p - PA_{strong}$ gel behave like permanent crosslinks. This suggests that the observed nonlinear behavior is general in soft materials with dual dynamic networks, provided that one network is dynamic and the other is "permanent" in the experimental observation window. And the decrease of strain at point A is because of the load transfer between transient and "permanent" networks.

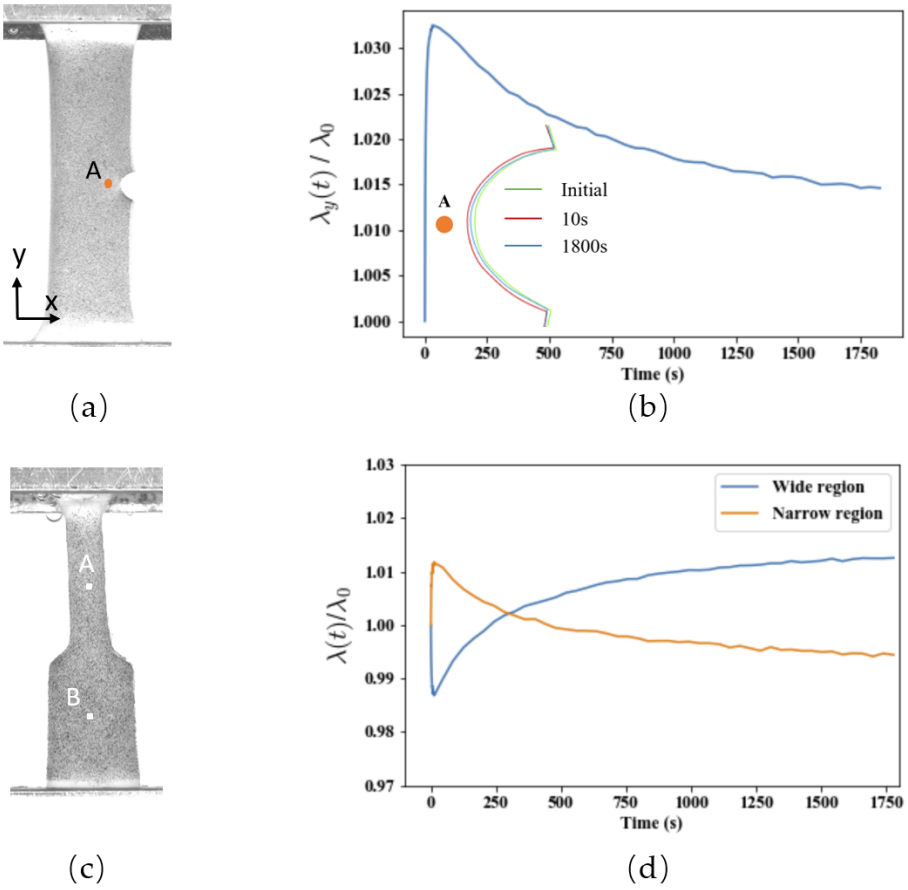

Figure 5.4: Nonlinear effect of $p - PA_{strong}$ gel. (a) SENT sample. (b) Time evolution of stretch at point A and COD (insert) in SENT specimen. λ_y is the local stretch in y direction. (c) T-shape sample. (d) Time evolution during relaxation in T-shape specimen. λ is the local stretch in y direction. λ_0 is the local stretch in y direction at measured points at $t = t_0$.

5.3.2 Experimental results for c-PA gels

From the results of $p - PA_{weak}$ gel, we see the nonlinear viscoelastic effect, just like our expectation. From the results of $p-PA_{strong}$ gel, we see another nonlinear effect, which may originate from "permanent" network caused by high topological entanglements. To validate our hypothesis, we add a chemical crosslinker into the p-PA gels and study its effect on these nonlinear effects.

Adding chemical crosslinker to hydrogels is quite a common way to increase

the mechanical properties of physical hydrogels [15, 17]. While the physical PA gels already have very good mechanical properties (higher strain, higher toughness and so on), the long time moduli of those gels are zero, which limits their application. With chemical crosslinker, a permanent network is formed by covalent bonds, which would not break or heal before the stretch limit. The presence of chemical network makes the gel more stable and more useful, but it may also make the mechanical properties of the gel more complex.

$c - PA_{weak}$ gel

First, we performed the same experiments for $c - PA_{weak}$ gel. The results are shown in Fig. 5.5. Fig. 5.5 (b) contrasts the evolution of the COD in the $c - PA_{weak}$ gel. Again, the result contradicts linear viscoelasticity. During relaxation, the crack first opens rapidly in one minute, after that, the crack closes slowly in the following half an hour, just like the $p - PA_{strong}$ gel! The stretch ratio $\lambda_y(t)$ in the y direction at point A shows the same behavior. It first increases rapidly in one minute, and then decreases slowly in the following half an hour. In T-shape sample, the behavior is also similar. The strain in the NS first increases rapidly, reaches a maximum, then decreases slowly while the WS behaves oppositely.

These results are very exciting for us, because they validate our hypothesis for the strain decrease after 10s in $p - PA_{strong}$ gel. The decrease of strain after 10s at point A is indeed because of the presence of permanent network, or almost "permanent" network caused by high topological entanglements within the observation window.

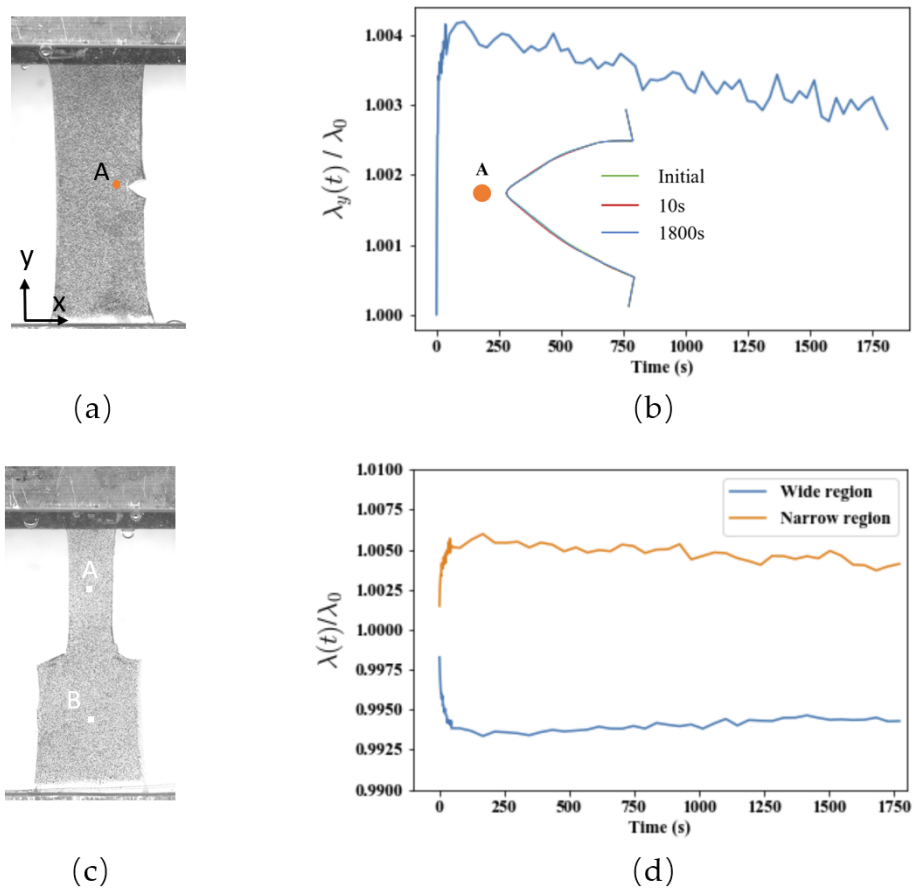

Figure 5.5: Nonlinear effect of $c{-}PA_{weak}$ gel. (a) SENT sample. (b) Time evolution of stretch at point A and COD (insert) in SENT specimen. λ_y is the local stretch in y direction. (c) T-shape sample. (d) Time evolution during relaxation in T-shape specimen. λ is the local stretch in y direction. λ_0 is the local stretch in y direction at measured points at $t = t_0$

$c - PA_{strong}$ gel

For $c - PA_{strong}$ gel, the high topological entanglements already behave like a permanent network, and adding chemical crosslinker should just increase ratio of permanent network, thus amplifying the nonlinear effect after 10s. Just like our expectations, in Fig. 5.6 (b), $c - PA_{strong}$ gel behaves very similar to $c - PA_{weak}$ and $p - PA_{strong}$ gel, but the strain decrease at point A is larger after 10s during relaxation.

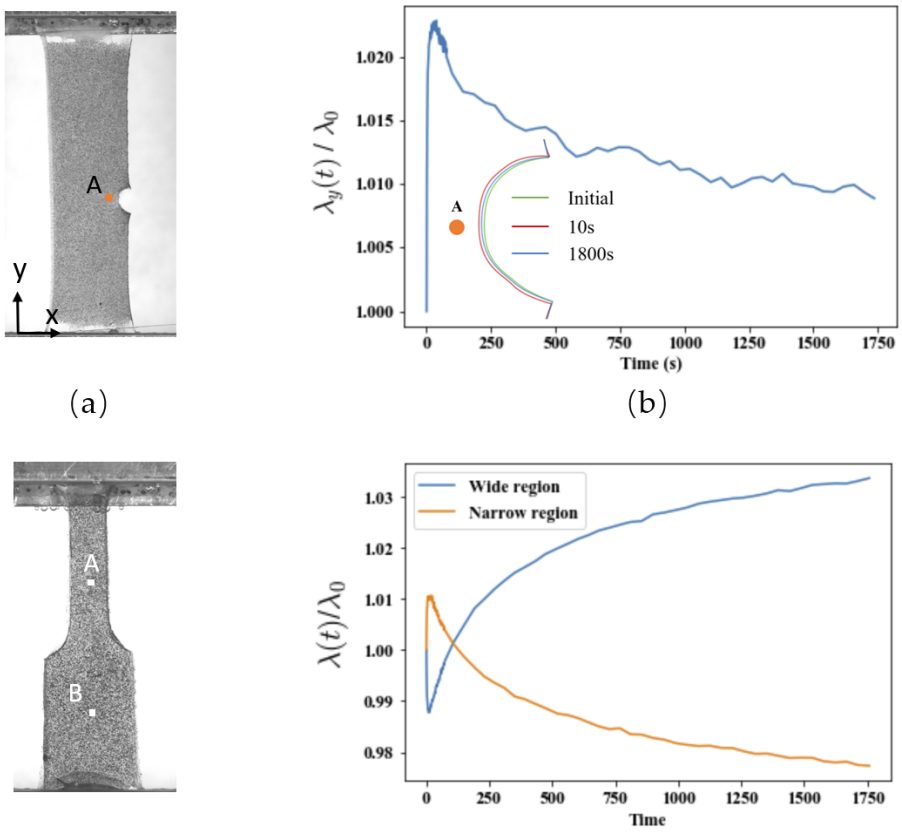

Figure 5.6: Nonlinear effect of $c - PA_{strong}$ gel. (a) SENT sample. (b) Time evolution of stretch at point A and COD (insert) in SENT specimen. λ_y is the local stretch in y direction. (c) T-shape sample. (d) Time evolution during relaxation in T-shape specimen. λ is the local stretch in y direction. λ_0 is the local stretch in y direction at measured points at $t = t_0$

5.4 Constitutive model analysis of nonlinear viscoelasticity and load transfer

In this section, a quantitative analysis of nonlinear viscoelasticity and load transfer using our PA constitutive models is performed. From our previous work [21, 22], the PA models are based on physical mechanisms of these gels, which have already been validated by elaborated experiments [17, 30]. So we are excited to see whether our model can describe these nonlinear effects and help us

reveal the underlying relationship between viscoelasticity and load transfer.

As we mentioned in 5.2.2, in the T-shape test, by taking NS and WS as two uniaxial tension parts, we are able to do theoretical analysis using our constitutive models. To simulate the relaxation process, we use Eq. (3.1) and Eq. (3.7). In our relaxation experiments, the stretch history at the grip is known, i.e.,

$$\lambda_N(t) = \begin{cases} 1 + 0.1t & 0 \le t \le 5s \\ 1.5 & t > 5s \end{cases} \tag{5.1}$$

We assume that the 1^{st} Piola or nominal stress and stretch in each section are uniform and denote them by $P_{ns},\ P_{ws},\ \lambda_{ns},\ \lambda_{ws}$ respectively. Our assumption implies that

$$\lambda_N = \frac{\lambda_{ns} + \lambda_{ws}}{2} \tag{5.2}$$

Force balance implies that

$$P_{ns}A_{ns} = P_{ws}A_{ws} = F \tag{5.3}$$

where $A_{ns},\ A_{ws}$ denote the cross-section area of the specimen in the undeformed state and F is the force acting on the specimen. Eq. (5.1) to Eq. (5.3) allow us to numerically determine the time evolution of stretch ratios $\lambda_{ns},\ \lambda_{ws}$ for the c-PA and p-PA gels. The numerical algorithm to determine the stress history is based on the fact that the force acting on the two sections is the same. In each timestep, we first guess the length of two sections with the constraint that the sum of their length is equal to the overall length which at each time step is a constant. Then we use our constitutive model to calculate the nominal stress on each section at this timestep. The force acting on each section is obtained using these nominal stresses. If the difference between the stress is less than 1Pa, we adopt these lengths and go to next timestep. If not, we re-estimate the length of two parts

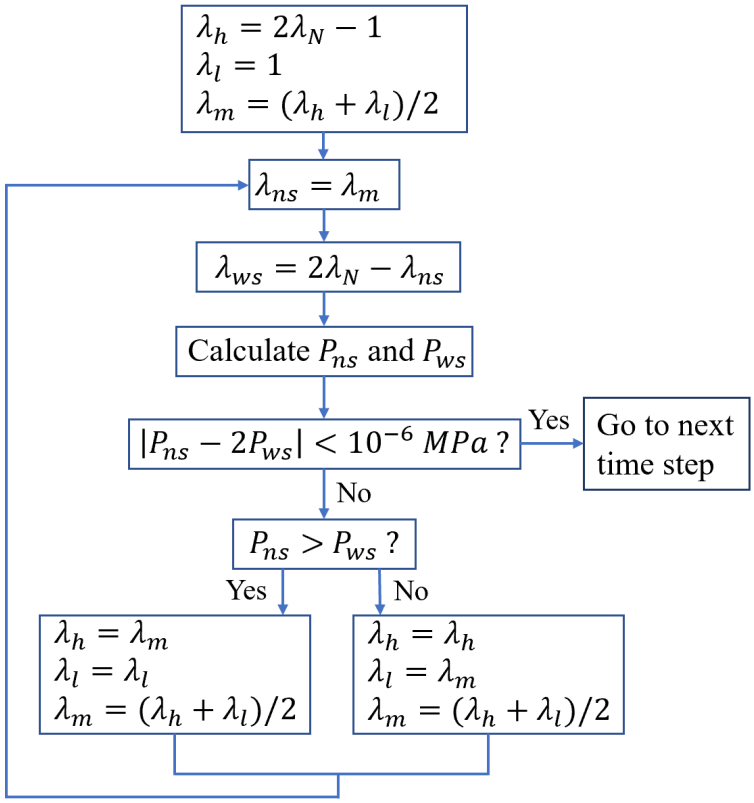

Figure 5.7: Flow chart for calculating stretches of T-shape sample in each time step. The subscripts *ns* and *ws* denote narrow and wide sections, respectively. λ_N is the nominal stretch imposed on the specimen. λ_h, λ_l, λ_m are intermediate variables in this algorithm to store relevant stretches.

according to the difference between the force of two parts. The flow chart of our numerical scheme is shown in Figure 5.7.

5.4.1 Model fitting for four types of PA gels

In chapter 4, we know that a good set of parameters is of vital importance for the prediction effects of constitutive models. So here our first step is to use our machine learning methods to find the optimal parameters for these PA gels.

Table 5.1: Model parameters for $p - PA_{weak}$ gel

$C_1 = 0.1000MPa$	$C_2/C_1 = 0.05$	$C_3/C_1 = 0.00$	$\lambda_c = 1.260$	
$w_1 = 0.5726$	$\alpha_{B1} = 1.7448$	$t_{B1} = 0.0058$	$m_1 = 0.3635$	$t_{H1} = 0.5301$
$w_2 = 0.4271$	$\alpha_{B2} = 1.8404$	$t_{B2} = 0.1529$	$m_2 = 0.5277$	$t_{H2} = 0.7351$

$p - PA_{weak}$ gel

Figure Fig. 5.8 and Table 5.1 shows the fitting results for $p - PA_{weak}$ gel. The fitting parameters are obtained using the ML framework in Chapter 4 with the adaptive neural network method.

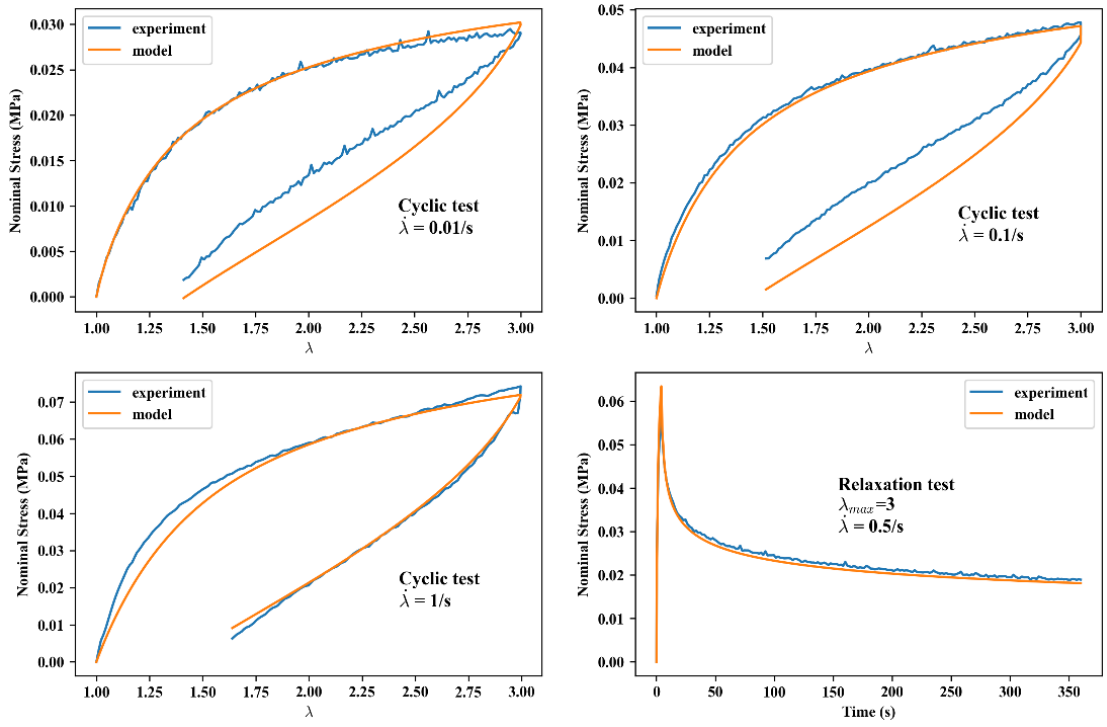

Figure 5.8: Fitting results of $p - PA_{weak}$ gel.

Table 5.2: Model parameters for $p - PA_{strong}$ gel

$C_1 = 3.990MPa$	$C_2/C_1 = 0.5060$	$C_3/C_1 = 0.0352$	$\lambda_c = 1.156$	
$w_1 = 0.7500$	$\alpha_{B1} = 1.7957$	$t_{B1} = 0.0051$	$m_1 = 0.4375$	$t_{H1} = 0.4289$
$w_2 = 0.2500$	$\alpha_{B2} = 1.6938$	$t_{B2} = 0.0183$	$m_2 = 0.4831$	$t_{H2} = 0.0940$

$p - PA_{strong}$ gel

Fig. 5.9 and Table 5.2 shows the fitting results for $p - PA_{strong}$ gel.

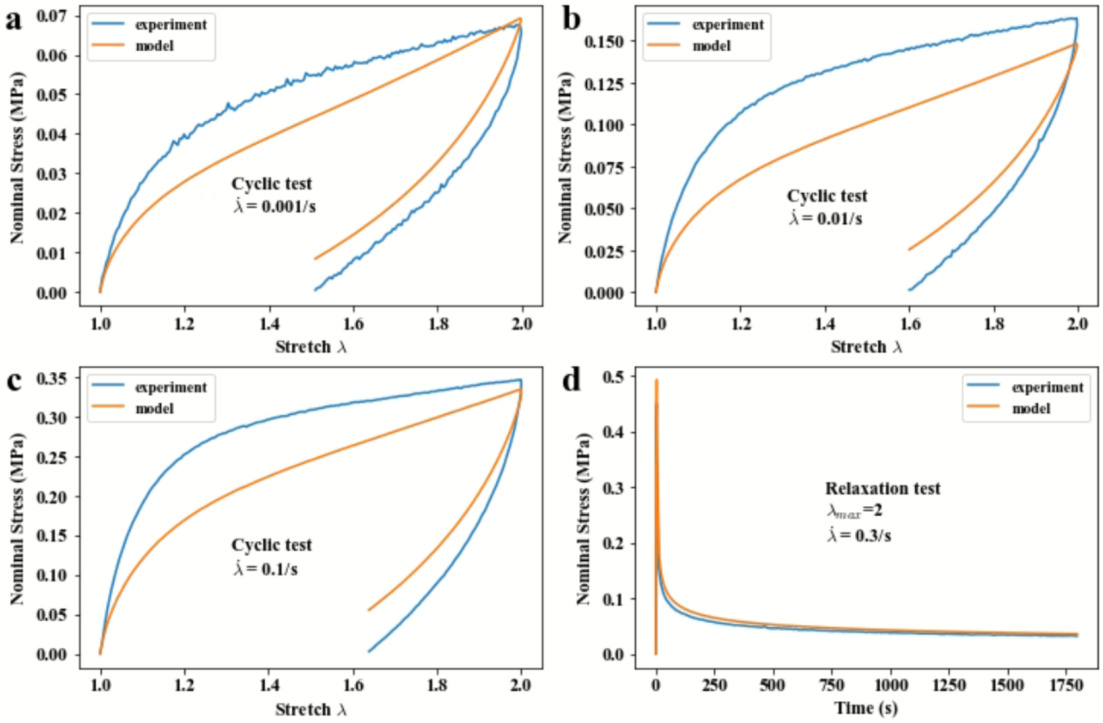

Figure 5.9: Fitting results of $p - PA_{strong}$ gel.

Table 5.3: Model parameters for $c - PA_{weak}$ gel

$C_1 = 0.05682MPa$	$C_2/C_1 = 0.0011$	$C_3/C_1 = 0.00$	$\lambda_c = 2.565$	
$w_{chem} = 0.0898$	$\alpha_B = 1.8717$	$t_B = 0.0061$	$m = 1.8017$	$t_H = 0.8021$

$c - PA_{weak}$ gel

Fig. 5.10 and Table 5.3 shows the fitting results for $p - PA_{weak}$ gel.

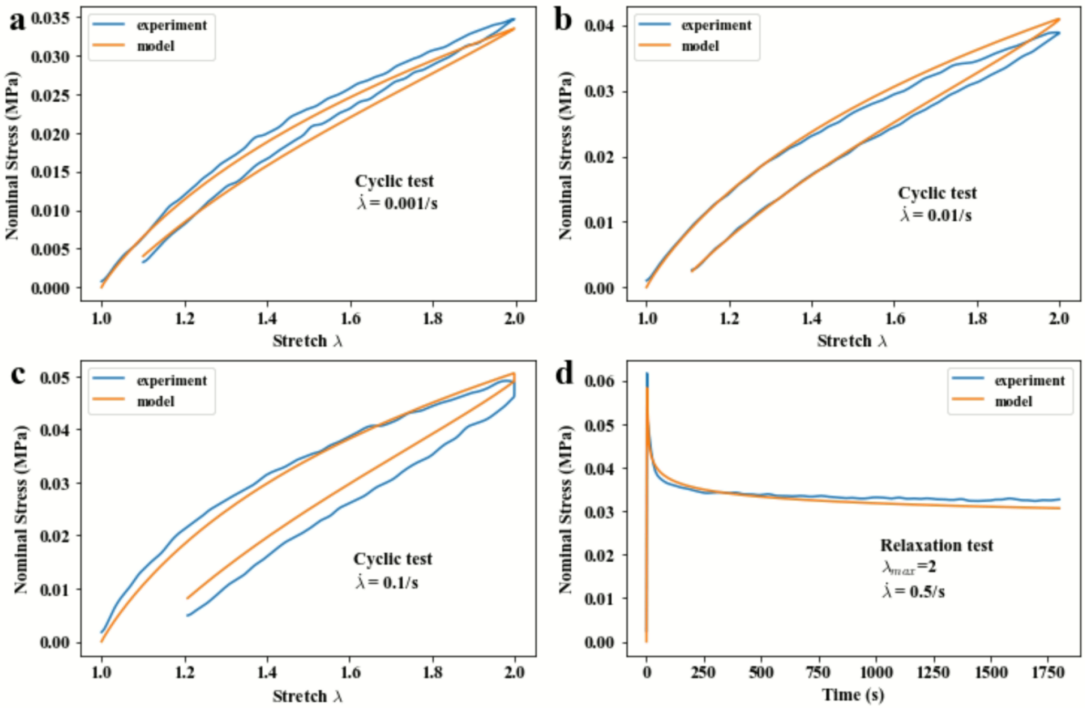

Figure 5.10: Fitting results of $c - PA_{weak}$ gel.

Table 5.4: Model parameters for $c - PA_{strong}$ gel

$C_1 = 2.3416MPa$	$C_2/C_1 = 0.1147$	$C_3/C_1 = 0.0535$	$\lambda_c = 1.055$	
$w_{chem} = 0.0026$	$\alpha_B = 1.7190$	$t_B = 0.0061$	$m = 0.3079$	$t_H = 0.3120$

$c - PA_{strong}$ gel

Fig. 5.11 and Table 5.4 shows the fitting results for $c - PA_{strong}$ gel.

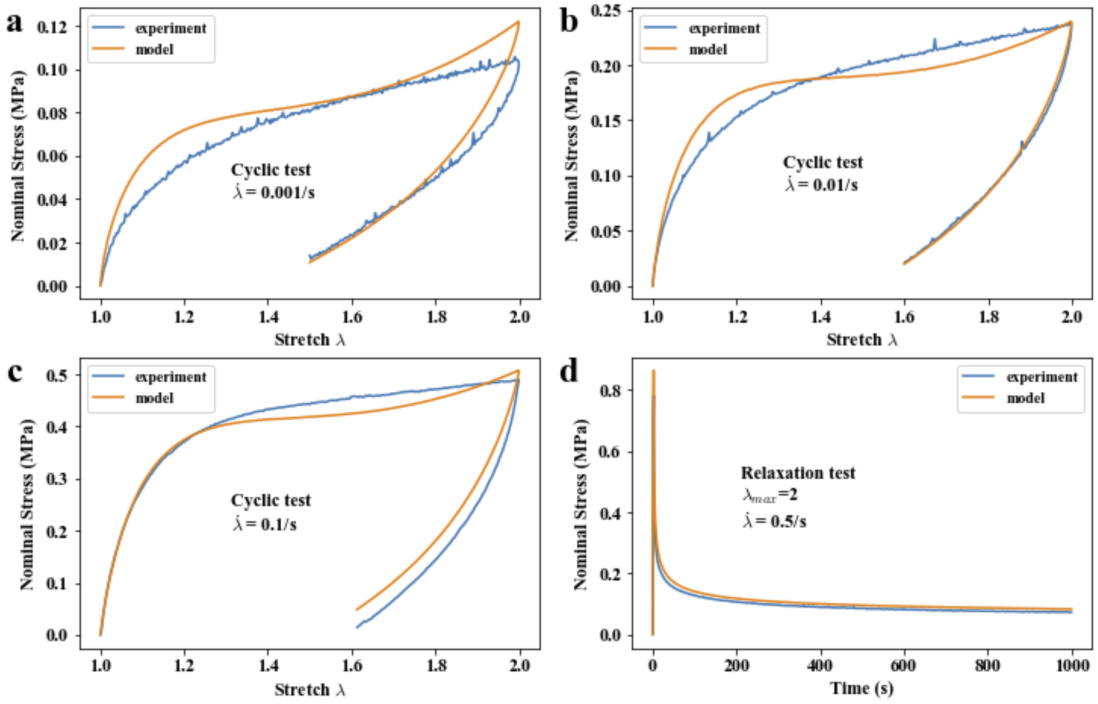

Figure 5.11: Fitting results of $c - PA_{strong}$ gel.

T-shape tests fitting results

As shown in the results of Fig. 5.12, our model can capture two nonlinear effects very well for all four types of PA gels, even though we didn't expect it when we built our model! In each case the qualitative results of the theory and experiment match. The quantitative values are all also quite close. This fact means our constitutive model captures some important physical mechanisms

of PA gels and we should go deeper into the model to find the physical cause of all those nonlinear effects.

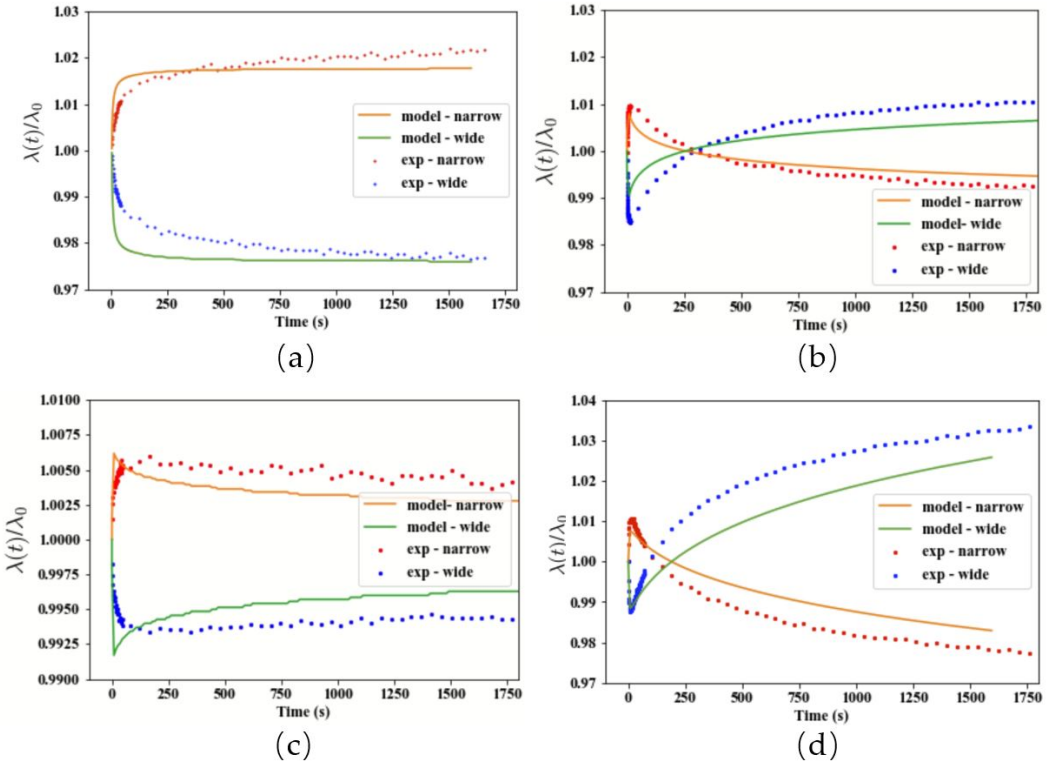

Figure 5.12: Model prediction for T-shape tests. (a) $p - PA_{weak}$ gel. (b) $p - PA_{strong}$ gel. (c) $c - PA_{weak}$ gel. and (d) $p - PA_{weak}$ gel. The model parameters used for prediction are obtained by fitting uniaxial tension tests for those gels.

5.4.2 Physical mechanisms revealed by PA models

Now we know that our constitutive models can describe the nonlinear effects of PA gels very well, which means those models indeed capture the underlying physical mechanisms of these gels. We already know that the nonlinear viscoelasticity is due to the higher chain breaking rate at higher strain. Now let's look at the reason of strain decrease at Point A from our constitutive models.

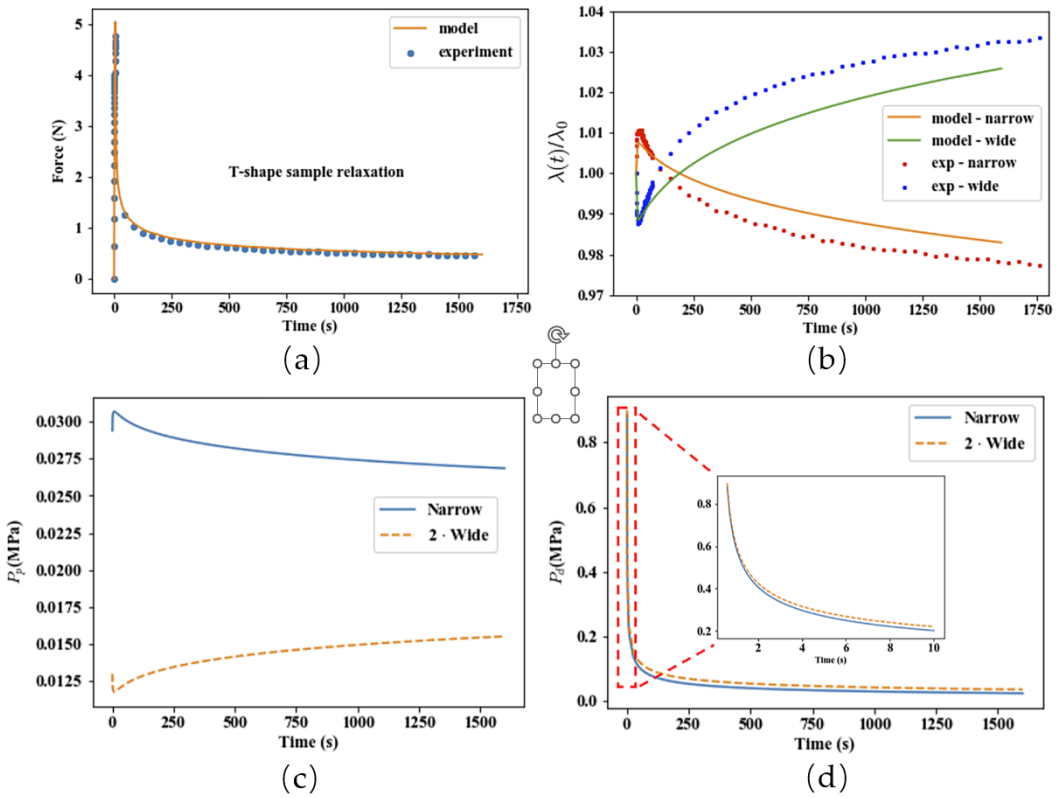

Figure 5.13: Load transfer between permanent and dynamic networks. (a) Measured force versus time curve for the T-shape specimen (b) Measured strain history (using DIC, symbols) versus simulated strain history (solid lines) during relaxation for $c-PA_s trong$ gel. Nominal stress history of the T-shape $c-PA_s trong$ gel during relaxation ($t > 5s$) for (c) permanent network, (d) dynamic network.

As shown in Fig. 5.13, let us denote the nominal stress in each section by P. In our constitutive model, we can separately calculate the nominal stress acting on the permanent network (P_p) and the dynamic network ($P_d = P - P_p$) in the $c - PA_{strong}$ gel. These stresses are plotted in Fig. 5.13 (c) and (d) for $t > T = 5s$ (when relaxation starts). Fig. 5.13 (c) shows the time evolution of the nominal stress in the permanent network in the narrow and wide section, and Fig. 5.13 (d) shows the stress evolution in the dynamic network.

These curves are consistent with the chemical structure and tension test data of $c-PA_{strong}$ gel. In this gel, the permanent crosslink density is 0.3 mol% with re-

spect to the monomer density, which is determined by the chemical crosslinker density, and the dynamic crosslink density is in the scale of 50 mol% with respect to monomer density, because one cationic and one anionic monomer can form one dynamic crosslink. As a result, in the T-shape sample test (Fig. 5.13 (a)), the stress after 1500 s is less than 10% of the stress at the beginning, which is caused by the relaxation of stress in dynamic network. In our chemical PA model, this stress distribution is captured. As shown in Fig. 5.13 (c) and (d). at the beginning of relaxation, the stress in the dynamic network is 20 times higher than the stress in the permanent network; the stress in the two networks reaches the same level after 1500 s relaxation. For different gel systems, the stress levels in the permanent and dynamic network may be different, according to their chemical components and concentration. In this work, we study only hydrogels with a high density of dynamic bonds. Note that most tough and self-healing hydrogels have a high density of dynamic bonds [15, 82, 83].

Note that, despite P decreasing with time in the relaxation test, the stress acting on the permanent network (NS) increases during the first 10 seconds, reaches a peak, then decreases to a steady value governed by the elasticity of the permanent network. The opposite is true in the wide section, as demanded by force balance. Fig. 5.13 shows that the stress in the dynamic network in the NS decays faster than the WS. At long times, the stress in both sections decays to zero, indicating that the healed physical bonds no longer carry load, as predicted by our constitutive model.

The results in Fig. 5.13 validate our hypothesis; in addition, they indicate that our constitutive model captures the relaxation behavior of this gel system. To put these results in the context of our model, we note that the relaxation function

in our theory (see Eq. (3.6)) is dependent on the strain level. Since $P_{ns} = 2P_{ws}$ in our T-shape specimens, the strain in the narrow section is higher, resulting in faster stress relaxation. However, the total force acting on each section is identical. To maintain force balance, the narrow section needs to be elongated to compensate for the faster decrease of the nominal stress, as shown in Fig. 5.13 (b). This explains the increase in strain acting on NS of the $c - PA_{strong}$ gel during the first 10 s (despite the decrease in total stress during this time).

At the beginning of relaxation, the force on the permanent network in the specimen is much smaller than the force on the dynamic network, so stress relaxation is dominated by the physical network (see Fig. 5.13 (d)). Recall that the strain in the narrow section must elongate to maintain force balance, this elongation stretches the permanent network in the narrow section and increases P_p. After the first 10 seconds, the force on the dynamic network is roughly the same as the force on the permanent network, and it relaxes much slower. This is the reason the strain in the narrow region keeps decreasing for such a long time after the first 10 seconds. In this period, the interaction between the permanent network and the dynamic network dominates the relaxation process. In our model, the force on the dynamic network will eventually vanish at sufficiently long times and the force on the permanent network is governed by hyper-elasticity.

5.5 Rheology analysis of nonlinear viscoelasticity and load transfer

The network of $c-PA_{strong}$ consists of a dynamic network crosslinked by ionic bonds and a permanent network crosslinked by chemical crosslinker and reinforced by trapped physical entanglement. Fig. 5.14 shows the dynamic spectra of this gel, which exhibits strong frequency-dependent moduli in an extremely wide frequency range from 10^{-5} to $10^{4}Hz$. This wide frequency viscoelasticity is attributed to high density of ionic bonds. For frequencies smaller than $10^{-5}Hz$, the gel shows a plateau modulus, due to the permanent confinement by the chemical crosslinkers and physical entanglements.

The $p-PA_{strong}$ gel consists of two dynamic networks crosslinked by dynamic bond and physical entanglement, respectively. This gel shows similar dynamic behavior as $c-PA_{strong}$ gel, except that the plateau modulus is from physical entanglement and in theory has no longtime modulus. However, the motion of the whole chain is significantly delayed by the stickers. We do not see the flow of this gel even for a timescale up to $10^{7}s$ (The flow time is approximately the inverse of frequency inFig. 5.14 (b)). This is due to the slowing down of Rouse modes (sticky Rouse) caused by the strong stickers [30]. Also, the distribution in the strength of ionic bonds, owing to the 100 nm-scale phase separation structure [31], could be another reason for the wide frequency viscoelasticity.

For $c-PA_{weak}$ and $p-PA_{weak}$ gels, these two gels have a weaker sticker and thus the sticky Rouse region shifts to high frequency region compared to the gels with strong stickers. We also do not see flow of $p-PA_{weak}$ gel for a timescale up to $10^{4}s$ (Fig. 5.14 (d)).

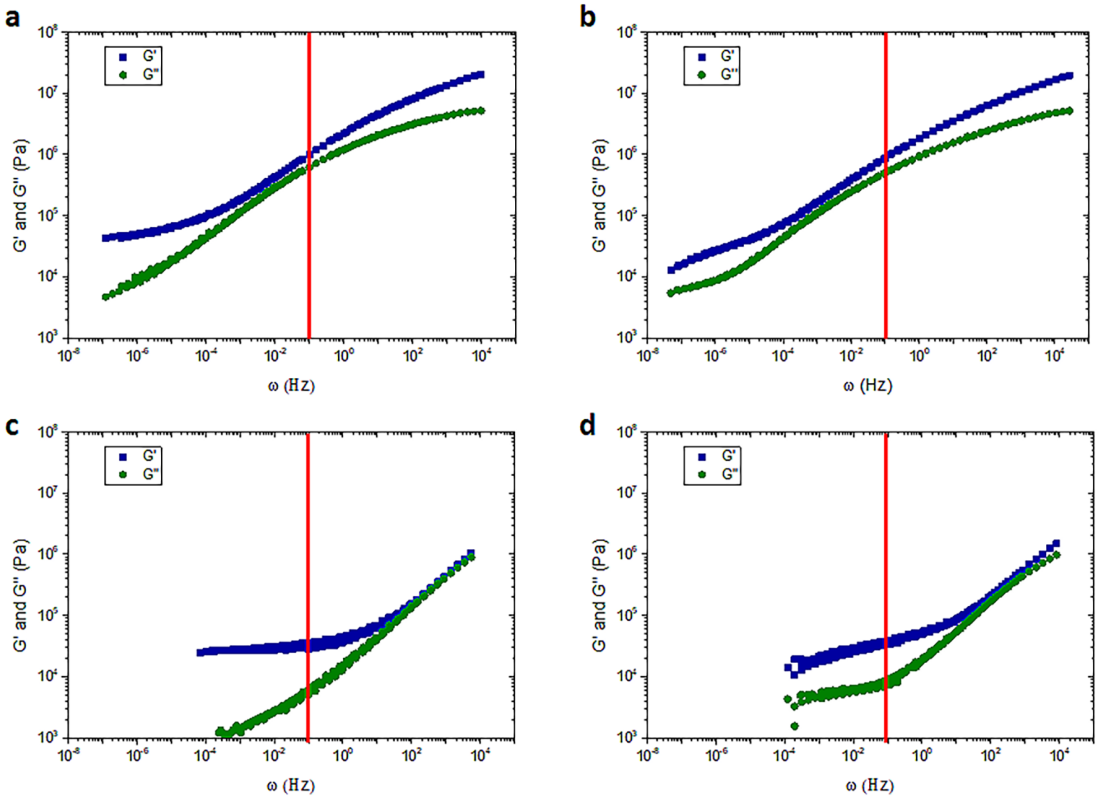

Figure 5.14: Dynamic mechanical spectra of four gels used in this work: (a) $c-PA_{strong}$, (b) $p-PA_{strong}$, (c) $c-PA_{weak}$, and (d) $p-PA_{weak}$. Reference temperature: $25°C$. $c-PA_{strong}$ and $c-PA_{weak}$ gels consist of a dynamic network crosslinked by ionic bonds and a permanent network crosslinked by chemical crosslinker and physical entanglement. $p-PA_{strong}$ and $p-PA_{weak}$ consist of two dynamic networks crosslinked by ionic bonds and physical entanglement, respectively. Red lines correspond to the strain rate of $0.1/s$ used in the following tensile tests, where $c-PA_{strong}$ and $p-PA_{strong}$ gels are strongly viscoelastic, while $c-PA_{weak}$ and $p-PA_{weak}$ gels are weakly viscoelastic, owing to the different strengths of stickers. This rheology data is provided by Kunpeng Cui and Jianping Gong at Hokkaido University.

In addition, we can see that for $c-PA_{strong}$ and $p-PA_{strong}$, both G' and G'' are bending towards asymptotic values in the limit of high strains, while for $c-PA_{weak}$ and $p-PA_{weak}$, both moduli are approximately linear in strain rate. This is because the physical PA gels with strong bonds have a long sticker lifetime. In the limit of high strain rates (or frequencies) in our rheological experiments, the dynamic bonds do not have time to break. Therefore, the moduli tend towards

a constant value at high frequencies. The PA gels with weak bonds have a short lifetime. Even in the high frequency regime in our experiments, they can still dissociate. Therefore, the moduli increase with frequency.

5.6 Discussion

We synthesized four PA gels with and without chemical crosslinks and with different sticker strengths. We carried out relaxation tests on SENT and T-shape specimens to study the effect of nonlinear viscoelasticity on the deformation fields. For $p - PA_{weak}$ gel with weak stickers, the stress near the crack tip drops faster than elsewhere due to the rapid breaking of the dynamic network; this causes the COD and strains near the crack tip to increase with time, while the strain away from the crack tip decreases with time. This further accelerates the breaking of the dynamic network near the crack tip. Since the grips are fixed, the COD for very long time will eventually reaches a steady state while the stress everywhere vanishes. We observe similar results for the T-shape $p-PA_{weak}$ specimen. This is not the case for physical gels with strong stickers. Within the time windows of our experiments, these gels behave as if they are permanently crosslinked.

For chemical gels with strong stickers, the strain, and the COD near the crack tip during relaxation first increase, reach a maximum, then decrease to a steady value. During this period of rapid relaxation, the dynamic network unloads rapidly and the additional strain is transferred to the permanent network. At some point in time, the strain in the permanent network near the crack tip reaches its maximum. If the imposed nominal stretch on the speci-

men is large enough, it is possible to fail the permanent network during this stage even while the stress is relaxing. This load transfer mechanism suggests the possibility of delayed fracture under stress relaxation. After this period, if the crack does not propagate, then the chemical network near the crack tip will stretch less (the COD will decrease) and the crack may never propagate. Eventually, the dynamic network is fully relaxed everywhere, and all the load is born by the permanent network.

Simulations are carried out using a nonlinear viscoelastic constitutive model to compute the deformation and stress in the T-shaped specimens. We found reasonable agreement between experiments and theory for all four gel specimens.

Our experiments can also be understood by appealing to rheology models for associated polymers [81]. Let us return to the longtime behavior of the $p-PA_{weak}$ gel, where the entangled network relaxes to its fluid-like state within observation time. According to Zhang et al. [81], this relaxation is governed by the sticky-reptation time $\tau_{rep} = \tau_s M^3 M_e^{-1} M_s^{-2}$,where M and M_e are the molecular mass of a whole chain and an entangled strand, respectively and M_s is the average molecular mass between stickers. This equation for τ_{rep} shows that the entanglement effect is controlled by the sticker lifetime τ_s and sticker density M/M_s. Therefore, it is reasonable to conclude that physical PA gels such as $p-PA_{weak}$ gel with weak ionic interaction will act like a fluid at long times while the $p-PA_{strong}$ gel will behave like a solid when τ_{rep} is larger than the observation time. This is supported by our results in Fig. 5.4. Likewise, the strength of stickers can also affect the behavior of chemical crosslinked gels. For example, if the stickers are weak, e.g., $c-PA_{weak}$ gel, the effect shown in Fig. 5.6 is much

weaker, as shown in Fig. 5.5. Specifically, the peak and decrease in Fig. 5.5 due to change of strains are barely perceptible since most of the stress is borne by the permanent network. Finally, we emphasize that occurrence of load transfer between the permanent/entangled and dynamic networks cannot take place without nonlinear viscoelasticity, that is, the sticker lifetime decreases with increasing strain. Specifically, the storage modulus versus frequency curve will shift to the right (higher frequency) as the strain increases. The net effect of this shift is changing the relaxation behavior within the observation window.

Finally, we address whether poroelastic flow can be partially responsible for our observations. First, we note that the behavior for both the crack and T shape samples are very similar: rapid changes of the stretch ratio occurring in roughly 10 seconds – this is much faster than the diffusion time scale. Therefore, the effect of water flow will be much more prominent in the crack sample which is not consistent with our observation. Recall that all the experiments are performed in deionized water, so water diffusion should be suppressed except perhaps at the crack tip [17, 30]. Most importantly, we have carried out some experiments with the specimen immersed in mineral oil and observed the same behavior (see A.3). The results suggested the role of water diffusion has no practical effect on the behavior.

CHAPTER 6

TIME-DEPENDENT DAMAGE OF PDMS

6.1 Introduction

In Chapter 5, we discussed the transient chain breaking and healing in PA gels, and nonlinear viscoelasticity caused by strain-dependent chain breaking kinematics. For this study, the crack in PA gels does not propagate, so we consider the permanent network as time-independent with no chain breakage during experiments. However, when the applied load is higher than some critical value, the crack has to propagate, which means breaking of both the permanent and transient network. From elastic fracture mechanics, the breaking of covalent permanent network is rate-independent and the polymer chain will break immediately when the load applied to it reaches some value. In other words, the permanent network will not fail when the external load is smaller than this critical value.

The simplest mechanical test for materials is to stretch a bar under uniaxial tension. The stress or strain when the material breaks is known as fracture strength or elongation at failure. Although fracture strength or elongation is easy to measure, it can vary greatly from specimen to specimen and is sensitive to size and loading rate [84, 85]. The fracture mechanics approach mediates the first of these difficulties by testing a pre-cracked specimen and using the critical energy release rate, G_c, at crack initiation as a criterion for failure. For time dependent elastic solids, G_c is a well-defined material property. A key advantage of the fracture mechanics approach is that while the fracture strength is geometry dependent, G_c is not [9, 86].

However, for many soft materials, G_c [26, 87, 88, 89] is not well defined (a detailed discussion of the meaning of toughness will be given here). For example, loading materials below their fracture strength or G_c [26, 28, 90] does not necessarily mean they are safe. When the external loading is below the critical criteria, instead of instantaneously breaking, catastrophic fracture due to the initiation and rapid propagation of a macroscopic crack (in samples with no pre-crack) or slow crack growth may occur after some time. This time dependent phenomenon is called delayed fracture (DF) and has been observed in ceramics [91], metals [92], plastics [93] and soft materials such as hydrogels and elastomers [27, 94, 95, 96, 97].

Although DF has been studied for different materials, we are not aware of any comprehensive study on DF, even for a single type of material. Such studies are difficult to carry out since: (1) DF, being a time dependent phenomenon, is sensitive to history of loading. For example, the behavior of a sample in a relaxation test [98] can be markedly different than the same sample in a creep or constant strain rate test [96]. (2) DF is extremely sensitive to stress concentration, and hence the geometry of the sample can significantly affect behavior. A small decrease in applied stress/strain may increase the delay time by orders of magnitude, from seconds to hours [26, 28]. Here we note that in the literature, delay fracture has been studied using different specimens with varying degree of stress concentration. For example, some studies use samples with sharp crack tips [26, 27, 90], while others used blunted cracks or notches with finite radius (usually in the scale of 0.1mm) [28, 97, 99]. In some studies, tension samples with no crack are used [94, 96]. (3) There can be many time dependent mechanisms underlying DF, e.g., poroelasticity [26, 90], viscoelasticity [96, 100] or damage due to rate dependent bond breaking [101]. More specifically, in hy-

drogels, movement of solvent can change the energy release rate near the crack tip and can lead to catastrophic fracture when the energy release rate exceeds the toughness [26, 97]. In highly viscoelastic hydrogels such as Polyampholyte gels [17], creep rupture (DF in some literature) is intimately associated with viscoelasticity, which is controlled by the breaking and healing kinetics of ionic bonds as well as the degree of chemical crosslinking [96]. Whether these mechanisms are strongly coupled depends on the material system, loading history and geometry. Due to these difficulties, there are considerable variations in observation: in some work, slow crack growth is observed before catastrophic failure [27, 97, 100], while in others only catastrophic failure is observed [26, 28, 90, 94].

The choice of experiments in this work is directed by these considerations. To study the effect of loading histories on DF, we used both relaxation and constant strain rate tests. The relaxation test is particularly relevant since in contrast to the constant strain rate test, there is no energy input to the specimen. To address the effect of specimen geometry on DF, we use two geometries: a pure shear (PS) and a double-edge crack (DEC) sample. From these two geometries, we can generate different specimens by varying the crack length and the sharpness of the crack tip. Finally, since our main interest is DF in soft materials, we choose polydimethlsiloxane (PDMS), a widely used silicon-based polymer as our model system. When cross-linked at a ratio of 10 to 1, PDMS is an elastomer, with a small amount of viscoelasticity and is used in many applications, such as substrates in microfluidic and microelectromechanical devices.

We mention two closely related studies on the delay fracture behavior of PDMS. The first used a laser speckle strain imaging technique to study the delayed fracture of a single edge notch sample [28]. The second, more recent,

combines multi-speckle diffusing wave spectroscopy technique, mechanophore mapping of chain scission and digital image correlation (DIC) to probe the mechanism of delayed fracture of single edge crack sample [89]. Both works presented strong evidence that the microscopic origin of delay fracture is localized molecular damage due to chain scission. In addition, both experiments showed that a fracture precursor in the form of a region of enhanced dynamics localized near the notch or crack tip. As noted by [89], this region of enhanced dynamics can be very large, on the order of $0.01mm^2$. An interesting result is that both studies observed very rapid crack growth once fracture initiates.

The primary focus of this work is to experimentally study the interaction between localized damage and the elastic field, by controlling the elastic fields using two different crack samples with different crack geometries (short or long crack, crack with blunt tips to reduce stress concentration) as well as loading histories (relaxation and constant stretch rate test). This coupling of elastic fields and local damage reveals a wide range of delay fracture behavior. For example, delay fracture can occur in the form of slow and stable crack growth (the slowest crack growth rate is on the order of $1nm/s$) over a wide range of energy release rates, from $35J/m^2$ to $190J/m^2$. On the other hand, a simple change of crack or sample geometry can lead to rapid catastrophic failure once fracture initiates.

The plan of this chapter is as follows. The experimental setup for delay fracture testing and material synthesis is given in section 6.2. Section 6.3 presents experimental results for blunted and sharp crack samples. Here we introduce the concept of small scale damage and G (energy release rate) controlled crack growth and demonstrate experimentally that there is a universal relation between crack growth rate v and energy release rate G. In section 6.4 we present

an analytic model based on chain breaking kinetics to determine the relation between v and G and compare the prediction of this model with experiments. Section 6.5 is summary and discussion. The concept of toughness is revisited in the discussion.

6.2 Samples and experimental design

Our experiments use two types of crack specimens (pure shear (PS) (Fig. 6.1 (a)) and double edge crack (DEC) (Fig. 6.1 (b))) with different crack geometries. The thickness of all specimens is 0.55mm where plane stress condition prevails. The crack tip in PS specimens are sharp whereas those in DEC specimens are blunted with a finite crack tip radius of $0.25mm$ (the circular hole is drilled by a CNC router with $0.25mm$ cutter, the spinning rate is 10000 rpm). Our choice of specimens is based on the observation that sharp cracks tend to initiate and grow slowly under quasi-static conditions. PS specimens allow us to study steady state crack growth in a relaxation test where the displacement is fixed on the PS sample (see Fig. 6.1 (a)). For blunt crack samples, the DEC specimen in Fig. 6.1 (b), with two symmetric blunted cracks is chosen to lower the strain concentration at the corners of sample, more details about this sample are shown in S4. A bonus of using this sample is that, with two cracks, we get two data points in a single test.

For sharp crack samples, the crack is cut using a razor blade, with the cutting edge towards the crack tip. To ensure sharpness, we first stretch the PS sample slowly ($10^{-4}/s$) until the crack propagates a very small amount, and then unload the sample to zero stretch. After this cycle the crack is very sharp because a

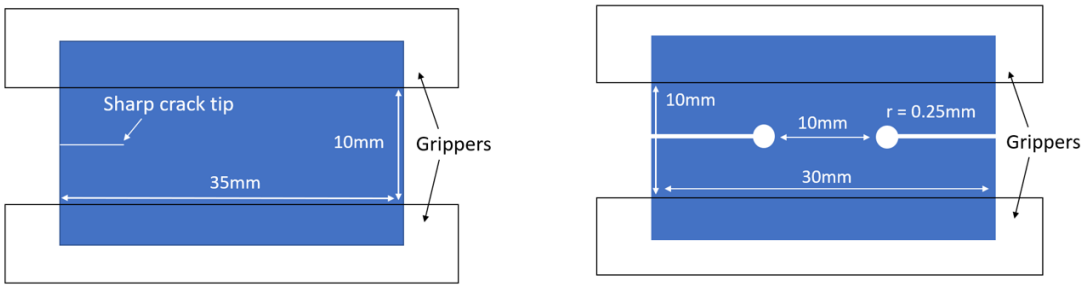

(a) (b)

Figure 6.1: Samples for delayed fracture. (a) Pure shear (PS) sample with sharp crack tip. (b) Double edge crack (DEC) sample with blunt crack tip.

new crack tip was generated during crack propagation. In Fig. 6.1, the crack length is not specified, because samples with different initial crack lengths will be used in this study. We will specify the length of the crack when we discuss our experimental results.

Fracture testing, Relaxation test: For DF tests, we stretched the samples with a stretch rate of 0.1/s until they reached the designated displacement. Then the displacements were fixed at the grips, during which the force was recorded using a load cell (Interface, SMT1-100N) and images were acquired using a camera (FLIR Grasshopper3 4.1 MP Mono).

DIC implementation: DIC was used to monitor the change of strain field for tension and relaxation tests. Details of the DIC measurements are given in Chapter 2.4-2.5.

6.3 Experimental results

6.3.1 Delayed fracture for blunt crack DEC sample

To determine the stretch levels to use in the DF experiments, we first stretched the sample with stretch rate $0.0001/s$ until it broke. The fracture stretch for this sample was between 1.65 to 1.7. Based on this value, in the relaxation experiments, we stretched the sample with a stretch rate of $0.1/s$ to a stretch of 1.6 and then held the displacement. During the holding period, images were acquired for DIC analysis. An example is shown in Fig. 6.2.

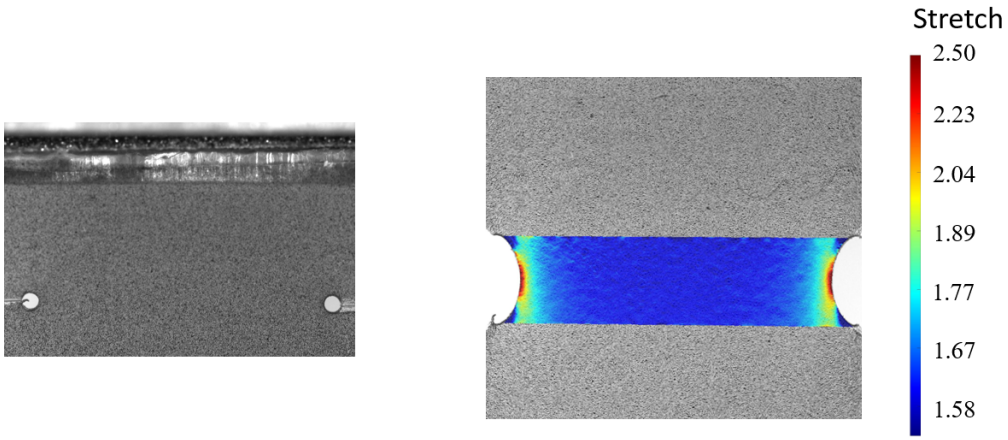

Figure 6.2: A blunt crack in a DEC specimen, only a small part of crack is shown due to limited field of view of camera. (a) Sample before stretch, (b) sample after stretch to a stretch ratio of 1.6.

We observe two interesting phenomena. The first is shown in Fig. 6.3 (a) where the change of stretch ratio at a fixed point ($100\mu m$ ahead of the crack tip, measured over a $20\mu m \times 20\mu m$ square) is plotted against time. During relaxation, the crack gradually opens and the normal stretch near the crack tip increases with time as well.

Fig. 6.3 (a) shows that the stretch ratio increases very rapidly in the first few minutes, then increases very slowly over a period of 7 hours. This result is unexpected for PDMS. In our previous work, we saw similar results in a PA gel, and we concluded that this phenomenon was caused by nonlinear viscoelasticity, where relaxation time increases with strain [25]. However, the viscoelasticity of our PDMS should be small (see A.5.1), and one would expect the relaxation time to be independent of strain. From our rheology test in SI and the rheology data from Placet et. al.[102], the loss modulus of PDMS does not reach its peak even when the frequency is 10^5 Hz, which means that the characteristic relaxation time of PDMS is smaller than $10^{-5}s$; therefore, the duration of the viscoelastic change in strain should also be very small, roughly on the order of milliseconds; after this period, the strain should not change with time. This is clearly not the case in Fig. 6.3 (a) where the strain keeps increasing for hours.

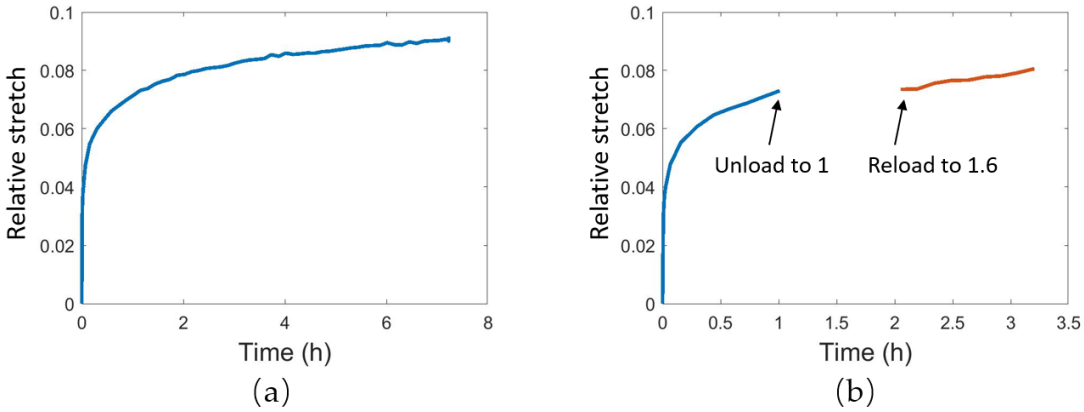

Figure 6.3: Time history of stretch near the blunt crack tip (a) Stretch increases near the blunt crack tip during hold. (b) Permanent stretch near the blunt crack tip upon unloading, resting for one hour, then reloading. In both plots, $t = 0$ corresponds to the start of holding which in our experiments is $6s$, after the start of stretching.

To further rule out the influence of viscoelasticity, we modify the loading history in our experiment. One important feature of viscoelasticity is that strain is recoverable. If the increase in strain is due to viscoelasticity, then the entire

sample should recover to its original unstrained state if we unload the sample to zero strain and let it relax for a time much longer than its characteristic relaxation time. This means that if we repeat the relaxation test after sufficient recovery time, the increase of strain should follow the same curve in Fig. 6.3 (a). However, this is not what we observed in this experiment. After unloading and 1 hour of relaxation, we stretched the sample to 1.6 again and monitored its strain change during holding. We found that the strain at the beginning of this second holding is not the same as the initial strain of the first holding. Instead, it is almost the same as the strain at the end of the first holding - there is no recovery (Fig. 6.3 (b)). This means that the strain increase near the crack tip is cumulative and not recoverable, thus cannot be due to viscoelasticity. Our hypothesis is that this increase in strain during relaxation is due to non-recoverable damage due to breaking of polymer chains near the crack tip. This hypothesis is consistent with the observation of Kooij et al. [28] and Jianzhu et al. [89]. In the discussion, we will provide insight on how damage couples with the elastic field to yield the result in Fig. 6.3 (a).

The second interesting phenomenon is that the sample eventually breaks after a period of holding (about 7 hours). Unstable crack growth occurs in less than the $0.1s$ image acquisition period, thus we are unable to determine the crack growth history. However, before the sample broke, we managed to capture some interesting photos. Fig. 6.4 shows a picture of this sample $1.8s - 0.05s$ before rapid fracture. We observe a small sharp wedge on the surface of the original blunt crack tip which grows during relaxation. When the length of this small wedge (or small crack) grows to about $100\mu m$, its rate of growth increases rapidly and a crack initiates and cuts across the sample in less than $0.1s$. This observation is consistent with the observation of Kojji et al. [28]. These authors

used laser speckle imaging to show the existence of an intense damage wedge region directly ahead of a blunt crack tip in PDMS seconds before catastrophic failure. At the end of section 6.4.3, we will provide a physical explanation for this observation.

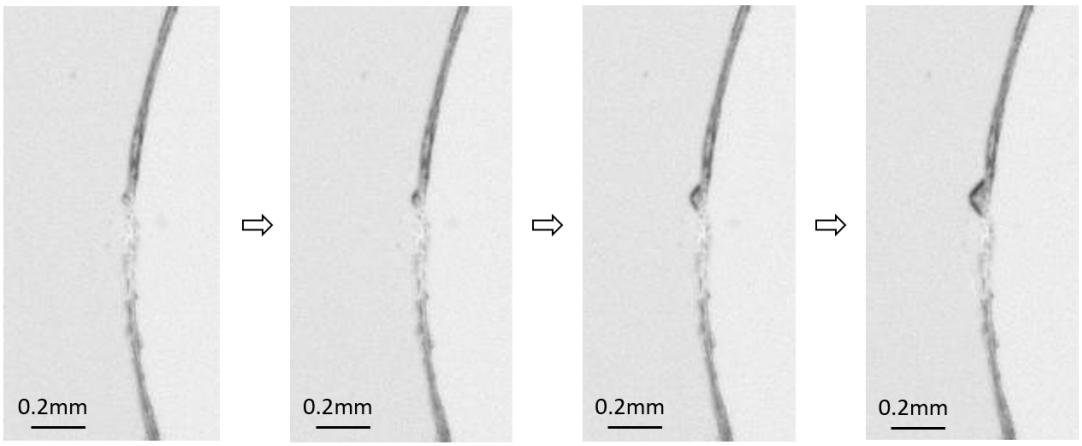

Figure 6.4: Small sharp crack nucleation before static delayed fracture. Time shown are time before the start of unstable crack growth. (To see the small crack clearly, there is no speckle pattern in this test)

6.3.2 Delayed fracture in sharp crack PS samples

The situation is very different for sharp crack tips. We first performed relaxation tests for a PS sample with a $10mm$ long sharp initial crack. We stretched the sample to $\lambda = 1.12$ and then held the displacement. During holding, the load relaxes, nevertheless, the crack initiates and then propagates with a constant speed at the beginning of relaxation (see Fig. 6.5). To study the dependence of crack growth rate, v, on the applied stretch ratio λ, additional relaxation tests are performed with the same specimen geometry but with different holding stretches. Fig. 6.5 shows that the crack growth rate, v, is nearly constant, for all

tests, the higher the applied stretch ratio λ, the faster the v. Typical crack speed in Fig. 6.5 ranges from $v = 1nm/s$ ($\lambda = 1.08$) to $v = 0.1mm/s$ ($\lambda = 1.16$).

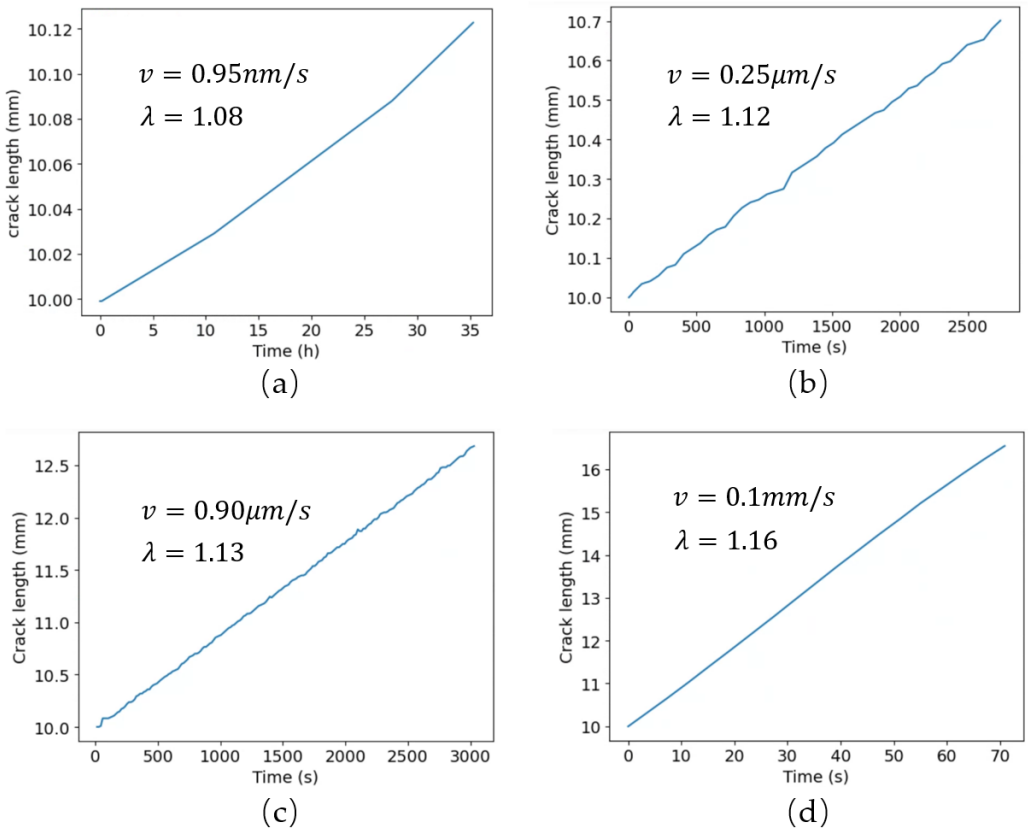

Figure 6.5: Crack length versus time in identical PS crack specimens subjected to different stretches. Zero time in these figures corresponds to the initiation of relaxation. (a) 1.08, (b) 1.12, (b) 1.13, (c) 1.16

6.3.3 Constant strain rate test

The relationship between v and λ can be an extremely useful tool to characterize DF of sharp cracks in PS samples. For such a relationship to be useful, it should be applicable to quasi-static crack growth (not only steady state) under different loading histories. To test our theory, we perform a test for the same PS crack sample with a constant stretch rate of $10^{-4}/s$ until failure. During this

test, we recorded the crack length from the acquired images and then calculated the crack growth rate by taking the derivative of the crack length versus time curve. Fig. 6.6 plots v against λ using this procedure. Also, the data for the four relaxation tests are plotted in Fig. 6.6 for comparison. The important result is that all data fall closely on the curve based on constant stretch rate test (In addition, we found that this curve is independent of the stretch rate in our tests). This shows that there is a universal relation governing crack growth rate and applied stretch in a pure shear test, irrespective of the manner of loading, as long as the crack is growing in a quasi-static manner.

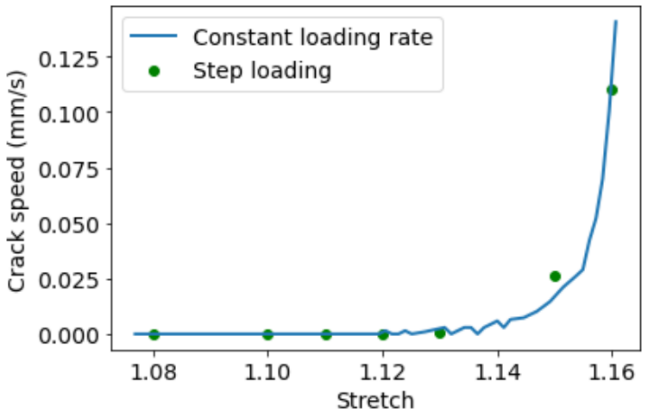

Figure 6.6: Steady crack propagation speed under difference stretch ratio λ

Our next step is to develop a model for crack propagation which is independent of specimen geometry. In this model, the applied stretch ratio λ in the PS tests is replaced by the energy release rate.

6.3.4 Fracture mechanics: G controlled crack growth

We propose a model which relates the crack growth rate to energy release rate of a specimen with a sharp crack. The key assumption is small scale damage

(SSD): that is, the region of damage is confined near the crack tip and is small in comparison with specimen geometry, specifically, c and H, where c is the crack length and H is the height of the strip. In a purely hyper-elastic solid, the true stress tensor near the crack tip is dominated by σ_{22} [103], the nominal stress in the loading direction, i.e.,

$$\sigma_{22} \sim \frac{\alpha J}{r} \tag{6.1}$$

where J is the path independent J integral [104], r is the radial coordinate of a material point in the undeformed configuration, and α is a numerical factor that depends on the angular coordinate and strain hardening characteristics. J is equal to energy release rate G in elastic solids. SSD implies that J is the unique parameter that controls damage. This means that, for SSD, there is a unique relationship between the crack speed to the applied energy release rate G. For an ideal PS specimen, the strip is infinitely long, and $c >> H$ (semi-infinite crack), G is given by [105]

$$G_{PS} = W(\lambda)H \tag{6.2}$$

where W is the strain energy density function for material points at large distances ahead of the crack tip. As shown below, in real PS samples, as long as the crack length is longer than H, the energy release rate is approximately independent of crack length and is given by Eq. (6.2). To determine W, we perform a uniaxial tension test of our PDMS using a dog-bone sample. The sample was stretched at a rate of 0.1/s until failure (See A.5.2). We observe considerable strain hardening for strain over 30% and found that the tension behavior can be well fitted by a 3-term Yeoh's hyper-elastic model (see A.5.2). In this model, the strain energy density function in Eq. (6.2) is:

$$W(\lambda) = \sum_{k=1}^{3} c_k (I_1 - 3)^k, \quad I_1 = \lambda^2 + \lambda^{-2} + 1 \tag{6.3}$$

The constants c_k in Eq. (6.3) have units of stress and is $c_1 = 0.2216MPa$, $c_2 = 4.4873 \times 10^{-2}MPa$ and $c_3 = 6.9596 \times 10^{-3}MPa$. The constant c_0 is one-half of the small strain shear modulus of the solid whereas c_2 and c_3 control strain hardening. Note that since the c_3 term is proportional to λ^6, the strain energy density can be strongly affected by strain hardening. The special case where $c_2 = c_3 = 0$ corresponds to a neo-Hookean solid.

6.3.5 FEM results for G in a PS specimen with different crack lengths

(The FEM simulations are done by Bangguo Zhu at Cornell University.)

Eq. (6.2) is an exact result for an ideal PS specimen. Of course, specimens that are infinitely long with a semi-infinite crack cannot be made. Therefore, it is important to determine the true energy release rate in a real specimen. More importantly, to validate our model (see below), we need the relation of v versus G using different crack lengths, some of these are small in comparison with H. Specifically, to avoid making more specimens, we use the same specimen geometry except we use cracks of different lengths c. Fig. 6.7 plots the normalized energy release rate $\overline{G} \equiv G/G_{PS}$ versus the normalized initial crack length $\overline{c} \equiv c/H$. The result in Fig. 6.7 is obtained using a finite element method (FEM) (see A.6.1 for details).

Recall that the length of our PS specimen is $35mm$ and the height H is $10mm$. When the crack length c is between $10 - 20mm$, the energy release rate G is independent of crack length and is give by Eq. (6.2) and Eq. (6.3). However, when

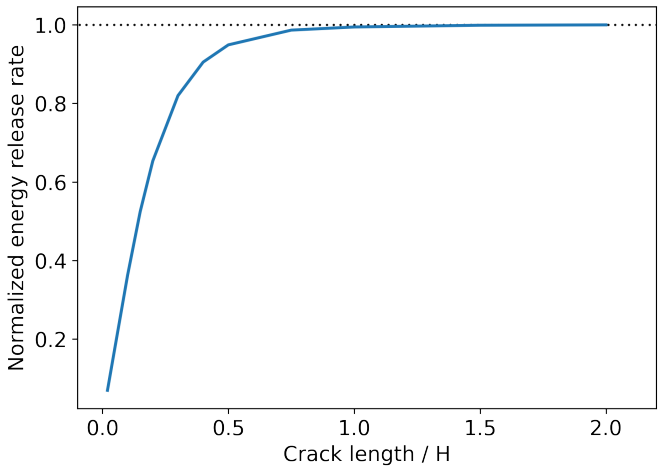

Figure 6.7: Energy release rate versus crack lengths for a stretch ratio 1.12 in a PS sample

c is less than $10mm$, G decreases with decreasing crack length even though the sample is still under stretch 1.12. Fig. 6.7 shows that when $c/H < 0.3$, G/G_{PS} increases linearly with c, i.e.,

$$G/G_{PS} = \omega c/H \Rightarrow G = \omega W(\lambda)c \quad c/H < 0.3 \tag{6.4}$$

where $\omega \approx \pi$. It is important to note that $G \propto W(\lambda)$ for short cracks is a universal relation and can be obtained using a scaling or dimensional argument, as noted by Rivlin [105]. The proportional constant ω is independent of crack length but can depend on the hyper-elasticity model. The result in Fig. 6.7 is for $\lambda = 1.12$. However, we found that the relation between normalized energy release rate and normalized crack length is practically independent of the stretch ratio.

This result shows that when the crack length is short, the specimen can no longer be considered a pure shear crack specimen. Indeed, when $c << H$, the crack geometry approaches an edge crack in an infinite plate Fig. 6.7 or Eq. (6.4) shows that a larger applied stretch is needed to provide the same energy release rate for short cracks (as compared to crack longer than H). This information is provided in Fig. 6.8 where the orange curve is our FEM result

which plots the stretches needed for different crack lengths to maintain the energy release rate of $114.7 J/m^2$. If our assumption that the relation between v and G is unique is true, then cracks with different initial lengths but with the same G ($114.7 J/m^2$) should have the same $v = 0.25 \mu m/s$, which is measured in our experiment. To validate this, we performed experiments with different initial crack lengths and stretched them slowly until the crack propagation speed reaches about $0.25 \mu m/s$. We recorded the stretch ratios at this time and plotted them as dots in Fig. 6.8. We then use FEM to compute the stretch needed to get $G = 114.7 J/m^2$, that is, a constant energy release rate curve. The experimental data is very close to this constant energy release rate curve, which validates the unique relation between v and G.

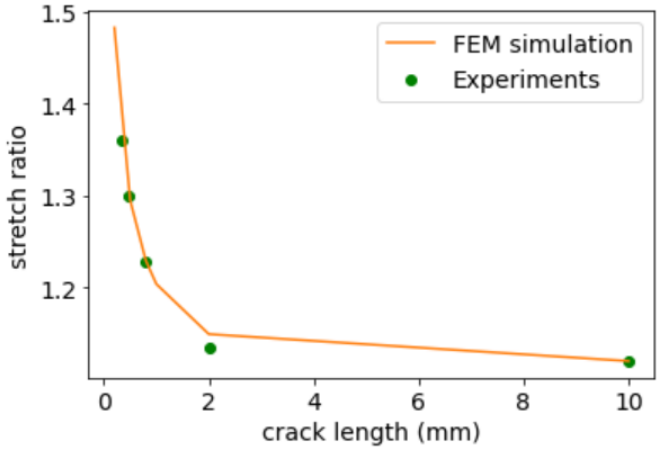

Figure 6.8: Stretch ratios for different crack lengths at a constant crack speed of $0.25 \mu m/s$. These stretch ratios correspond to the same energy release rate of $114.7 J/m^2$

Having established that the crack speed v is a unique function of G, we plot v versus G and find that it fits well to a simple exponential function. The fitting result is plotted in Fig. 6.9 and the relation between v and G is

$$v = v^* e^{G/G^*} \tag{6.5}$$

with $v^* = 1.2 \times 10^{-8} mm/s$ and $G^* = 12.4 J/m^2$.

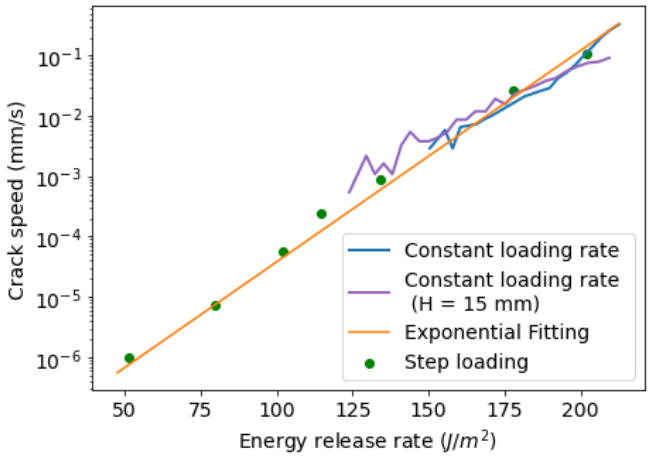

Figure 6.9: Crack speed versus energy release rate

An important feature not shown in Fig. 6.9 is that there can be a threshold energy release rate below which the crack cannot grow. In our experiments, when the energy release rate is lower than $35 J/m^2$, no crack propagation is observed even after 48 hours of holding. However, this could be due to the spatial resolution ($6\mu m$ minimum) of our measurement technique.

6.4 Modeling v versus G

6.4.1 Time-dependent damage model

Our experimental observations show that there exists a unique relation between v and G given by Eq. (6.5). Although the exponential function fits the experimental data very well, it is still a phenomenological result. Here we propose a physical model to explain the origin of this exponential relationship. Our experimental results suggest that the delayed fracture behaviors of PDMS are due to the time-dependent permanent damage of polymer chains in a region near the

crack tip. The basic theory of rate dependent chain scission was established by Eyring [106] and his model has been incorporated into cohesive zone model to study rate dependent fracture in polymers [23]. Here we adopt the formulation of Lavoie et al [107]. In their formulation, the polymer elasticity is represented by many networks, and the chains in each network have equal lengths. To avoid having a large number of undetermined parameters in our model, we consider a simple network where chains have equal length, hence the length of chains is an average length in the real network. In this model, the surviving volume fraction of polymer chains is denoted by b, and the rate of change of b is given by

$$\frac{db}{dt} = -\frac{n_m}{\tau} b \; exp(\frac{L_a f}{k_B T}) \tag{6.6}$$

where L_a is the activation length which is assumed to be constant [107], n_m is the number of monomers in a chain, f is the force acting on a polymer chain, k_B is the Boltzmann's constant and T is the absolute temperature in Kelvin.

In [107], the relation between the chain force f and the extension of a chain is determined using the freely jointed chain model. The extension of a chain is computed based on the affine assumption where the extension of each chain in the network is obtained from the local deformation gradient $\boldsymbol{F}$. Using the Arruda-Boyce constitutive model, f is related to $I_1 = tr(\boldsymbol{B})$ by [107]:

$$f = \frac{k_B T}{l_k} \beta\Big(\sqrt{I_1(\boldsymbol{B})/3n}\Big) \tag{6.7}$$

where l_k is the Kuhn length of the polymer chain, n is the number of Kuhn segments per chain and $\beta\Big(\sqrt{I_1(\boldsymbol{B})/3n}\Big)$ denotes the inverse Langevin function defined by

$$coth - \frac{1}{\beta} = \sqrt{I_1(\boldsymbol{B})/3n} \tag{6.8}$$

However, the use of the Arruda-Boyce model in [107] is inconvenient in that the

inverse Langevin function cannot be written in closed form. Here we introduce a simplification by using an approximation of the Langevin function [108] (less than 5% relative error everywhere) where

$$\beta\Big(\sqrt{I_1(\boldsymbol{B})/3n}\Big) \approx \Big(\sqrt{I_1(\boldsymbol{B})/3n}\Big)\left[\frac{3 - I_1(\boldsymbol{B})/3n}{1 - I_1(\boldsymbol{B})/3n}\right] \tag{6.9}$$

Substituting Eq. (6.9) into Eq. (6.7) shows that the chain force is related to the deformation by

$$f = \frac{k_B T}{l_k}\sqrt{I_1(\boldsymbol{B})/3n}\left[\frac{3 - I_1(\boldsymbol{B})/3n}{1 - I_1(\boldsymbol{B})/3n}\right] \tag{6.10}$$

The chain breaking kinetics Eq. (6.6) can be expressed in terms of continuum quantities by substituting Eq. (6.10) into Eq. (6.6), resulting in

$$\frac{db}{dt} = -\frac{n_m}{\tau} b\, exp\left(\frac{L_a}{l_k}\sqrt{\frac{I_1(\boldsymbol{B})}{3n}}\left[\frac{3 - I_1(\boldsymbol{B})/3n}{1 - I_1(\boldsymbol{B})/3n}\right]\right) \tag{6.11}$$

In this model, damage takes time to develop. However, due to the exponential function in Eq. (6.11), the rate of damage increases exponentially fast as a chain reaches the limit of its extensibility. In the continuum model, this occurs when $I_1(\boldsymbol{B}) \to 3n$, and db/dt becomes unbounded.

6.4.2 Calculating crack propagation speed using chain damage model

In the following, we determine the relation between crack growth rate v and the applied energy release G rate in a PS specimen using a simple analytic model. We assume steady state crack growth. Under this assumption, the continuum field is independent of time with respect a coordinate system (x, y) fixed to the moving crack tip in the reference configuration. The steady state assumption

implies that the material derivative of b, Db/Dt is given by

$$\frac{Db}{Dt} = -v\frac{\partial b}{\partial x} \tag{6.12}$$

where v is the speed of the crack, $b = b(x, y)$ in the moving coordinate system. Substituting Eq. (6.12) into Eq. (6.11), we have

$$v\frac{\partial b}{\partial x} = -\frac{n_m}{\tau} b \; exp\left(\frac{L_a}{l_k}\sqrt{\frac{I_1(\boldsymbol{B})}{3n}}\left[\frac{3 - I_1(\boldsymbol{B})/3n}{1 - I_1(\boldsymbol{B})/3n}\right]\right) \tag{6.13}$$

A difficulty with the damage model of Eq. (6.13) is that healing is neglected, hence damage occurs irrespective of the stress/strain level. While this assumption is reasonable near the crack tip, it is incompatible with the steady state assumption since the material as $x \to \infty$ is undamaged. To bypass this difficulty, we introduce a cut-off effective strain, represented by I_c, such that the damage rate is zero for $I_1 \leq I_c$. We also impose the fracture condition that crack growth occurs when the damage reaches a critical fraction b_c at a microscopic distance x_c directly ahead of the crack tip. These assumptions allow us to integrate Eq. (6.13) directly ahead of the crack tip ($y = 0$) to yield

$$v = \frac{n_m}{\tau ln(1/b_c)} \int_{x_c}^{L} exp\left(\frac{L_a}{l_k}\sqrt{\frac{I_1(\boldsymbol{B})}{3n}}\left[\frac{3 - I_1(\boldsymbol{B})/3n}{1 - I_1(\boldsymbol{B})/3n}\right]\right) \tag{6.14}$$

To complete the analysis, we need to know how $I_1(\boldsymbol{B})$ varies with x. In general, this strain field is coupled to the damage. To simplify the analysis, we assume the damage zone is sufficiently small so that the strain field is the same as a semi-infinite crack in a hyper-elastic solid obeying the 3 term Yeoh's model (Eq. (6.3)). The simulation is performed using Abaqus (see A.6.2). This assumption is justified since the damage zone is found to be roughly $20\mu m$ and is indeed very small in comparison with specimen dimension. In addition, since the PS is under displacement control, the effect of damage is reflected in the stress field instead of the strain field, so the hyper-elastic model field should provide a good approximation of the strain field.

There are 5 independent parameters in our model, $\{n_m/[\tau ln(b_c)], x_c, I_c, nL_a/l_k\}$ and we choose these parameters to fit the experimental data. The fitting results are shown in Fig. 6.10. The figure shows that the model can predict the crack speed observed in experiments quantitatively. The parameters are

$$\{n_m/[\tau ln(b_c)], x_c, I_c, nL_a/l_k\} = \{-59.58, 6.1\mu m, 4.439, 2.210, 0.9883\} \tag{6.15}$$

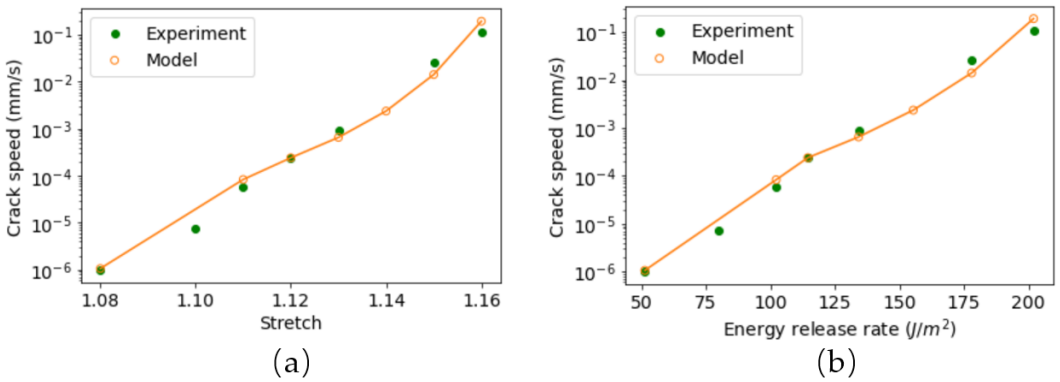

Figure 6.10: Fitting result of polymer chain damage model. (a) Crack growth speed versus stretch. (b) Crack growth speed versus energy release rate.

6.4.3 Delayed fracture in PS samples with different crack lengths

We are now ready to analyze how crack geometry controls DF. To recap, sharp cracks in PS samples fail at lower stretch ratios than in DEC samples. The mode of failure is slow, steady crack growth. We emphasize that these experiments are conducted with cracks longer than sample height H. In contrast, blunt crack samples fail at higher stretch ratios and the failure mode is sudden rapid crack growth. Superficially, it seems that these two phenomena are unconnected. In

the following, we show that the underlying failure mechanism is the same and they can be understood using the same model.

We first present data on DF tests with very short sharp cracks (c = 0.8–0.34mm) in PS samples. The samples are stretched to λ = 1.23–1.30 with a stretch rate $0.1/s$ and then held fixed. Note these stretch ratios are much larger than those needed to grow a long starter crack. Photos are taken during holding and the time evolution of crack length is recorded. As shown in Fig. 6.11(a)-(d), the crack propagates very slowly at first, but the crack speed keeps increasing. In Fig. 6.11 (a), after 400 seconds, the crack speed suddenly increases rapidly and breaks the sample in less than 3 seconds.

The crack length evolution can be understood using a simple physical argument. At the beginning, the crack length is very short and since the energy release rate is directly proportional to the crack length (see Fig. 6.7), it is also very small. Small energy release rate means slow crack growth rate, as predicted by our model, Eq. (6.1) (see also Fig. 6.9 and Fig. 6.10). Once the crack grows, the crack length increases, which leads to the increase of energy release rate. Higher energy release rate leads to higher crack speed. This positive feedback and the fact that crack speed depends exponentially on G make the crack grow faster and faster, and finally cause the catastrophic failure of the sample. This argument will be justified rigorously below.

In Fig. 6.11(a), the crack speed seems to approach infinity when the crack length is slightly below 1.5mm (short crack). This is the case for all the initial crack lengths in Fig. 6.11. Hence the energy release rate in these experiments is given by Eq. (6.4). Using Eq. (6.1) and Eq. (6.4) and $v = dc/dt$. The rate of change

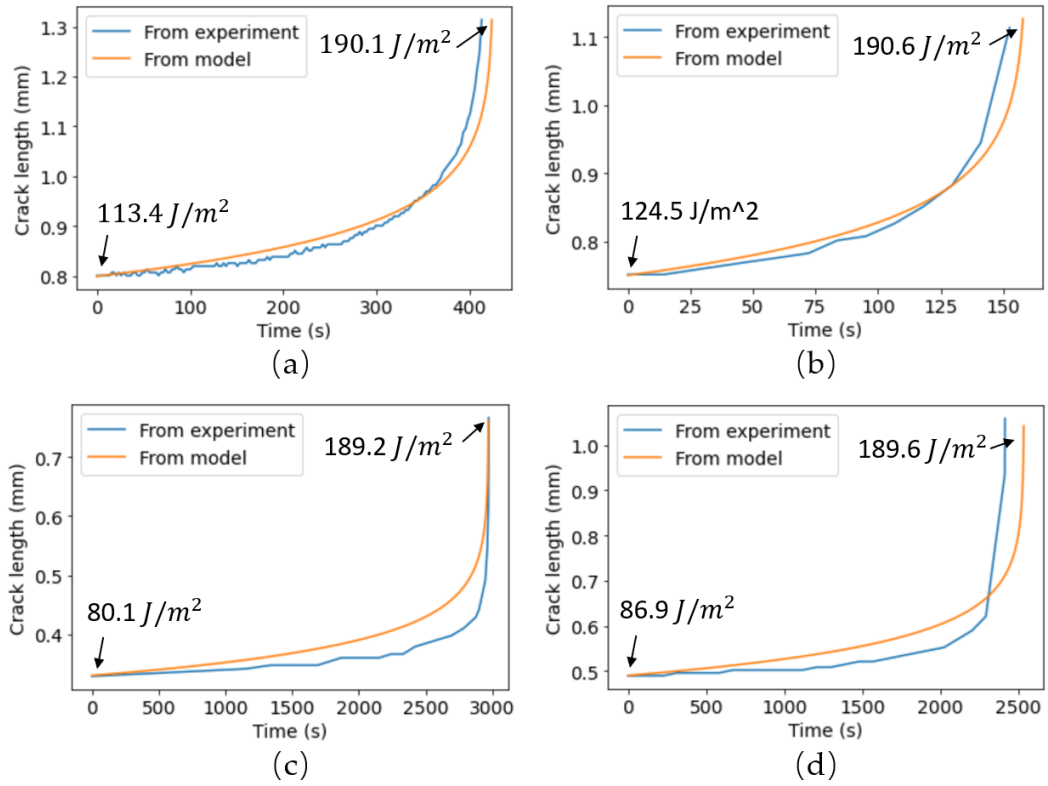

Figure 6.11: Delayed fracture tests on sharp crack samples for 4 initial crack lengths. (a) 0.80mm crack with stretch 1.23, (a) 0.75 mm crack with stretch 1.25, (b) 0.49mm crack with stretch 1.26, (c) 0.34 mm crack with stretch 1.30. Energy release rate values noted on the figures refer to G for the starter crack at the indicated stretch and G at the point that the crack grows unstably.

of crack length obeys the differential equation

$$\frac{dc}{dt} = v^* e^{W(\lambda)\alpha c/G^*} \tag{6.16}$$

The solution of Eq. (6.16) subjected to the initial condition $c(t = 0) = c_0$ where c_0 is the initial crack length. Then $c(t)$ is

$$c(t) = c_0 - \frac{G^*}{W(\lambda)\alpha} ln\left[1 - \frac{t}{t_{max}}\right] \tag{6.17}$$

where

$$t_{max} = \frac{G^* e^{-G_0/G^*}}{G_0} \frac{c_0}{v^*} \tag{6.18}$$

and

$$G_0 = \alpha W(\lambda) c_0 \tag{6.19}$$

is the energy release rate of the initial crack. The dependence of crack growth rate on time is obtained by differentiating Eq. (6.17), i.e.,

$$v = \frac{dc}{dt} = \frac{G^*}{G_0} \frac{1}{1 - t/t_{max}} \frac{c_0}{t_{max}} \tag{6.20}$$

Note that the crack growth rate approaches infinity as t approaches t_{max}. Eq. (6.20) captures the rapid increase of crack velocity in Fig. 6.11. The predicted crack length using Eq. (6.17), Eq. (6.18) and Eq. (6.19) fits the experimental crack length well.

One interesting feature in all four tests is the rapid increase in crack speed happens at roughly the same energy release rate ($\sim 190 J/m^2$). From Fig. 6.9 and Fig. 6.10, we can see that at this energy release rate, the crack speed reaches $0.1 mm/s$. In all these short crack tests, the cracks grow roughly $0.1 - 0.3 mm$ before catastrophic failure occurs.

These results suggest a simple explanation of why rapid crack growth is associated with delayed fracture in blunt crack specimens. Our results above suggest that when very small cracks are present directly ahead of the notch tip in blunted crack specimens, these short cracks propagate slowly, and are not easily observable, (see Fig. 6.4), but once they reach a certain size (roughly on the order of the size of the circular hole or notch size), they can accelerate rapidly since the energy release rate is very high and the shielding effect of the hole is lost. Note that the energy release rate is high because the applied stretch ratio is much higher than the applied stretch ratio for cracks of the same length in the PS samples.

6.5 Summary and discussion

A comprehensive study for the delayed fracture of PDMS is carried out to study DF in different crack specimens containing sharp and blunted cracks. Our experiments showed that DF is caused by localized damage due to rate dependent bond breaking. In blunted crack samples, DF occurs at a higher energy release rate and crack growth is catastrophic. In contrast, in sharp crack samples, DF occurs at much lower energy release and crack growth is slow and steady. Experimentally, we found that the velocity of crack growth is uniquely related to the energy release rate. In particular, the crack velocity is an exponential function of the energy release rate. We also derive this v versus G relation using a fracture model based on rate dependent chain breaking kinetics and found good agreement between theory and experiments.

Our experiments and theory strongly suggested that DF in samples with blunted and sharp cracks are governed by the same micromechanics of chain breaking. Once a small crack is formed in blunted samples, the crack growth rate can be explained by the universal relation between crack growth rate and energy release rate given by Eq. (6.5). In other words, DF can be explained by combining chain breaking kinetics with concepts from nonlinear fracture mechanics.

The result in Fig. 6.3 (a) can be explained by the interaction between chain breaking and elastic field. Fig. 6.3 (a) shows that the stretch at a fixed point directly ahead of the blunted tip increases very rapidly for the first few minutes after holding and then continues to increase at a much slower rate. In an elastic solid, this increase is impossible since the strain distribution is fixed and cannot

change with time during relaxation. The cause of this increase is due to time dependent damage caused by chain breaking. . Indeed, our damage model implies that damage softens the material by decreasing the effective shear modulus $2c_1$ to $b \times 2c_1$ (recall $2c_1$ is the shear modulus in Yeoh's model). This means that there is a region of softened material near the notch tip, surrounding this softened region is undamaged material which is substantially stiffer. Since the average spatial strain during relaxation must be constant, strain is transferred to the softer material near the notch tip, as a result, the strain of the material near the notch tip increases, this increase in strain is compensated by equal decrease of average strain in the surrounding stiffer solid. To understand the rapid increase in strain, we appeal to the fact that the network strands in PDMS have a wide molecular weight distribution. As a consequence, the short strands break rapidly due to the strain concentration near the notch tip. After this initial period of rapid breaking, all the short strands are broken. The remaining long strands require much higher strain to break rapidly, but can gradually break as they are aided by thermal fluctuation. This explains the slow increase in strain over hours.

An interesting issue raised by this work is the meaning of fracture toughness for materials with time-dependent damage, like PDMS. In fracture mechanics, the toughness is the minimum energy release rate required to initiate crack growth so it should correspond to the energy release rate below which crack growth rate is zero. However, in most experiments measuring toughness, this value is usually obtained by stretching a PS sample with constant loading rate until the crack length has noticeable increase. This toughness is much higher than the critical energy release rate for crack growth we observed, which is between $35J/m^2$ to $50J/m^2$. As noted earlier, there may exist a threshold energy

release rate below which delayed fracture does not occur. Here we note that, in theory, there exists an energy release rate for PDMS below which crack growth cannot occur - which is the surface energy. For PDMS, the surface energy has been measured [109] and is found to be $21.6mJ/m^2$. Thus, this "critical" energy release rate must be greater than $43.2mJ/m^2$, which is unrealistically small. As noted by Lake and Thomas [110], the toughness of elastomers is much greater than its surface energy since when a chain breaks, it losses all its strain energy.

In LT theory [110], toughness is given by the product of the number of effective load bearing chain crossings per unit reference area, of the average number of monomers per chain and of the energy needed to break the chemical bond between monomers. LT [110] shows that this fracture energy is given by $\Gamma_{LT} = \sqrt{3/8}\gamma l U \xi$, where l is the monomer length, γ is a factor determined by the freedom of rotation about bonds in the chain which influences the flexibility, which we taken to be one, U is the energy needed to break a polymer bond and $\xi = N\overline{n}^{3/2}$, where $\overline{n}$ is the number of monomer unit in a chain, and N is the number of effective load bearing chains per unit volume, N can be obtained using polymer physics [111]. For PDMS, our estimation for N is

$$N = \frac{\mu}{kT} = \frac{0.44 \times 10^6 Pa}{4.11 \times 10^{-21} J} \approx 10^{26}/m^3 \tag{6.21}$$

The average number of monomer units per chain is

$$\overline{n} \approx \frac{\rho}{mN} \tag{6.22}$$

where m is the mass of a single monomer unit and ρ the mass density. The repeated unit of PDMS is $Si(CH_3)_2O$ and the mass density is $965kg/m^3$. So the mass per monomer is about $1.27 \times 10^{-25} kg$. This gives

$$\overline{n} = \frac{\rho}{mN} = \frac{965kg/m^3}{1.27 \times 10^{-25} kg \times 10^{26}/m^3} \approx 80 \tag{6.23}$$

For this we can find

$$\xi = N\overline{n}^{3/2} \approx (80)^{3/2} \times 10^{26}/m^3 \tag{6.24}$$

Taking the monomer length of PDMS to be 10 Angstroms, the toughness predicted by LT is

$$\Gamma_{LT} = \sqrt{3/8}\gamma l U \xi \approx \sqrt{3/8} \times 10 \times 10^{-10} m \times 3 \times 10^{-19} J \times 10^{26}/m^3 \times (80)^{3/2} = 13.1 J/m^2 \tag{6.25}$$

This is the lower bound for "fracture toughness", since it assumes all the damage is confined to a single plane directly ahead of the crack tip. Thus, if the threshold energy for crack growth exists, it should be higher or equal to LT energy. In our experimental observations, the threshold energy for crack propagation is about $35 J/m^2$, which is two times higher than the LT energy.

It should be noted in this study, the crack length is always much greater than the damage zone size or the radius of the blunted crack, this is the reason why fracture mechanics is applicable. If the size of the damage zone is comparable to the crack length, DF can no longer be governed by a single parameter, G. In the literature, this corresponds to samples that are notch insensitive [84, 112]. A key length scale proposed to quantify notch sensitivity is the fracto-cohesive length $l_f = \Gamma/W_f$ [112], where Γ is the fracture toughness of the material and W_f is its work of extension which is the energy per unit volume to fail an uncracked tension sample. If the crack length is smaller than Γ/W_f, the sample is notch insensitive and fracture mechanics approach is not valid. For PDMS in this study, l_f is estimated to be $13\mu m$ (with $\Gamma = 35 J/m^2$ and $W_f = 2.69 MPa$, see A.5.2), which is consistent with our experimental results and damage model. For example, in blunt crack samples, before catastrophic failure, the size of the small crack is roughly $80\mu m$. For sharp crack samples, using our damage model, when we have a $50\mu m$ initial crack, a nominal stretch ratio of 2.5 is needed to reach a crack

speed $0.1mm/s$, which is very close to the fracture stretch ratio of 2.6 in uniaxial tension. Here we note another length scale in soft material fracture is the elasto-adhesive length $l_e = \Gamma/E$ [1, 113], where E is the small strain Young's modulus. This length represents the typical distance from a crack tip below which the deformation is dominated by elastic nonlinearity at the onset of crack initiation [1]. Thus, fracture mechanics cannot be applied if the damage zone size is on the same order as Γ/E. Interestingly, for our PDMS system, $E = 1.3MPa$, $l_e = \Gamma/E \approx 26\mu m$ which is roughly the same order as the fracto-cohesive length.

APPENDIX A

APPENDIX

A.1 Implementation of GP

This part is done with the help of Tianjiao Li at Cornell University.

The singular value decomposition (SVD) and Gaussian Process (GP) were performed using Python 3.7 in Jupter 6.0.1.

The `GaussianProcessRegressor` module in `sklearn` package requires an optimizer function as input. By default, `'fmin_l_bfgs_b'` algorithm implemented in `scipy.optimize.minimize` is used:

```
class sklearn.gaussian_process.GaussianProcessRegressor(kernel=None,
    *, alpha=1e-10, optimizer='fmin_l_bfgs_b', n_restarts_optimizer=0,
     normalize_y=False, copy_X_train=True, random_state=None)
```

However, the default maximum number of iteration `maxiter` in `scipy.optimize.minimize` does not seem to be sufficient for the presented example of PVA constitutive model and the default setting gives rise to errors. To solve this issue, we define our optimizer by keeping the `'fmin_l_bfgs_b'` algorithm and modifying the optimizer by setting `options = {'maxiter':30000}`:

```
def my_optimizer(obj_func, initial_theta, bounds):
    opt_res = scipy.optimize.minimize(
                obj_func, initial_theta, method="L-BFGS-B", jac=True,
                bounds=bounds, options = {'maxiter':30000})
    theta_opt, func_min = opt_res.x, opt_res.fun
    return theta_opt, func_min
```

And we create our $\mathcal{GP}$ instances as:

```
kernel = C(1.0, (1e-4, 1e10)) * RBF([5, 5, 5, 5], (1e-3, 1e4)) #
    anisotropic kernel
gp = GaussianProcessRegressor(kernel=kernel,
                              alpha=0.1^2, # value added to the
    diagonal of the kernel
                              optimizer=my_optimizer,
                              n_restarts_optimizer=10,
                              normalize_y = True)
```

A.2 Active learning for Gaussian process

The active learning for GP is done by Tianjiao Li at Cornell University.

To make this study more comprehensive, here we did some active learning studies for Gaussian process, with PVA constitutive model. Instead of starting from 1000 parameters, this time we choose smaller training set at the beginning.

We are aware that there are other methods to construct the training set. Active learning scheme is one of the most popular to construct the training set on demand. In Gaussian process machine learning, it is a common practice to leverage the predictive variance and use a highest-variance search algorithm to populate the training set on the fly during training. The algorithm is described below:

Algorithm 1 Active learning of Gaussian process model using highest variance search

Input
- T total number of iterations
- $S_{T,1}$ initial training set (label known)
- A_1 stress matrix associated with $S_{T,0}$
- $S_{R,1}$ initial reference set (label unknown)
- $|S_{C,i}|$ size of the set of chosen points in each iteration

Output
- $\mathcal{GP}$ trained Gaussian process model

Initialize the Gaussian process model $\mathcal{GP}$
for t in $[T]$ **do**
    Update $\mathcal{GP}$ with $S_{T,t}$ and their labels
    Use $\mathcal{GP}$ to make predictions on $S_{R,t}$ and get the predictive mean and variance
    Pick $|S_{C,i}|$ points in $S_{R,t}$ with the highest predictive variance and put them into $S_{C,t}$
    $S_{T,t+1} \leftarrow S_{T,t} \bigcup S_{C,t}$
    $S_{R,t+1} \leftarrow S_{R,t} \setminus S_{C,t}$
    Calculate the stress histories of these $|S_{C,t}|$ points and add them to A_t to get A_{t+1}
    Apply SVD to A_{t+1} to get the labels for $S_{T,t+1}$
end for

To characterize the performance of highest-variance-search active learning, we apply Algorithm 1 to the learning tasks in the presented work. We argue that this algorithm is effective for reducing the size of the training set, but particularly in the presented research, it is not necessary. We show this by analyzing the example of learning the first $\mathcal{GP}$ in the first experiment (EXP 1. $k = 1$).

When running Algorithm 1, we tested different sizes of the set of the chosen points, namely $|S_{C,i}| \in \{5, 10, 15, 20\}$. Besides, to characterize the quality of the models across the training history, we constructed an independent validation set of randomly distributed 1000 points in Ω, on which we compute the root mean square error (RMSE) of the model predictions across the training history.

We also keep track of the cumulative time used Algorithm 1 as a function of the size of the training set. The results are shown in Fig. A.1, where the performance of the model trained on 1000 LHS points in our presented work is the baseline.

From Fig. A.1, we can see that to get equivalent or better accuracy as the baseline model, the minimum number of the training points is roughly $275, 320, 490, 440$ for $|S_{C,i}| = 5, 10, 15, 20$, respectively. This demonstrates the power of highest-variance search in reducing the size of the training set. However, to update the $\mathcal{GP}$, in each iteration, an individual training process needs to be carried out. This creates significant overhead. Smaller size of $|S_{C,i}|$ means more frequent updates (training), resulting in a rapidly increasing cumulative time. For example, for $|S_{C,i}| = 5$, to reach the point where the number of the training points is 275, the cumulative time is effectively identical to the baseline. Also, larger size of $|S_{C,i}|$ results in slower convergence of the validation error, probably because when $|S_{C,i}|$ is large, many points in $S_{C,i}$ don't carry much useful information to effectively update the $\mathcal{GP}$. Moreover, notice that we only observe the minimum needed number of training points in hindsight. In actual active learning, it won't be easy to immediately tell if the training has converged. As a result, in practice, it may take more time to conduct active learning.

This result implies that in the presented work, although the evaluation of the constitutive model is slow enough to make manual model fitting infeasible, it is not sufficiently slow to make the active learning scheme effective. In cases where evaluating the constitutive model takes extremely long time, active learning will be significantly more efficient.

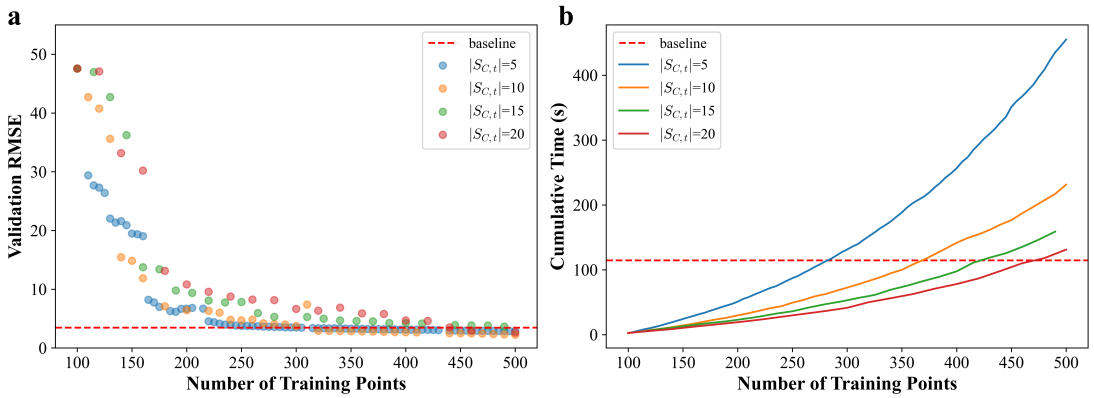

Figure A.1: Validation error and cumulative time for $|S_{C,i}| \in \{5, 10, 15, 20\}$ in active learning.

A.3 Implementation of Neural network training

The Neural network is built using torch.nn.Module in Pytorch. The linear function is `torch.nn.linear(input_size, output_size)` and the activation function is `torch.nn.Softplus()`. For example, for PVA gel, the final neural network with two hidden layers is represented by:

```
class Net(nn.Module):
    def __init__(self):
        super(Net, self).__init__()
        self.layer = []

        # Linear part for first hidden layer
        self.layer.append(torch.nn.Linear(4, 32))
        # Activation for first hidden layer
        self.layer.append(torch.nn.Softplus())
        # Linear part for second hidden layer
        self.layer.append(torch.nn.Linear(32, 32))
        # Activation for second hidden layer
```

```
        self.layer.append(torch.nn.Softplus())
        # Output layer, 4 principal values
        self.layer.append(torch.nn.Linear(32, 4))
        # Combine all layers together
        self.nn_layer = torch.nn.Sequential(*self.layer)

    def forward(self, x):
        x = self.nn_layer(x)    # x is the input and y is the output
        return x
```

For the implementation of adaptive neural network, `Net()` with different layers and nodes are generated automatically using a `for` loop, following the rule below.

$$\frac{\{32,32\}}{two\ layers} \rightarrow \frac{\{32,64,32\}}{three\ layers} \rightarrow \frac{\{32,64,64,32\}}{four\ layers} \rightarrow \frac{\{32,64,128,64,32\}}{five\ layers} \rightarrow \cdots\cdots \tag{A.1}$$

The the loss function for training and prediction is

$$err_{train} = \frac{1}{|\Omega_T|} \sum_{\vec{x}_j \in \Omega_T} \frac{||\vec{\psi}_{NN}(\vec{x}_j) - \vec{\psi}(\vec{x}_j)||}{||\vec{\psi}_{NN}(\vec{x}_j)||} \tag{A.2}$$

which is implemented using

```
class Relative_Loss(nn.Module):
    def __init__(self):
        super(RMSELoss,self).__init__()
    def forward(self,x,y):
        loss = torch.sum(torch.square(x - y) , axis= 1) / torch.sum(
   torch.square(y), axis = 1)
        loss = torch.sqrt(loss)
        loss = torch.sum(loss)/loss.shape[0]
        return loss
```

The training of the neural network is based on Adam gradient descent method. All data in the training set are fed to the neural network at the same time to get the training error. Simple speaking, gradient descent method is applied to optimize the weights of all nodes so they can give us the training error as low as possible. Specifically, we use Adam optimizer to help us optimize all the weights, and the command for Adam optimizer in Pytorch is

```
optimizer = torch.optim.Adam(net.parameters(), lr = 0.002,
                             betas = (0.99, 0.999), eps=1e-08,
                             weight_decay=1e-5)
```

where "lr" means the learning rate, "betas" means the coefficients used for computing running averages of gradient and its square, "eps" is the term added to improve numerical stability, and "weight_decay" means the weight decay (or L2 penalty). More details about it can be found in "https://pytorch.org/docs/stable/generated/torch.optim.Adam.html". The optimizer does one step of gradient descent and updates all the weights, which is called one step, or one epoch. Many epochs are conducted to train a neural network until the error cannot be smaller. To be specific, when the relative change of error is smaller than 10% between 10000 epochs, we stop training and determine whether to increase the number of layers or to go to the validation part.

A.4 Relaxation test for T-shape sample in oil

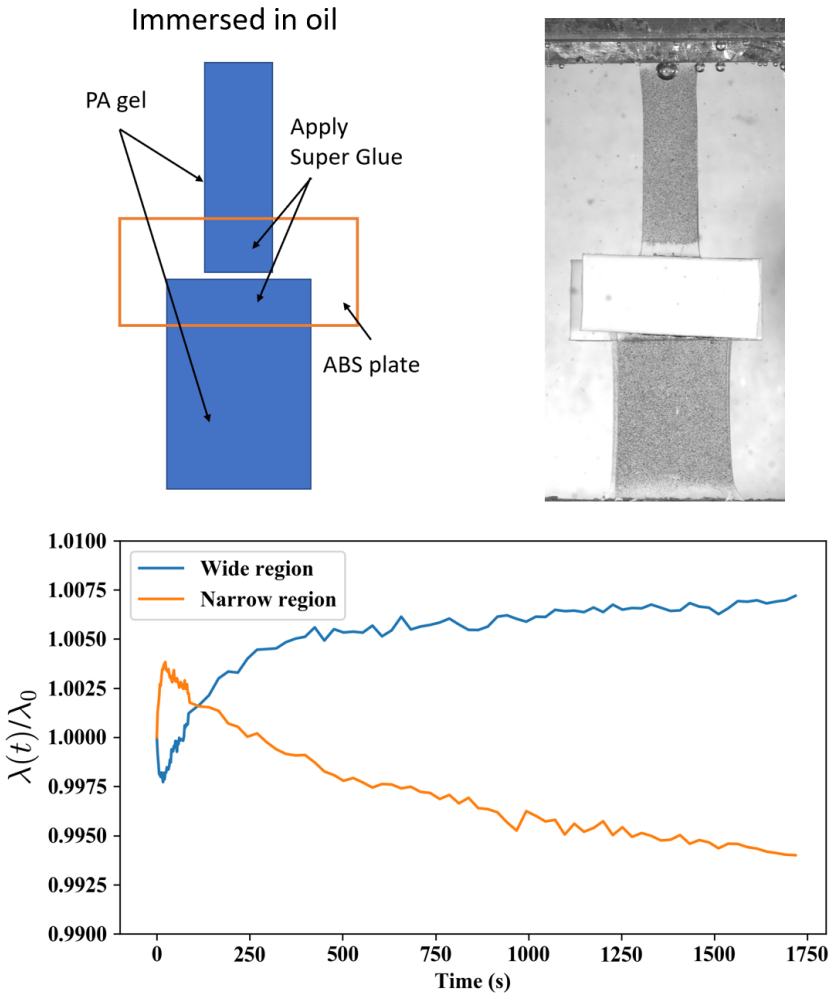

Figure A.2: T-shape test for $c - PA_{strong}$ immersed in mineral oil

The sample is made of two separate parts so there is no water flow within this sample. The sample is stretched to $\lambda_N = L/L_0 = 1.3$ with a fast stretch rate of $0.1/s$ and then held at the deformed length $L = 1.3L_0$ for half an hour. The curves show the time evolution of stretch at narrow and wide sections, which have the same trend as the curve of T-shape test in water.

A.5 Characterization of PDMS

A.5.1 Pheology test for PDMS

The rheology test for PDMS was done with a torsion rheometer (Discovery Hybrid Rheometer HR-3, TA instruments). A cylindrical sample of radius 10 mm and height 2mm was cut using a circular cutter. A small precompression (1-2 *N* force) is imposed on the sample to prevent slip and then cyclic torsion was applied with different frequencies, from 0.01Hz to 50Hz. The frequency scan was done using different strain amplitudes, 0.5%, 1% and 2%, and all results are almost the same to each other. Our results are in good agreement with literature [102].

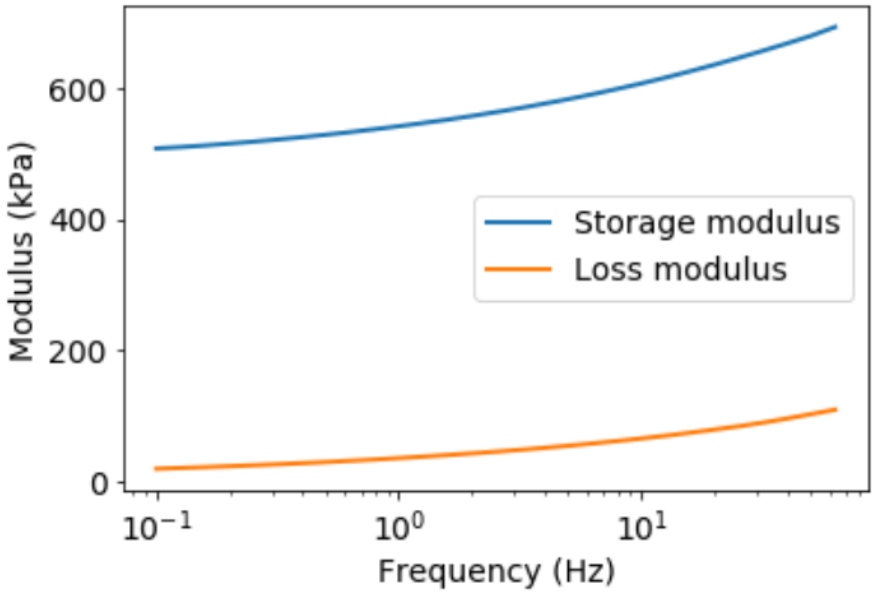

Figure A.3: Rheology test for PDMS

A.5.2 Uniaxial tension test for PDMS

The data fitting for PDMS uniaxial tension is done with the help of Bangguo Zhu at Cornell University.

As we mentioned in section 6, the uniaxial tension date of PDMS is fitted using a 3-term Yeoh's hyper-elastic model. The strain energy density function is

$$W(\lambda) = \sum_{k=1}^{3} c_k (I_1 - 3)^k, \qquad I_1 = \lambda^2 + 2\lambda^{-1} \tag{A.3}$$

Fig. A.4 shows the fitting result, and the parameters are

$$c_1 = 0.2215MPa \quad c_2 = 4.4873 \times 10^{-2} MPa \quad c_3 = 6.9596 \times 10^{-3} MPa \tag{A.4}$$

Then, by calculating the area under the blue curve, we can get the work to rupture W_f

$$W_f = \int_1^{\lambda_f} s d\lambda = 2.69MPa \tag{A.5}$$

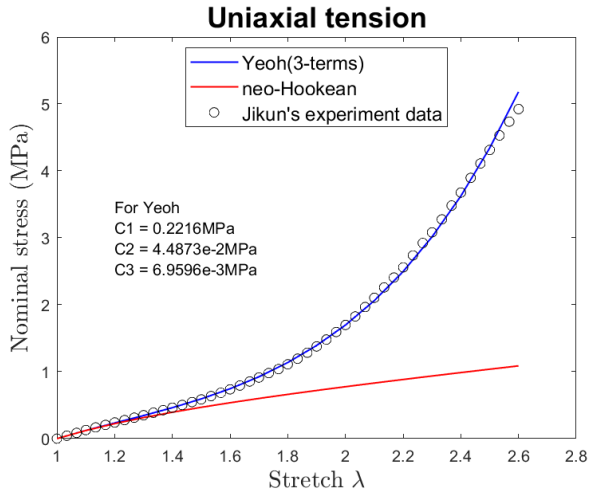

Figure A.4: Fitting of PDMS uniaxial tension test using 3-term Yeoh's model. From the comparison with neo-Hookean model, there is strong strain-hardening effect in PDMS.

A.5.3 Strain concentrating in single edge blunt crack sample

For single edge blunt crack samples. When the radius of the notch is not small enough, the stress concentration is not high enough so defects from the clamped edges of PS samples often nucleate and grow before the blunted crack grows. As shown in Fig. A.5.

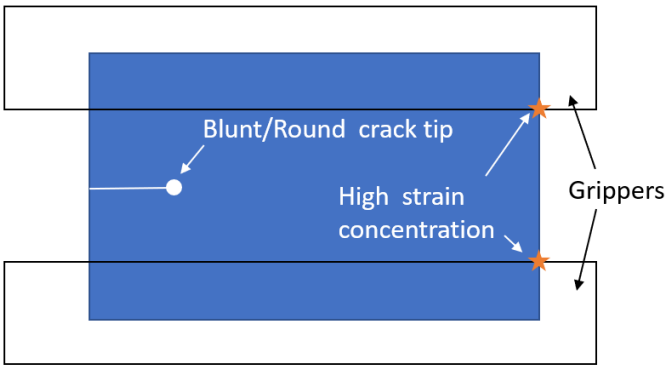

(a)

(b)

Figure A.5: Strain concentration in single edge blunt crack sample. (a) Illustration of strain concentration at the edge. (b) Experimental picture for crack growing from the edge. The radius of the notch tip is 0.25mm.

A.6 Numerical simulations of PDMS PS samples with sharp crack

The numerical simulations of PDMS is done by Bangguo Zhu at Cornell University.

A.6.1 Calculating energy release rate for sharp cracks with different lengths

The J-integral is utilized to compute the energy release rate numerically. In commercial FEM software Abaqus, the numerical evaluations of the J-integral are provided based on the virtual crack extension/domain integral methods. Following the procedure stated in the Abaqus documentation, we can determine the energy release rate for a 2D pure shear sample with varying crack lengths. The numerical results are verified through several ways. Firstly, the J-integral values for different integral "contours" (Fig. A.6) are found to be reasonably close. Secondly, even with significant mesh refinement, the J-integral value remains close to the original value. Thirdly, in theory, the energy release rate G_{PS} can be calculated for an ideal pure shear sample with a much longer crack length than the height and thickness of the specimen. The amount of strain energy released per unit crack area is equivalent to the strain energy stored in the stripe under pure shear state of height H. As illustrated in Fig. 6.7, when crack length is greater than H, the FEM-derived energy release rate remains relatively constant and is close to G_{PS}.

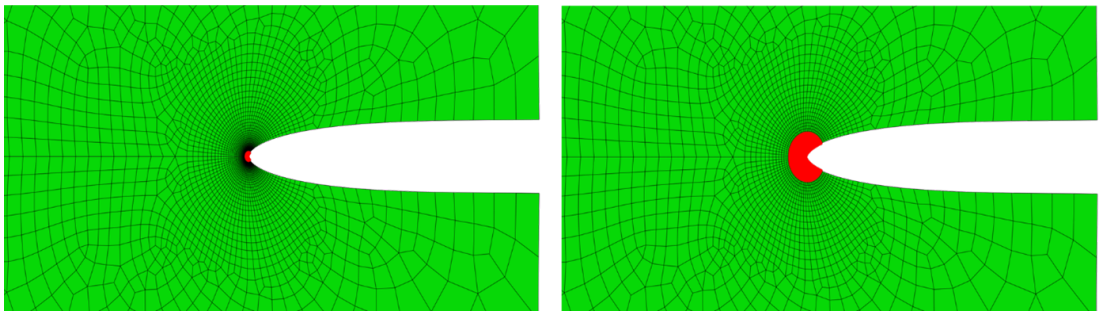

Figure A.6: Different "contours" (domains, marked in red) used to evaluate the J-integral in Abaqus. In Abaqus, the closed path integral is converted into the domain integral.

A.6.2 Evaluate Eq. (6.14) for long sharp crack

To complete the evaluation of Eq. (6.14). We use FEM simulation to get $I_1(B)$ as a function of x, the distance ahead of the crack tip. The equation is

$$v = \frac{n_m}{\tau ln(1/b_c)} \int_{x_c}^{L} exp\left(\frac{L_a}{l_k}\sqrt{\frac{I_1(\boldsymbol{B})}{3n}}\left[\frac{3 - I_1(\boldsymbol{B})/3n}{1 - I_1(\boldsymbol{B})/3n}\right]\right) \tag{A.6}$$

The simulation is implemented with the 3-term Yeoh's model, under the assumption that the damage zone near the crack tip is sufficiently small so the strain field in PDMS is almost the same as a semi-infinite crack in a hyperelastic solid. The simulation results are shown in Fig. A.7. Fig. A.7 (a) shows the meshes in deformed state and Fig. A.7 (b) shows the strain field in deformed state. Same simulations are implemented for different stretch ratios. The strain along the integrating path is used to evaluate Eq. (6.14) or Eq. (A.6).

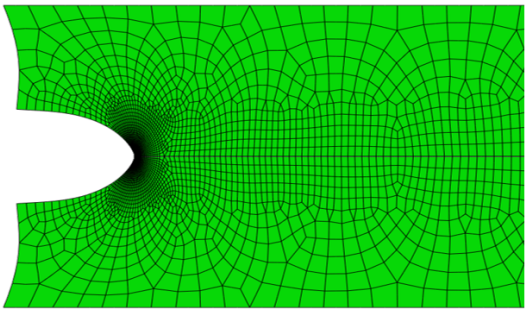

(a)

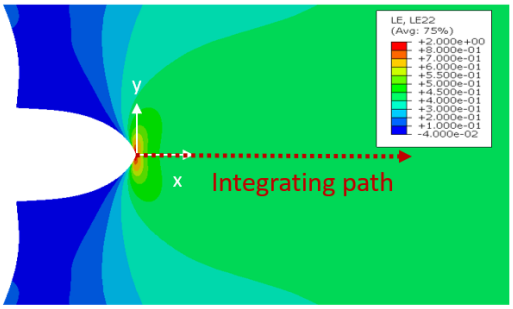

(b)

Figure A.7: FEM simulation for PS samples with a long sharp crack. (a) Meshes in deformed state. (b) Strain field and integrating path in deformed state.

BIBLIOGRAPHY

[1] Costantino Creton and Matteo Ciccotti. Fracture and adhesion of soft materials: a review. *Reports on Progress in Physics*, 79(4):046601, 2016.

[2] Zishun Liu, William Toh, and Teng Yong Ng. Advances in mechanics of soft materials: A review of large deformation behavior of hydrogels. *International Journal of Applied Mechanics*, 7(05):1530001, 2015.

[3] Carmel Majidi. Soft-matter engineering for soft robotics. *Advanced Materials Technologies*, 4(2):1800477, 2019.

[4] Canhui Yang and Zhigang Suo. Hydrogel ionotronics. *Nature Reviews Materials*, 3(6):125–142, 2018.

[5] Jikun Wang, Tongqing Lu, Meng Yang, Danqi Sun, Yukun Xia, and Tiejun Wang. Hydrogel 3d printing with the capacitor edge effect. *Science Advances*, 5(3):eaau8769, 2019.

[6] Ihor Tokarev and Sergiy Minko. Stimuli-responsive porous hydrogels at interfaces for molecular filtration, separation, controlled release, and gating in capsules and membranes. *Advanced Materials*, 22(31):3446–3462, 2010.

[7] Somasundar Mantha, Sangeeth Pillai, Parisa Khayambashi, Akshaya Upadhyay, Yuli Zhang, Owen Tao, Hieu M Pham, and Simon D Tran. Smart hydrogels in tissue engineering and regenerative medicine. *Materials*, 12(20):3323, 2019.

[8] Ronald A Siegel, Yuandong Gu, Ming Lei, Antonio Baldi, Eric E Nuxoll, and Babak Ziaie. Hard and soft micro-and nanofabrication: An integrated approach to hydrogel-based biosensing and drug delivery. *Journal of controlled release*, 141(3):303–313, 2010.

[9] Xuanhe Zhao. Multi-scale multi-mechanism design of tough hydrogels: building dissipation into stretchy networks. *Soft matter*, 10(5):672–687, 2014.

[10] Andrews Victor, JE Ribeiro, and Fernando F Araújo. Study of pdms characterization and its applications in biomedicine: A review. *Journal of Mechanical Engineering and Biomechanics*, 4(1):1–9, 2019.

[11] Hyunwoo Yuk, Teng Zhang, German Alberto Parada, Xinyue Liu, and Xuanhe Zhao. Skin-inspired hydrogel–elastomer hybrids with robust interfaces and functional microstructures. *Nature communications*, 7(1):12028, 2016.

[12] Jian Ping Gong. Why are double network hydrogels so tough? *Soft Matter*, 6(12):2583–2590, 2010.

[13] Jian Ping Gong, Yoshinori Katsuyama, Takayuki Kurokawa, and Yoshihito Osada. Double-network hydrogels with extremely high mechanical strength. *Advanced materials*, 15(14):1155–1158, 2003.

[14] Md Anamul Haque, Takayuki Kurokawa, and Jian Ping Gong. Super tough double network hydrogels and their application as biomaterials. *Polymer*, 53(9):1805–1822, 2012.

[15] Jeong-Yun Sun, Xuanhe Zhao, Widusha RK Illeperuma, Ovijit Chaudhuri, Kyu Hwan Oh, David J Mooney, Joost J Vlassak, and Zhigang Suo. Highly stretchable and tough hydrogels. *Nature*, 489(7414):133–136, 2012.

[16] Koichi Mayumi, Alba Marcellan, Guylaine Ducouret, Costantino Creton, and Tetsuharu Narita. Stress–strain relationship of highly stretchable dual cross-link gels: separability of strain and time effect. *ACS Macro Letters*, 2(12):1065–1068, 2013.

[17] Tao Lin Sun, Takayuki Kurokawa, Shinya Kuroda, Abu Bin Ihsan, Taigo Akasaki, Koshiro Sato, Md Anamul Haque, Tasuku Nakajima, and Jian Ping Gong. Physical hydrogels composed of polyampholytes demonstrate high toughness and viscoelasticity. *Nature materials*, 12(10):932–937, 2013.

[18] Qiang Chen, Hong Chen, Lin Zhu, and Jie Zheng. Fundamentals of double network hydrogels. *Journal of Materials Chemistry B*, 3(18):3654–3676, 2015.

[19] Tongqing Lu, Jikun Wang, Ruisen Yang, and TJ Wang. A constitutive model for soft materials incorporating viscoelasticity and mullins effect. *Journal of Applied Mechanics*, 84(2):021010, 2017.

[20] Jingyi Guo, Rong Long, Koichi Mayumi, and Chung-Yuen Hui. Mechanics of a dual cross-link gel with dynamic bonds: Steady state kinetics and large deformation effects. *Macromolecules*, 49(9):3497–3507, 2016.

[21] Sairam Pamulaparthi Venkata, Kunpeng Cui, Jingyi Guo, Alan T Zehnder, Jian Ping Gong, and Chung-Yuen Hui. Constitutive modeling of bond breaking and healing kinetics of physical polyampholyte (pa) gel. *Extreme Mechanics Letters*, 43:101184, 2021.

[22] Sairam Pamulaparthi Venkata, Kunpeng Cui, Jingyi Guo, Alan T Zehnder, Jian Ping Gong, and Chung-Yuen Hui. Constitutive modeling of strain-dependent bond breaking and healing kinetics of chemical polyampholyte (pa) gel. *Soft Matter*, 17(15):4161–4169, 2021.

[23] Jingyi Guo, Alan T Zehnder, Costantino Creton, and Chung-Yuen Hui. Time dependent fracture of soft materials: linear versus nonlinear viscoelasticity. *Soft Matter*, 16(26):6163–6179, 2020.

[24] Jikun Wang, Tianjiao Li, Fan Cui, Chung-Yuen Hui, Jingjie Yeo, and Alan T Zehnder. Metamodeling of constitutive model using gaussian process machine learning. *Journal of the Mechanics and Physics of Solids*, 154:104532, 2021.

[25] Jikun Wang, Kunpeng Cui, Bangguo Zhu, Jian Ping Gong, Chung-Yuen Hui, and Alan T Zehnder. Load transfer between permanent and dynamic networks due to stress gradients in nonlinear viscoelastic hydrogels. *Extreme Mechanics Letters*, 58:101928, 2023.

[26] Xiao Wang and Wei Hong. Delayed fracture in gels. *Soft Matter*, 8(31):8171–8178, 2012.

[27] Jingda Tang, Jianyu Li, Joost J Vlassak, and Zhigang Suo. Fatigue fracture of hydrogels. *Extreme Mechanics Letters*, 10:24–31, 2017.

[28] Hanne M van der Kooij, Simone Dussi, Gea T van de Kerkhof, Raoul AM Frijns, Jasper van der Gucht, and Joris Sprakel. Laser speckle strain imaging reveals the origin of delayed fracture in a soft solid. *Science advances*, 4(5):eaar1926, 2018.

[29] Bing Pan, Kemao Qian, Huimin Xie, and Anand Asundi. Two-dimensional digital image correlation for in-plane displacement and strain measurement: a review. *Measurement science and technology*, 20(6):062001, 2009.

[30] Kunpeng Cui, Ya Nan Ye, Tao Lin Sun, Chengtao Yu, Xueyu Li, Takayuki Kurokawa, and Jian Ping Gong. Phase separation behavior in tough and

self-healing polyampholyte hydrogels. *Macromolecules*, 53(13):5116–5126, 2020.

[31] Shawn A Chester. A constitutive model for coupled fluid permeation and large viscoelastic deformation in polymeric gels. *Soft Matter*, 8(31):8223–8233, 2012.

[32] Yiqi Mao, Fen Chen, Shujuan Hou, H Jerry Qi, and Kai Yu. A viscoelastic model for hydrothermally activated malleable covalent network polymer and its application in shape memory analysis. *Journal of the Mechanics and Physics of Solids*, 127:239–265, 2019.

[33] Yunwei Mao, Shaoting Lin, Xuanhe Zhao, and Lallit Anand. A large deformation viscoelastic model for double-network hydrogels. *Journal of the Mechanics and Physics of Solids*, 100:103–130, 2017.

[34] Shan Tang, M Steven Greene, and Wing Kam Liu. Two-scale mechanism-based theory of nonlinear viscoelasticity. *Journal of the Mechanics and Physics of Solids*, 60(2):199–226, 2012.

[35] Victor Crespo-Cuevas, Virginia L Ferguson, and Franck Vernerey. Poroviscoelasto-plasticity of agarose-based hydrogels. *Soft Matter*, 2023.

[36] Jan Niklas Fuhg, Christoph Böhm, Nikolaos Bouklas, Amelie Fau, Peter Wriggers, and Michele Marino. Model-data-driven constitutive responses: application to a multiscale computational framework. *International Journal of Engineering Science*, 167:103522, 2021.

[37] Sourav Saha, Zhengtao Gan, Lin Cheng, Jiaying Gao, Orion L Kafka, Xiaoyu Xie, Hengyang Li, Mahsa Tajdari, H Alicia Kim, and Wing Kam Liu. Hierarchical deep learning neural network (hidenn): An artificial intelligence (ai) framework for computational science and engineering. *Computer Methods in Applied Mechanics and Engineering*, 373:113452, 2021.

[38] Xing Liu, Christos E Athanasiou, Nitin P Padture, Brian W Sheldon, and Huajian Gao. A machine learning approach to fracture mechanics problems. *Acta Materialia*, 190:105–112, 2020.

[39] Jia-Ji Wang, Chen Wang, Jian-Sheng Fan, and YL Mo. A deep learning framework for constitutive modeling based on temporal convolutional network. *Journal of Computational Physics*, 449:110784, 2022.

[40] Kasma Diana Saharuddin, Mohd Hatta Mohammed Ariff, Irfan Bahiuddin, Saiful Amri Mazlan, Siti Aishah Abdul Aziz, Nurhazimah Nazmi, Abdul Yasser Abdul Fatah, and Khairunnisa Mohmad. Constitutive models for predicting field-dependent viscoelastic behavior of magnetorheological elastomer using machine learning. *Smart Materials and Structures*, 29(8):087001, 2020.

[41] Filippo Masi, Ioannis Stefanou, Paolo Vannucci, and Victor Maffi-Berthier. Thermodynamics-based artificial neural networks for constitutive modeling. *Journal of the Mechanics and Physics of Solids*, 147:104277, 2021.

[42] Minliang Liu, Liang Liang, and Wei Sun. Estimation of in vivo constitutive parameters of the aortic wall using a machine learning approach. *Computer methods in applied mechanics and engineering*, 347:201–217, 2019.

[43] Robin Schulte, Cavid Karca, Richard Ostwald, and Andreas Menzel. Machine learning-assisted parameter identification for constitutive models based on concatenated loading path sequences. *European Journal of Mechanics-A/Solids*, 98:104854, 2023.

[44] Shoujing Zheng and Zishun Liu. The machine learning embedded method of parameters determination in the constitutive models and potential applications for hydrogels. *International Journal of Applied Mechanics*, 13(01):2150001, 2021.

[45] Kenneth Levenberg. A method for the solution of certain non-linear problems in least squares. *Quarterly of applied mathematics*, 2(2):164–168, 1944.

[46] Donald W Marquardt. An algorithm for least-squares estimation of nonlinear parameters. *Journal of the society for Industrial and Applied Mathematics*, 11(2):431–441, 1963.

[47] Jorge J Moré. The levenberg-marquardt algorithm: implementation and theory. In *Numerical Analysis: Proceedings of the Biennial Conference Held at Dundee, June 28–July 1, 1977*, pages 105–116. Springer, 2006.

[48] ER Henry and J Hofrichter. [8] singular value decomposition: Application to analysis of experimental data. In *Methods in enzymology*, volume 210, pages 129–192. Elsevier, 1992.

[49] Eric R Henry. The use of matrix methods in the modeling of spectroscopic data sets. *Biophysical journal*, 72(2):652–673, 1997.

[50] Pemra Doruker, Ali Rana Atilgan, and Ivet Bahar. Dynamics of proteins predicted by molecular dynamics simulations and analytical approaches: Application to α-amylase inhibitor. *Proteins: Structure, Function, and Bioinformatics*, 40(3):512–524, 2000.

[51] Orly Alter, Patrick O Brown, and David Botstein. Singular value decomposition for genome-wide expression data processing and modeling. *Proceedings of the National Academy of Sciences*, 97(18):10101–10106, 2000.

[52] Marius Schmidt, Sudarshan Rajagopal, Zhong Ren, and Keith Moffat. Application of singular value decomposition to the analysis of time-resolved macromolecular x-ray data. *Biophysical journal*, 84(3):2112–2129, 2003.

[53] Charles Yang, Youngsoo Kim, Seunghwa Ryu, and Grace X Gu. Prediction of composite microstructure stress-strain curves using convolutional neural networks. *Materials & Design*, 189:108509, 2020.

[54] Oludare Isaac Abiodun, Aman Jantan, Abiodun Esther Omolara, Kemi Victoria Dada, Nachaat AbdElatif Mohamed, and Humaira Arshad. State-of-the-art in artificial neural network applications: A survey. *Heliyon*, 4(11):e00938, 2018.

[55] Rana Abou Khamis and Ashraf Matrawy. Evaluation of adversarial training on different types of neural networks in deep learning-based idss. In *2020 international symposium on networks, computers and communications (ISNCC)*, pages 1–6. IEEE, 2020.

[56] C Rasmussen and C Williams. Gaussian processes for machine learning.,(mit press: Cambridge, ma). 2006.

[57] Edoardo Menga, María J Sánchez, and Ignacio Romero. Anisotropic metamodels for computationally expensive simulations in nonlinear mechanics. *International Journal for Numerical Methods in Engineering*, 121(5):904–924, 2020.

[58] Juan Luis de Pablos, Edoardo Menga, and Ignacio Romero. A methodology for the statistical calibration of complex constitutive material models: Application to temperature-dependent elasto-visco-plastic materials. *Materials*, 13(19):4402, 2020.

[59] Jacob Gardner, Geoff Pleiss, Kilian Q Weinberger, David Bindel, and Andrew G Wilson. Gpytorch: Blackbox matrix-matrix gaussian process in-

ference with gpu acceleration. *Advances in neural information processing systems*, 31, 2018.

[60] Rudy J Wojtecki, Michael A Meador, and Stuart J Rowan. Using the dynamic bond to access macroscopically responsive structurally dynamic polymers. *Nature materials*, 10(1):14–27, 2011.

[61] Zhao Wei, Jian Hai Yang, Jinxiong Zhou, Feng Xu, Miklós Zrínyi, Patrick H Dussault, Yoshihito Osada, and Yong Mei Chen. Self-healing gels based on constitutional dynamic chemistry and their potential applications. *Chemical Society Reviews*, 43(23):8114–8131, 2014.

[62] Danielle Lynne Taylor and Marc in het Panhuis. Self-healing hydrogels. *Advanced Materials*, 28(41):9060–9093, 2016.

[63] Kunhao Yu, An Xin, and Qiming Wang. Mechanics of self-healing polymer networks crosslinked by dynamic bonds. *Journal of the Mechanics and Physics of Solids*, 121:409–431, 2018.

[64] Chao Wang, Nan Liu, Ranulfo Allen, Jeffrey B-H Tok, Yunpeng Wu, Fan Zhang, Yongsheng Chen, and Zhenan Bao. A rapid and efficient self-healing thermo-reversible elastomer crosslinked with graphene oxide. *Advanced materials*, 25(40):5785–5790, 2013.

[65] Koichi Mayumi, Jingyi Guo, Tetsuharu Narita, Chung Yuen Hui, and Costantino Creton. Fracture of dual crosslink gels with permanent and transient crosslinks. *Extreme Mechanics Letters*, 6:52–59, 2016.

[66] Chao Wang, Hui Wu, Zheng Chen, Matthew T McDowell, Yi Cui, and Zhenan Bao. Self-healing chemistry enables the stable operation of silicon microparticle anodes for high-energy lithium-ion batteries. *Nature chemistry*, 5(12):1042–1048, 2013.

[67] Ji Liu, Cindy Soo Yun Tan, Ziyi Yu, Yang Lan, Chris Abell, and Oren A Scherman. Biomimetic supramolecular polymer networks exhibiting both toughness and self-recovery. *Advanced Materials*, 29(10):1604951, 2017.

[68] Feng Luo, Tao Lin Sun, Tasuku Nakajima, Takayuki Kurokawa, Yu Zhao, Koshiro Sato, Abu Bin Ihsan, Xufeng Li, Honglei Guo, and Jian Ping Gong. Oppositely charged polyelectrolytes form tough, self-healing, and rebuildable hydrogels. *Advanced materials*, 27(17):2722–2727, 2015.

[69] Nabarun Roy, Bernd Bruchmann, and Jean-Marie Lehn. Dynamers: dynamic polymers as self-healing materials. *Chemical Society Reviews*, 44(11):3786–3807, 2015.

[70] Tingting Song, Bojun Jiang, Yida Li, Zhuohan Ji, Hongling Zhou, Dawei Jiang, Ilwoo Seok, Vignesh Murugadoss, Nan Wen, and Henry Colorado. Self-healing materials: a review of recent developments. *ES Materials & Manufacturing*, 14:1–19, 2021.

[71] Xueyu Li, Kunpeng Cui, Tao Lin Sun, Lingpu Meng, Chengtao Yu, Liangbin Li, Costantino Creton, Takayuki Kurokawa, and Jian Ping Gong. Mesoscale bicontinuous networks in self-healing hydrogels delay fatigue fracture. *Proceedings of the National Academy of Sciences*, 117(14):7606–7612, 2020.

[72] Jianyu Li, Zhigang Suo, and Joost J Vlassak. Stiff, strong, and tough hydrogels with good chemical stability. *Journal of Materials Chemistry B*, 2(39):6708–6713, 2014.

[73] Jianyu Li, Widusha RK Illeperuma, Zhigang Suo, and Joost J Vlassak. Hybrid hydrogels with extremely high stiffness and toughness. *ACS Macro Letters*, 3(6):520–523, 2014.

[74] Chung-Yuen Hui, Fan Cui, Alan Zehnder, and Franck J Vernerey. Physically motivated models of polymer networks with dynamic cross-links: comparative study and future outlook. *Proceedings of the Royal Society A*, 477(2255):20210608, 2021.

[75] George I Bell. Models for the specific adhesion of cells to cells: a theoretical framework for adhesion mediated by reversible bonds between cell surface molecules. *Science*, 200(4342):618–627, 1978.

[76] Konik Kothari, Yuhang Hu, Sahil Gupta, and Ahmed Elbanna. Mechanical response of two-dimensional polymer networks: role of topology, rate dependence, and damage accumulation. *Journal of Applied Mechanics*, 85(3), 2018.

[77] Samuel C Lamont, Jason Mulderrig, Nikolaos Bouklas, and Franck J Vernerey. Rate-dependent damage mechanics of polymer networks with reversible bonds. *Macromolecules*, 54(23):10801–10813, 2021.

[78] Ahmed Ghareeb and Ahmed Elbanna. Modeling fracture in rate-

dependent polymer networks: A quasicontinuum approach. *Journal of Applied Mechanics*, 88(11), 2021.

[79] Franck J Vernerey. Mechanics of transient semi-flexible networks: Soft-elasticity, stress relaxation and remodeling. *Journal of the Mechanics and Physics of Solids*, 160:104776, 2022.

[80] M Liu, J Guo, C-Y Hui, and AT Zehnder. Application of digital image correlation (dic) to the measurement of strain concentration of a pva dual-crosslink hydrogel under large deformation. *Experimental Mechanics*, 59:1021–1032, 2019.

[81] Zhijie Zhang, Quan Chen, and Ralph H Colby. Dynamics of associative polymers. *Soft Matter*, 14(16):2961–2977, 2018.

[82] Kevin J Henderson, Tian C Zhou, Kathryn J Otim, and Kenneth R Shull. Ionically cross-linked triblock copolymer hydrogels with high strength. *Macromolecules*, 43(14):6193–6201, 2010.

[83] Tetsuharu Narita, Koichi Mayumi, Guylaine Ducouret, and Pascal Hebraud. Viscoelastic properties of poly (vinyl alcohol) hydrogels having permanent and transient cross-links studied by microrheology, classical rheometry, and dynamic light scattering. *Macromolecules*, 46(10):4174–4183, 2013.

[84] Chao Chen, Zhengjin Wang, and Zhigang Suo. Flaw sensitivity of highly stretchable materials. *Extreme Mechanics Letters*, 10:50–57, 2017.

[85] Sammy Hassan, Junsoo Kim, et al. Polyacrylamide hydrogels. iv. near-perfect elasticity and rate-dependent toughness. *Journal of the Mechanics and Physics of Solids*, 158:104675, 2022.

[86] Yoshimi Tanaka, Rikimaru Kuwabara, Yang-Ho Na, Takayuki Kurokawa, Jian Ping Gong, and Yoshihito Osada. Determination of fracture energy of high strength double network hydrogels. *The Journal of Physical Chemistry B*, 109(23):11559–11562, 2005.

[87] Samy Mzabi, Daniel Berghezan, Stéphane Roux, Francois Hild, and Costantino Creton. A critical local energy release rate criterion for fatigue fracture of elastomers. *Journal of Polymer Science Part B: Polymer Physics*, 49(21):1518–1524, 2011.

[88] Ruobing Bai, Jiawei Yang, and Zhigang Suo. Fatigue of hydrogels. *European Journal of Mechanics-A/Solids*, 74:337–370, 2019.

[89] Jianzhu Ju, Gabriel E. Sanoja, Med Yassine Nagazi, Luca Cipelletti, Zezhou Liu, Chung-Yuen Hui, Matteo Ciccotti, Tetsuharu Narita, and Costantino Creton. Fast detection of early-stage damage in soft elastomers. *In sumbission*, 2023.

[90] Yalin Yu, Nikolaos Bouklas, Chad M Landis, and Rui Huang. Poroelastic effects on the time-and rate-dependent fracture of polymer gels. *Journal of Applied Mechanics*, 87(3), 2020.

[91] S Pearson. Delayed fracture of sintered alumina. *Proceedings of the Physical Society. Section B*, 69(12):1293, 1956.

[92] NJ Petch and P Stables. Delayed fracture of metals under static load. *Nature*, 169:842–843, 1952.

[93] Olivier Lengliné, Renaud Toussaint, Jean Schmittbuhl, Jean E Elkhoury, JP Ampuero, Ken Tore Tallakstad, Stéphane Santucci, and Knut Jørgen Mløy. Average crack-front velocity during subcritical fracture propagation in a heterogeneous medium. *Physical Review E*, 84(3):036104, 2011.

[94] Daniel Bonn, Hamid Kellay, Michael Prochnow, Karim Ben-Djemiaa, and Jacques Meunier. Delayed fracture of an inhomogeneous soft solid. *Science*, 280(5361):265–267, 1998.

[95] Paulina J Skrzeszewska, Joris Sprakel, Frits A de Wolf, Remco Fokkink, Martien A Cohen Stuart, and Jasper van der Gucht. Fracture and self-healing in a well-defined self-assembled polymer network. *Macromolecules*, 43(7):3542–3548, 2010.

[96] Sadia Nazneen Karobi, Tao Lin Sun, Takayuki Kurokawa, Feng Luo, Tasuku Nakajima, Takayuki Nonoyama, and Jian Ping Gong. Creep behavior and delayed fracture of tough polyampholyte hydrogels by tensile test. *Macromolecules*, 49(15):5630–5636, 2016.

[97] Yan Yang, Haoyu Guo, Zhenjiang Du, Wei Hong, Tongqing Lu, and Tiejun Wang. Rate-dependent fracture of hydrogels due to water migration. *Journal of the Mechanics and Physics of Solids*, 167:105007, 2022.

[98] Kunpeng Cui, Ya Nan Ye, Chengtao Yu, Xueyu Li, Takayuki Kurokawa,

and Jian Ping Gong. Stress relaxation and underlying structure evolution in tough and self-healing hydrogels. *ACS Macro Letters*, 9(11):1582–1589, 2020.

[99] Yunwei Mao and Lallit Anand. A theory for fracture of polymeric gels. *Journal of the Mechanics and Physics of Solids*, 115:30–53, 2018.

[100] AA Kaminsky. Mechanics of the delayed fracture of viscoelastic bodies with cracks: Theory and experiment. *International Applied Mechanics*, 50:485–548, 2014.

[101] Manoj K Chaudhury. Rate-dependent fracture at adhesive interface. *The Journal of Physical Chemistry B*, 103(31):6562–6566, 1999.

[102] Vincent Placet and Patrick Delobelle. Mechanical properties of bulk polydimethylsiloxane for microfluidics over a large range of frequencies and aging times. *Journal of Micromechanics and Microengineering*, 25(3):035009, 2015.

[103] Rong Long, Venkat R Krishnan, and Chung-Yuen Hui. Finite strain analysis of crack tip fields in incompressible hyperelastic solids loaded in plane stress. *Journal of the Mechanics and Physics of Solids*, 59(3):672–695, 2011.

[104] James R Rice. A path independent integral and the approximate analysis of strain concentration by notches and cracks. 1968.

[105] RS Rivlin and A Gr Thomas. Rupture of rubber. i. characteristic energy for tearing. *Journal of polymer science*, 10(3):291–318, 1953.

[106] Arthur Tobolsky and Henry Eyring. Mechanical properties of polymeric materials. *The Journal of chemical physics*, 11(3):125–134, 1943.

[107] Shawn R Lavoie, Rong Long, and Tian Tang. A rate-dependent damage model for elastomers at large strain. *Extreme Mechanics Letters*, 8:114–124, 2016.

[108] A Cohen. A padé approximant to the inverse langevin function. *Rheologica acta*, 30:270–273, 1991.

[109] Manoj K Chaudhury and George M Whitesides. Direct measurement of interfacial interactions between semispherical lenses and flat sheets

of poly (dimethylsiloxane) and their chemical derivatives. *Langmuir*, 7(5):1013–1025, 1991.

[110] GJ Lake and AG Thomas. The strength of highly elastic materials. *Proceedings of the Royal Society of London. Series A. Mathematical and Physical Sciences*, 300(1460):108–119, 1967.

[111] Mary C Boyce and Ellen M Arruda. Constitutive models of rubber elasticity: a review. *Rubber chemistry and technology*, 73(3):504–523, 2000.

[112] Canhui Yang, Tenghao Yin, and Zhigang Suo. Polyacrylamide hydrogels. i. network imperfection. *Journal of the Mechanics and Physics of Solids*, 131:43–55, 2019.

[113] C-Y Hui, SJ Bennison, and JD Londono. Crack blunting and the strength of soft elastic solids. *Proceedings of the Royal Society of London. Series A: Mathematical, Physical and Engineering Sciences*, 459(2034):1489–1516, 2003.